GEORGIA INSTITUTE OF TECHNOLOGY
OFFICE OF RESEARCH AOMINISTRATION

RESEARCH PROJECT INITIATION

Date: September 25, 1973

Project Title: "Study of Effects of Injector Geometry on Fuel-Air Mixing and Combustion"

Project No: E-16-640

Green Cd
Misc

Principal Investigator Dr. Louis Baugert

Sponsor: National Aeronautics and Space Administration

Agreement Period: From 9/1/73 Until 8/31/74

Type Agreement: Grant No. NGR 11-002-177

Amount:

$18,932	NASA
1,209	GIT
$20,141	

Reports Required: Semi-Annual Report
Final Report

Sponsor Contact Person (s):

Administrator

Mr. Donald H. Carson
NASA
Langley Research Center
Hampton, Virginia
(703) 827-3214

Technical

Mr. William B. Boatright
Advanced Facilities Research Section
NASA
Langley Research Center
Hampton, Virginia
(703) 827-3772

Assigned to: ~~Aerospace Engineering~~

COPIES TO:

Principal Investigator	Library
School Director	Rich Electronic Computer Center
Dean of the College	Photographic Laboratory
Director, Research Administration	Project File
Director, Financial Affairs (2)	
Security-Reports-Property Office ✓	
Patent Coordinator	Other

RA-3 (6-71)

GEORGIA INSTITUTE OF TECHNOLOGY
OFFICE OF CONTRACT ADMINISTRATION

SPONSORED PROJECT TERMINATION

Date: September 6, 1977

Project Title: Study of Effects of Injector Geometry on Fuel-Air Mixing and Combustion.

Project No: E-16-640

Project Director: Dr. L. H. Bangert

Sponsor: NASA - Langley Research Center, Hampton, VA

Effective Termination Date: 1/31/77

Clearance of Accounting Charges: 2/28/77

Grant/Contract Closeout Actions Remaining:

- x Final Invoice and Closing Documents
- x Final Fiscal Report
- x Final Report of Inventions
- x Govt. Property Inventory & Related Certificate
- _ Classified Material Certificate
- _ Other _____

Assigned to: Aerospace Engineering (School/Laboratory)

COPIES TO:

Project Director	Library, Technical Reports Section ✓
Division Chief (EES)	Office of Computing Services
School/Laboratory Director	Director, Physical Plant
Dean/Director–EES	EES Information Office
Accounting Office	Project File (OCA)
Procurement Office	Project Code (GTRI)
Security Coordinator (OCA)	Other _____
Reports Coordinator (OCA)	

CA–4 (3/76)

E-16-640

GEORGIA INSTITUTE OF TECHNOLOGY
ATLANTA, GEORGIA 30332

OFFICE OF
THE DIRECTOR OF
FINANCIAL AFFAIRS

October 12, 1977

Mr. F. S. Kawalkiewicz
Grants Officer
NASA
Langley Research Center
Hampton, Va. 23665

Dear Mr. Kawalkiewicz:

Enclosed are the Final Cumulative Cost Expenditure Report and the final Form 1031 for Grant Number NGR 11-002-177 covering the period September 1, 1973 through January 31, 1977.

If you have questions or desire additional information, please let us know.

Sincerely yours,

Evan Crosby
Associate Director of
Financial Affairs

EC/bs
Enclosures as stated
cc: Dr. A. L. Ducoffe
Dr. L. H. Bangert
Mr. E. E. Renfro
Mr. A. H. Becker
File E-16-640

GRANTS

Final- Cumulative Cost Expenditure Report

1.	Cumulative Award.....	$ 48,898.00
2.	Cumulative Costs.....	$ 48,816.38
	(a) Balance.....	$ 81.62
3.	Cost Sharing.....	$ 2,987.03

Certification: To the best of our knowledge all costs due from the U. S. Government in the performance of NASA Grant Number NGR 11-002-177, are included in this cumulative cost statement. No additional costs will be billed for the services provided thereunder.

Georgia Institute of Technology
Institution Name

Evan Crosby
Authorized Approving Official
Associate Director of Financial Affairs

5 Oct 77
Date

Dr. L. H. Bangert
Principal Investigator

Enclosure

GRANTEE QUARTERLY [illegible] 1731777

National Aeronautics & Space Admin.
Langley Research Ctr., Hampton, Va. 23665

FROM: Georgia Institute of Technology
Atlanta, Georgia 30332

GRANT NO. (1)	AMOUNT OF AWARD (2)	EXPENDED THIS QUARTER (3)	EXPENDED TO DATE (4)	ANTICIPATED EXPENDITURES NEXT QUARTER (5)	CASH RECEIVED TO DATE (6)	CASH REQUIRED NEXT QUARTER (7)	REMARKS (8)
-11-002-177	$48,898.00	-0-	$48,816.38	-0-	$48,816.38	-0-	I certify that all payments are for appropriate purposes and in accordance with the agreements set forth in the application and award documents.

LAST PAYMENT VOUCHER DRAWN		10. CASH REQUIRED NEXT QUARTER – COL. (7) (Enter breakdown for each month in quarter)			11. EST. CASH REQUIRED FOR FIRST MONTH OF NEXT SUCCEEDING QUARTER
	DATED	1ST MO. IN QTR. (Amt.)	2D MO. IN QTR. (Amt.)	3D MO. IN QTR. (Amt.)	

I CERTIFY THAT NO INTEREST WAS EARNED ON RETAINED FEDERAL FUNDS.

TITLE: Associate Director of Financial Affairs

SIGNATURE: Evan Crosby

DATE: 10/12/77

RCS 10PUBL00415

PART 1

ORM 1031 DEC 75 PREVIOUS EDITION MAY BE USED.

C-16-640

NASA Grant No. NGR-11-002-177

Semi-Annual Progress Report

February 1974

STUDY OF EFFECTS OF INJECTOR GEOMETRY ON FUEL-AIR MIXING AND COMBUSTION

by

Louis H. Bangert

Georgia Institute of Technology

Atlanta, Georgia 30332

Prepared for

NATIONAL AERONAUTICS AND SPACE ADMINISTRATION

Langley Research Center

Hampton, Virginia 23665

Mr. William B. Boatright, Technical Officer

ABSTRACT

This research involves a series of experiments, and supporting analysis, to relate characteristics of fuel injector geometry to the turbulence produced and to the resultant hydrogen-air mixing and combustion. The accomplishments of the research program for the period September 1973 through February 1974 are described. In summary, these are: (1) The injector models are designed and fabricated; (2) The finite difference computer program for the flow field has been checked out; (3) Calculations for effects of turbulence initial conditions and of turbulence on reaction rate have been started.

1.0 INTRODUCTION

1.1 Background

The problem of obtaining rapid fuel-air mixing and combustion in a supersonic air stream is part of the larger problem of development of a supersonic combustion ramjet (scramjet) for hypersonic flight. There is a need to know the relationship between heat-release distribution and fuel injector design, to allow optimum combustor design. There is also great uncertainty in predicting fuel-air mixing to molecular scales, coupled with the desire to achieve this as close to the fuel injector as possible. More background details, plus a literature review of recent experimental studies of scramjet injectors and related configurations, are given in Reference 1.

As described in (1), recent studies of base flow with mass addition lead to the conclusions that:

(1) The effect of base and injection orifice geometry on base pressure is only partially known, and their effects on turbulence properties in the near field are unknown.

(2) The base drag for single-orifice injection is strongly influenced by d_J/d_B, so that there is also a strong effect on turbulence kinetic energy, k, and turbulence length scale, $k^{1.5}/\epsilon$, in the near field.

The above conclusions were later supported by the work of Matsumoto, et al[2], in low-speed (incompressible) air flow. They found that injector wall thickness has a strong influence on near field flow behavior, especially as U_J and U_∞ become more nearly equal. They also found that mixing length is not constant in the near field. This is expected, because there is more than

one length scale in the near field, and so a simple mixing length model is not adequate.

1.2 Objectives

The overall objective is to relate characteristics of fuel injector geometry to the turbulence produced and to the resultant hydrogen-air mixing and combustion. The particular objective of this study is to determine the effect of d_J/d_B, the ratio of fuel jet diameter to injector base diameter, on hydrogen-air mixing and combustion.

2.0 DESCRIPTION OF ACCOMPLISHMENTS

2.1 Experiments

The experimental task, as described in (1), is to perform mixing and combustion experiments with three single-orifice, axisymmetric injectors, for which d_J/d_B is varied. The external geometry of the injectors is the same otherwise. The test gases are hydrogen-air and hydrogen-nitrogen.

These first experiments are restricted to subsonic and sonic hydrogen injection. $\dot{m}_J/\rho_\infty U_\infty d_B^2$ will be varied for each d_J/d_B. The principal measurements will be pitot pressure profiles and mean concentration profiles, as well as test flow conditions. The experiments will be performed in the Langley Ceramic-Heated Tunnel.

The details of the injector design are reported in (3). This includes a description of calculations of required hydrogen mass flow rates, heat transfer to the injector, and test points.

The start of the experiments has been delayed several times because of unavailability of certain materials for repairs to the Ceramic-Heated Tunnel, and because of damage to the Mach 2 nozzle for the tunnel. Present estimates are for the experiments to begin in May 1974.

2.2 Analysis

The analytical tasks, as described in (1) are:

(i) Evaluate effects of d_J/d_B on k and ϵ in the near field, particularly with regard to initial conditions needed for the flow field prediction methods.

(ii) Evaluate proposed models of the effect of turbulence on reaction rate.

These tasks are to be accomplished by comparing finite-difference computer

calculations with the experimental data from this program.

A simple mixing-length model is not adequate to calculate turbulent transport in the near field of the injector. Convection and diffusion of turbulence are important here, so the turbulent length scale, $k^{1.5}/\epsilon$, is not simply related to mean flow properties. It is necessary to use at least a two-equation model for k and ϵ (i.e., two partial differential equations with k and ϵ as dependent variables).

The major effort for the period September 1973 to February 1974 was setting up and checking out a finite difference computer program that solves a set of parabolic partial differential equations. The program is a modification of that described in (4). Equations of continuity, species continuity, momentum, and stagnation enthalpy are solved, in addition to two equations for k and ϵ describing the turbulence dynamics. These last two equations are:

$$\rho U \frac{\partial k}{\partial x} + \rho V \frac{\partial k}{\partial y} = \frac{1}{r} \frac{\partial}{\partial y} \left(\frac{r \mu_t}{\sigma_k} \frac{\partial k}{\partial y} \right) + \mu_t \left(\frac{\partial U}{\partial y} \right)^2 - \rho \epsilon \qquad (1)$$

and

$$\rho U \frac{\partial \epsilon}{\partial x} + \rho V \frac{\partial \epsilon}{\partial y} = \frac{1}{r} \frac{\partial}{\partial y} \left(\frac{r \mu_t}{\sigma_\epsilon} \frac{\partial \epsilon}{\partial y} \right) + C_{\epsilon 1} \frac{\epsilon}{k} \mu_t \left(\frac{\partial U}{\partial y} \right)^2 - C_{\epsilon 2} \frac{\rho \epsilon^2}{k} \qquad (2)$$

where

$$\mu_t = C_\mu \frac{\rho k^2}{\epsilon} \qquad (3)$$

In the calculations described below, $C_\mu = 0.09$, $C_{\epsilon 1} = 1.43$, $C_{\epsilon 2} = 1.92$, $\sigma_k = 1.0$, $\sigma_\epsilon = 1.3$. References 5-7 contain detailed descriptions of the considerations leading to these choices.

Recent modeling of the effect of turbulent mixing on time-average reaction rate has recognized the importance of concentration fluctuations in determining reaction rate. Thus, to make calculations of this kind, an equation for mean square fuel concentration fluctuations, g_{fu}, has been included in the computer program. This equation is (6,7):

$$\rho U \frac{\partial g}{\partial x} + \rho V \frac{\partial g}{\partial y} = \frac{1}{r} \frac{\partial}{\partial y}\left(\frac{r\mu_t}{\sigma_g} \frac{\partial g}{\partial y}\right) + C_{g1}\, \mu_t \left(\frac{\partial G}{\partial y}\right)^2 - C_{g2}\, \rho^2\, g\, k/\mu_t \qquad (4)$$

In equation (4), g is g_{fu} and G is $\bar{m}_{fu}$. For the calculations shown in Figure 3, $\sigma_g = 0.7$, $C_{g1} = 3.0$, and $C_{g2} = 0.20$.

Equation (4) can be used to compute the mean square fluctuation of other scalar quantities, such as oxygen concentration and temperature, by making appropriate identification of g and G. For example, it may be desirable later to add an equation like (4) for mean square oxygen concentration fluctuations.

The computer program has now been checked out. This is illustrated in Figures 1 - 6, which show comparisons of calculations with experimental data for free jets and for wall boundary layers.

Figure 1 showns U/U_{AXIS} versus $r/r_{0.5}$ for an air jet issuing into quiescent air. Figure 2 shows $\bar{m}_{fu}/\bar{m}_{fu,AXIS}$ versus $r/r_{0.5}$ for a case where the "fuel" is an inert injectant with the same properties as air. In both Figures 1 and 2, the mean flow has reached self-similarity. Figure 3

shows $(g_{fu}/g_{fu,AXIS})^{0.5}$ versus $r/r_{0.5,fu}$ for the same flow as in Figures 1 and 2. These seem to be the only experimental data showing a profile of concentration fluctuations across the jet. It is significant that approximately 40 jet diameters are required for the calculation to reach the self-similar profile shown in Figure 3, while the calculated mean flow quantities reach self-similarity in about 10 jet diameters. This behavior is also consistent with experimental results (8,9).

Figures 4-6 show some calculations for wall boundary layers. Although these are not of direct application to the present study, they were included in the program checkout. This is because it is important to check that the computer program can handle wall flows, as well as free shear flows. Figure 4 shows the mean velocity profile near a smooth wall for a constant-pressure turbulent boundary layer on a smooth wall. The calculations were started with a power-law mean velocity profile. Initial values of k and ϵ were obtained by assuming $\mu_t = 1000\ \mu_{AIR}$. Then, an initial shear stress profile is obtained from $\tau = \mu_t\ \partial U/\partial y$. Finally, $k = \tau/\rho\ C_\mu^{0.5}$ and $\epsilon = C_\mu\ \rho\ k^2/\mu_t$. Figure 4 shows conditions about 30 boundary-layer thicknesses from the start, so the results are essentially independent of the assumed initial conditions. This general procedure is suitable, however, for cases when only the initial mean velocity profile is known. For such cases, the assumed initial μ_t must be varied until there is agreement with data near the start of the flow (5). If $\partial U/\partial y \cong 0$, $k = \text{const} \times U^2$ provides a suitable starting value. For the calculations shown in Figures 1-3, this constant was chosen to be 10^{-4}.

Figure 5 shows the variation of wall shear stress downstream of an abrupt change in surface roughness (smooth to rough). Figure 6 shows the mean velocity profiles at several locations for the same flow. This

case is of interest because a simple mixing-length model cannot handle it. The turbulence structure is strongly influenced by flow history, and not by local conditions alone.

The next steps in the analytical part of the program are:

(i) Examine the effect of changes in initial conditions for turbulence energy, k, and length scale, $k^{1.5}/\varepsilon$.

(ii) Examine the behavior of proposed models for the effect of turbulence on reaction rate.

It is planned to perform (i) and (ii) first for the experimental conditions of (12), as both pitot pressure and mean concentration profiles are available for this case.

When the chemical reaction rate is controlled by turbulent mixing, the chemical kinetic reaction time is much shorter than the time for large eddies of fuel and air to mix down to molecular scales. The latter time is expected to be of the same order as the characteristic time of the large eddies, k/ε. This is by analogy with the transfer of energy from the large eddies to the microscales, when, at large Reynolds numbers, they are statistically separated, and the rate of dissipation is controlled by the rate of transfer. If this hypothesis is correct:

$$\text{time-average reaction rate} = R_{fu} \quad \alpha - \rho\varepsilon/k \tag{5}$$

Here, R_{fu} is the source term in the time-average species continuity equation for the fuel. The Spalding (10) and Spalding-Lilley (11) eddy break-up models are special cases of equation (5). Both were developed for premixed fuel-air mixtures.

The Spalding-Lilley model (11) is:

$$R_{fu} = -\left(C_{EBU} / C_{\mu} \right) \quad g_{fu}^{0.5} \quad \rho\varepsilon/k \tag{6}$$

and so makes reaction rate proportional to the rms value of fuel concentration fluctuations. The accuracy of equation (6) for initially unmixed flows has not yet been determined. $C_{EBU} = 0.53$ is recommended in (11).

A possibly useful approach for initially unmixed fuel and air streams is to write:

$$R_{fu} = - C \ \overline{m_{fu} \, m_{ox}} \ \rho\varepsilon/k$$

$$= - C \ (\bar{m}_{fu} \cdot \bar{m}_{ox} + \overline{m_{fu}' \ m_{ox}'}) \ \rho\varepsilon/k$$

$$= - C \ (\bar{m}_{fu} \cdot \bar{m}_{ox} + C_{fo} \ g_{fu}^{0.5} \ g_{ox}^{0.5}) \ \rho\varepsilon/k \quad (7)$$

where C_{fo} is a correlation coefficient between fuel and oxygen fluctuations, and $0 \leq C_{fo} \leq 1$. C is a positive constant, to be determined by experiment. Both equation (6) and the model of (10) are special cases of equation (7). Some of the possibilities of equation (7), and simplifications of it, will be explored.

3.0 SUMMARY

The accomplishments of this research program through February 1974 are:

(1) The injector models are designed and fabricated, and the experimental part of the program is ready to begin.

(2) The finite difference computer program for analysis of the flow field and comparison with data has been successfully checked out. This program uses a two-equation model for turbulence dynamics and an equation for concentration fluctuations.

(3) Calculations are now being performed for the effects of variation of initial conditions for k and ϵ, and for cases where the effect of turbulence on reaction rate is included.

REFERENCES

1. Bangert, L. H., "Study of Effects of Injector Geometry on Fuel-Air Mixing and Combustion", a Research Proposal submitted to NASA Langley Research Center, April 1973.

2. Matsumoto, I. R., Kimoto, K. and Tsuchimoto, N., "A Study on Double Concentric Jets", JSME Bulletin, V. 16, March 1973, pp. 529-540.

3. Bangert, L. H., "Study of Effects of Injector Geometry on Fuel-Air Mixing and Combustion", Progress Report 1, to NASA Langley Research Center, August 1973.

4. Patankar, S. V. and Spalding, D. B., Heat and Mass Transfer in Boundary Layers, 2nd ed., Intertext Books, London, 1970.

5. Launder, B. E., Morse, A., Rodi, W. and Spalding, D. B., "The Prediction of Free Shear Flows - A Comparison of the Performance of Six Turbulence Models," NASA Conference on Free Shear Flows, V. 1, July 1972.

6. Launder, B. E., and Spalding, D. B., "Turbulence Models and Their Application to the Prediction of Internal Flow", Heat and Fluid Flow, V. 2, January 1972, pp. 43-54.

7. Spalding, D. B., "Concentration Fluctuations in a Round Turbulent Free Jet", Chem. Eng. Sci., V. 26, 1971, pp. 95-107.

REFERENCES (continued)

8. Tennekes, H. and Lumley, J. L., A First Course in Turbulence, MIT Press, 1972.

9. Hinze, J. O., Turbulence, McGraw-Hill, 1959.

10. Spalding, D. B., "Mixing and Chemical Reaction in Steady Confined Turbulent Flames", 13th Symposium (Int.) on Combustion, 1970, pp. 649-657.

11. Lilley, D. G., "Turbulent Swirling Flame Prediction", AIAA Paper 73-651, July 1973.

12. Anderson, G. Y., Agnone, A.M. and Russin, W. R., "Composition Distribution and Equivalent Body Shape for a Reacting, Coaxial, Supersonic Hydrogen-Air Flow", NASA TN D-6123, January 1971.

SYMBOLS

d_B	base diameter of injector
d_J	fuel jet diameter
g_{fu}, g_{ox}	mean square fluctuation of fuel mass fraction and oxygen mass fraction, respectively
k	turbulent kinetic energy per unit mass
m_{fu}, m_{ox}	mass fraction of fuel and oxygen, respectively
$\dot{m}_J$	fuel mass flow rate from injector
r	distance from axis of symmetry
R_{fu}	rate of generation of fuel (mass/volume/time)
U	mean velocity in x - direction
U_J	mean velocity of fuel at injection point
U_∞	mean velocity of undisturbed air at injection station
V	mean velocity in y - direction
x	distance in mainstream direction
y	distance in cross-stream direction
ϵ	dissipation rate of turbulent kinetic energy (energy/mass/time)
μ_t	effective viscosity for turbulent transport
ρ	density
ρ_∞	density of undisturbed air at injection station
σ_k, σ_ϵ, σ_g	effective Prandtl-Schmidt numbers for turbulent transport of k, ϵ and g, respectively
τ	shear stress
$\overline{(\ )}$	mean or time-average value
$(\ )'$	fluctuating value; i.e., difference between instantaneous and mean values

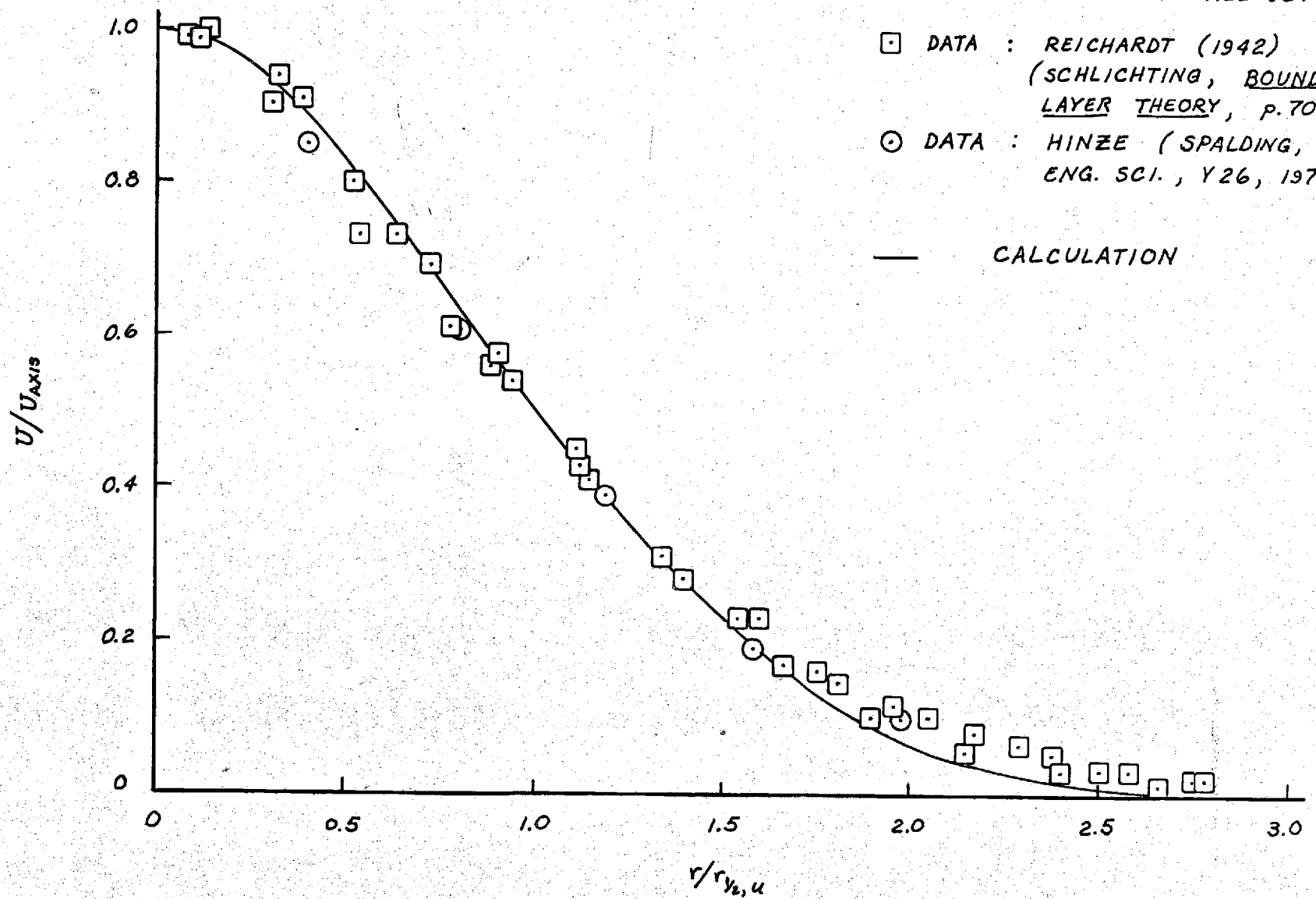
CIRCULAR TURBULENT FREE JET
DATA : REICHARDT (1942) (SCHLICHTING, BOUNDARY LAYER THEORY, p. 700)
DATA : HINZE (SPALDING, CHEM. ENG. SCI., Y26, 1971)
CALCULATION
1.0
0.8
0.6
0.4
0.2
0
U/U_{AXIS}
0
0.5
1.0
1.5
2.0
2.5
3.0
$r/r_{1/2,u}$

FIGURE 1

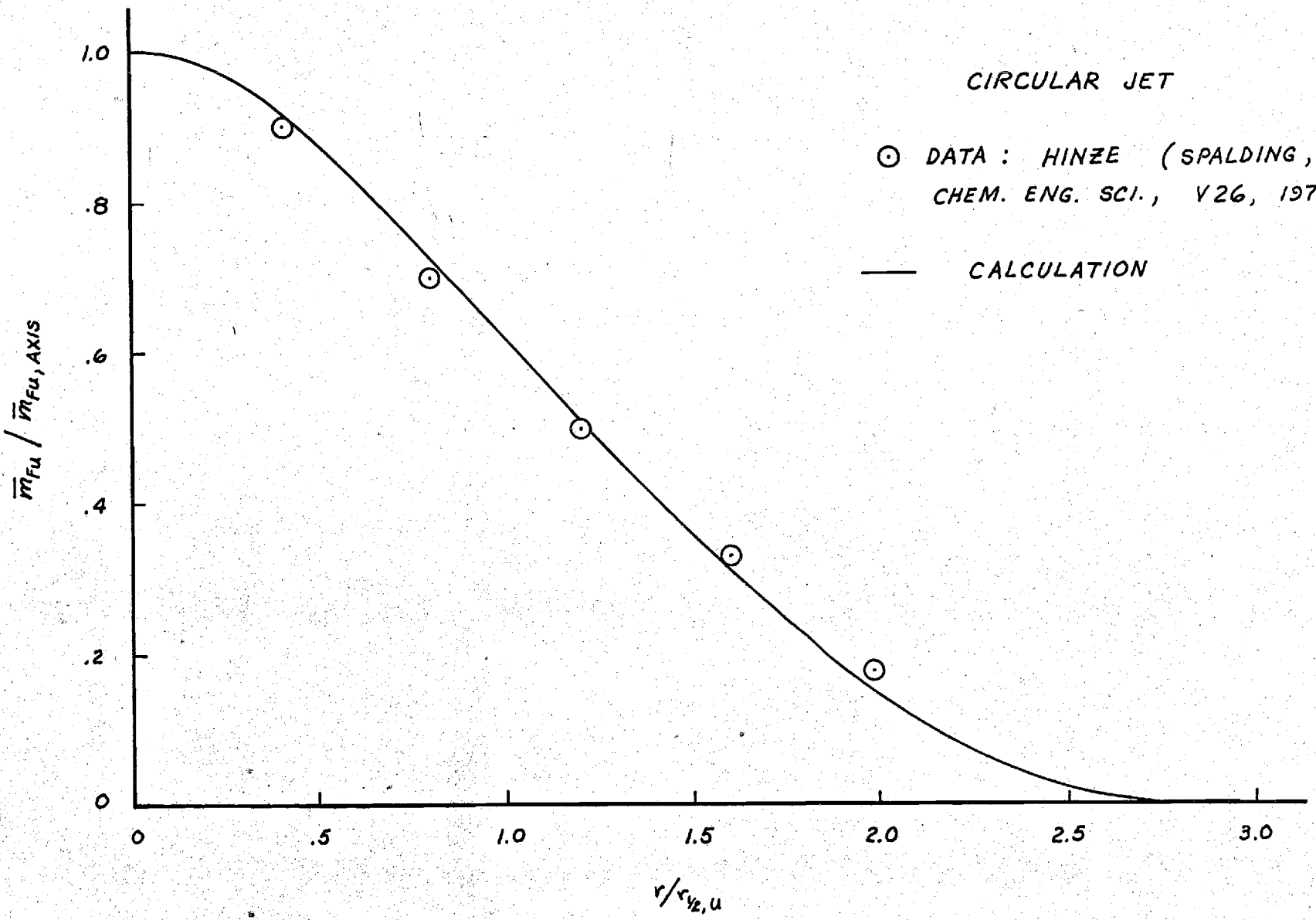
CIRCULAR JET
⊙ DATA : HINZE (SPALDING, CHEM. ENG. SCI., V26, 1971)
—— CALCULATION
$\bar{m}_{Fu} / \bar{m}_{Fu,AXIS}$
1.0
.8
.6
.4
.2
0
0
.5
1.0
1.5
2.0
2.5
3.0
$r/r_{1/2,u}$

FIGURE 2

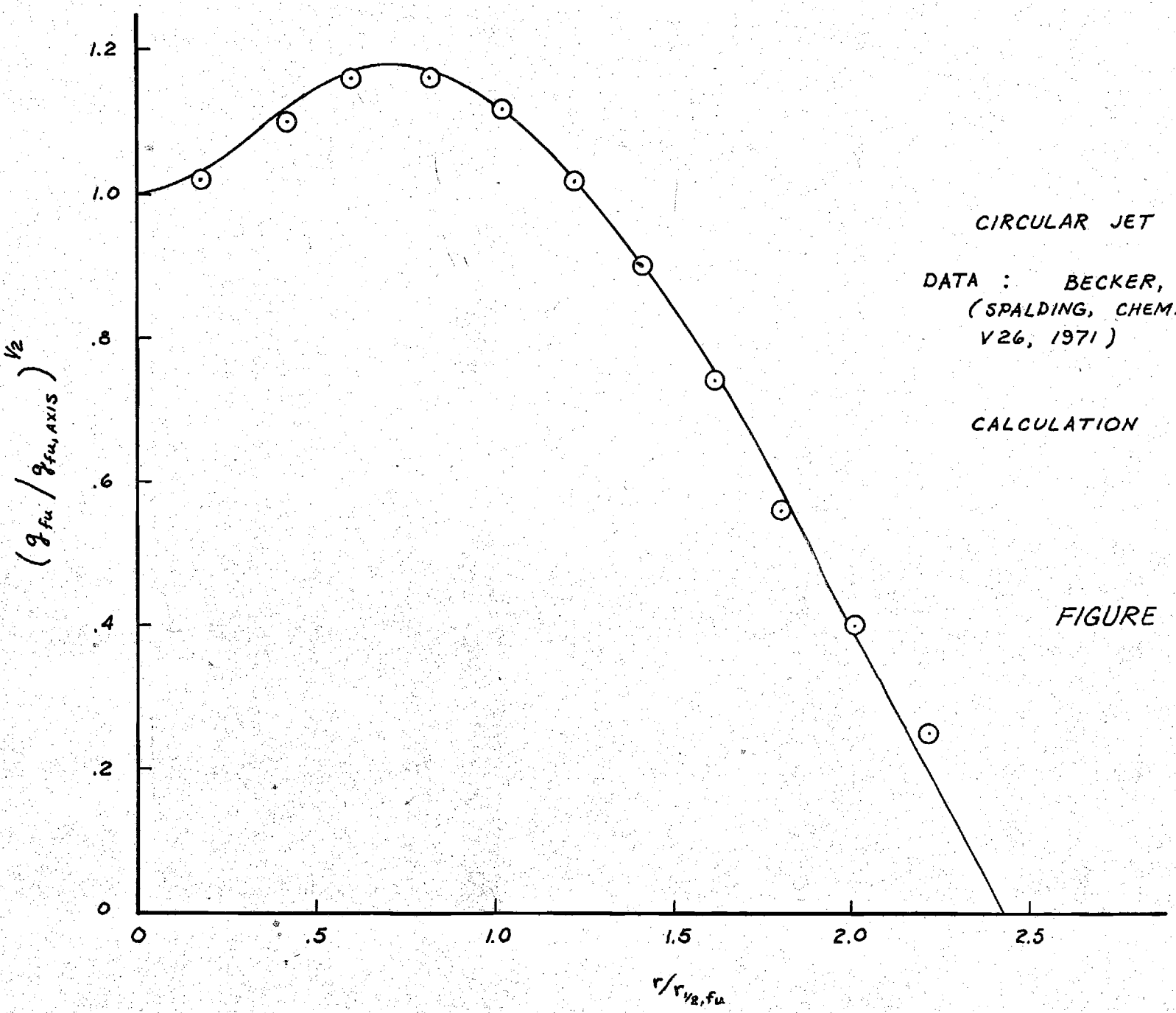

CIRCULAR JET

DATA : BECKER, ET AL
(SPALDING, CHEM. ENG. SCI., V26, 1971)

CALCULATION

FIGURE 3

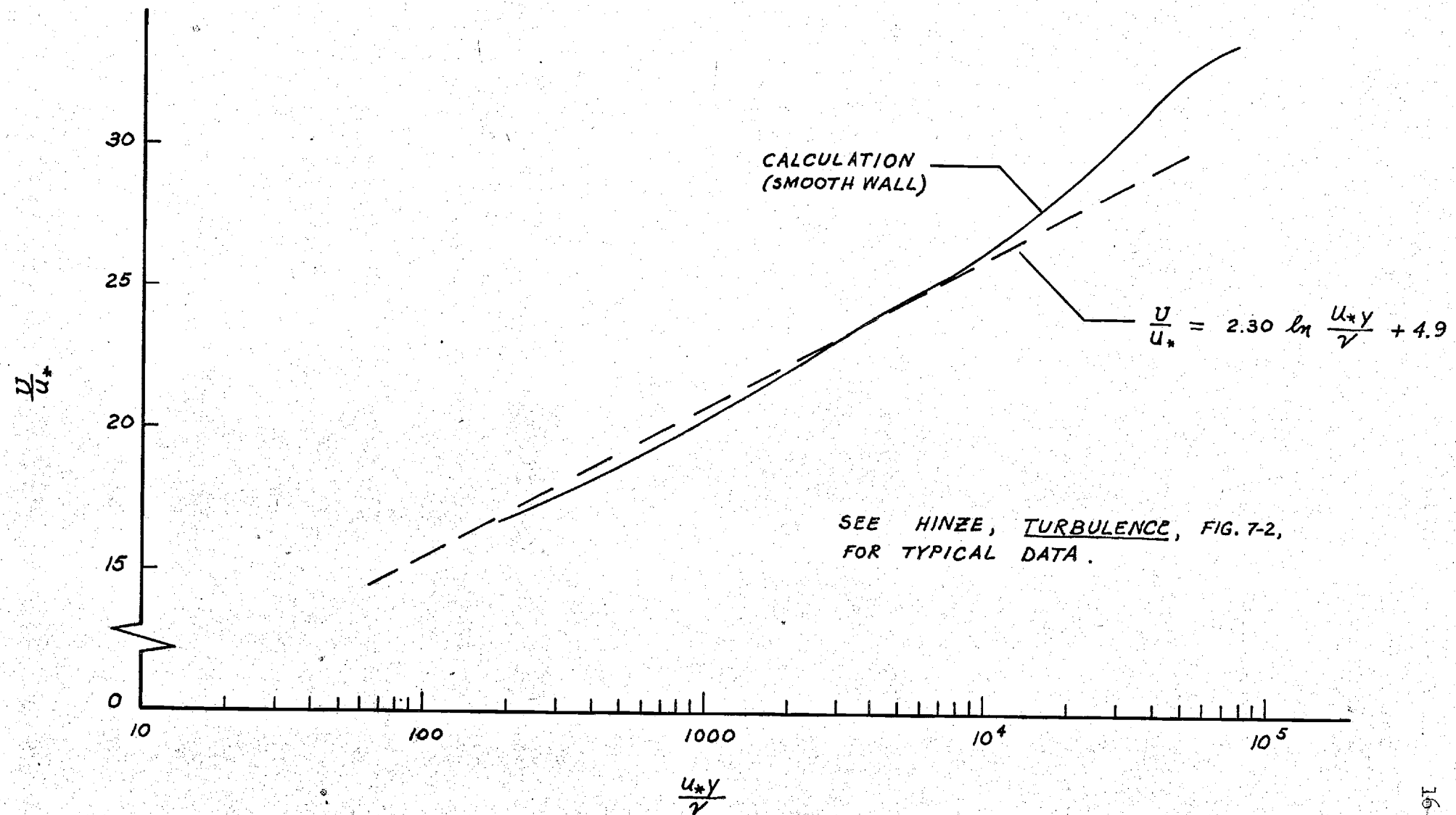
30
25
20
15
0
$\frac{U}{u_*}$
CALCULATION
(SMOOTH WALL)
$\frac{U}{u_*} = 2.30 \ln \frac{u_* y}{\nu} + 4.9$
SEE HINZE, TURBULENCE, FIG. 7-2,
FOR TYPICAL DATA.
10
100
1000
10^4
10^5
$\frac{u_* y}{\nu}$

FIGURE 4

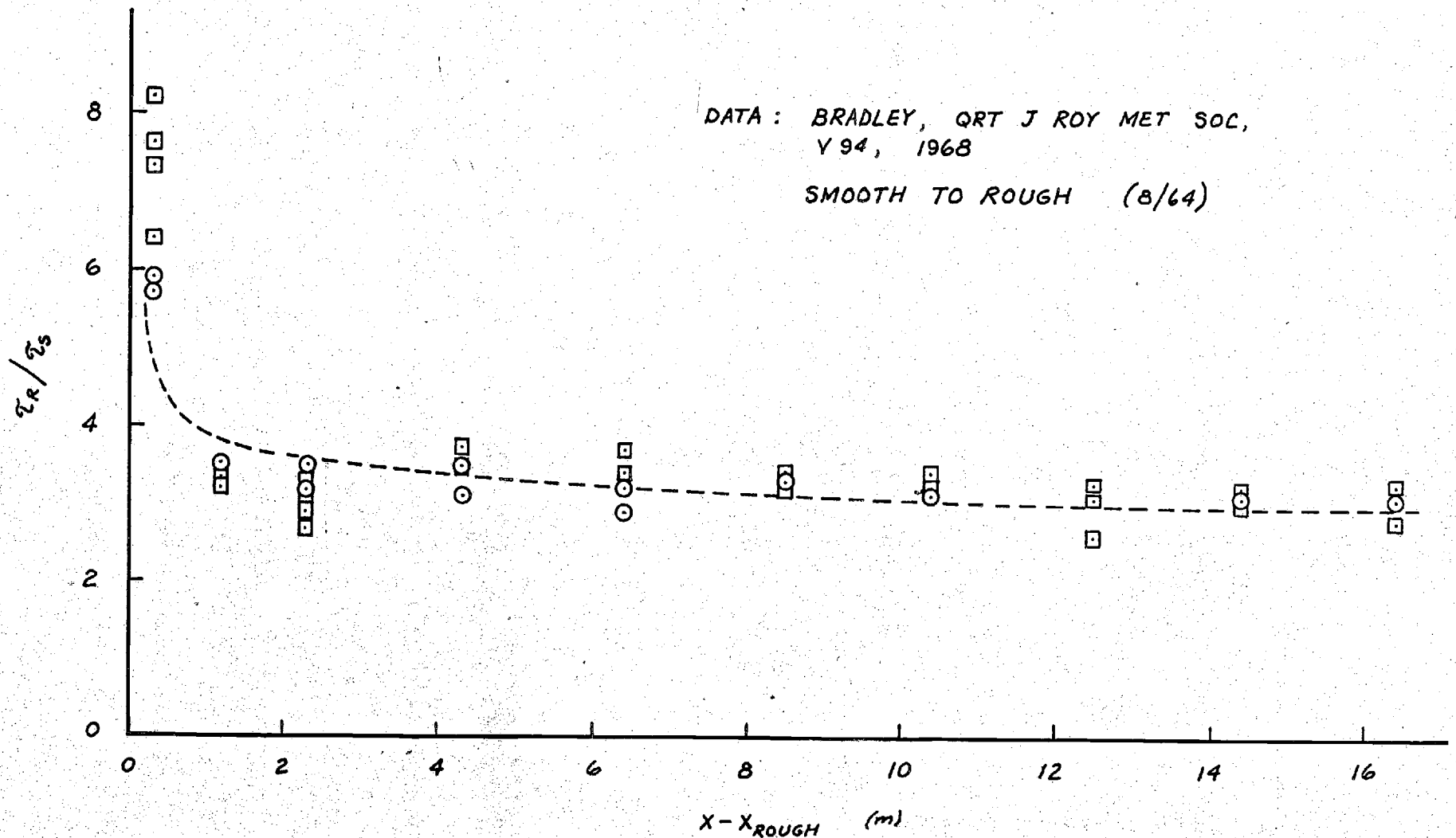
DATA : BRADLEY, QRT J ROY MET SOC, Y 94, 1968
SMOOTH TO ROUGH (8/64)
τ_R/τ_S
0
2
4
6
8
0
2
4
6
8
10
12
14
16
$X - X_{ROUGH}$ (m)

FIGURE 5

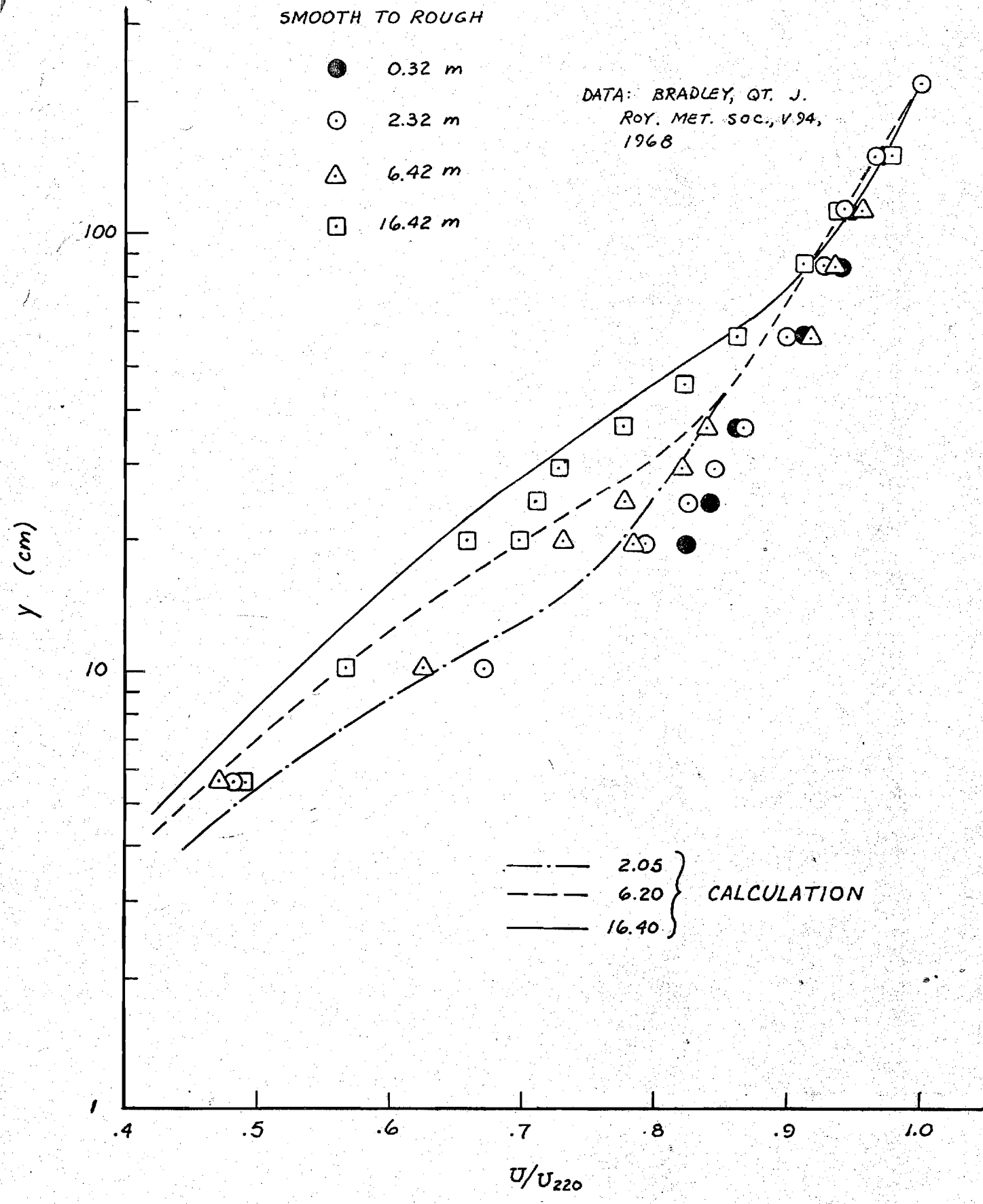
SMOOTH TO ROUGH
0.32 m
2.32 m
6.42 m
16.42 m
DATA: BRADLEY, QT. J. ROY. MET. SOC., V.94, 1968
100
10
1
Y (cm)
.4
.5
.6
.7
.8
.9
1.0
U/U220
2.05
6.20
16.40
CALCULATION

FIGURE 6

File: E-16-640

NASA Grant No. NGR-11-002-177

Semi-Annual Progress Report
March through August 1974

STUDY OF EFFECTS OF INJECTOR GEOMETRY ON FUEL-AIR MIXING AND COMBUSTION

by

Louis H. Bangert

School of Aerospace Engineering
Georgia Institute of Technology
Atlanta, Georgia 30332

Prepared for

NATIONAL AERONAUTICS AND SPACE ADMINISTRATION
Langley Research Center
Hampton, Virginia 23665
Mr. William B. Boatright, Technical Officer

ABSTRACT

This research program involves a series of experiments, and supporting analysis, to relate characteristics of fuel injector geometry to the turbulence produced and to the resultant hydrogen-air mixing and combustion. The accomplishments of the research program for the period March through August 1974 are described. In summary, these are: (1) a detailed experimental plan has been prepared, and (2) an approximation for the effect of turbulence on chemical reactions in flows with fast reactions has been developed.

1. INTRODUCTION

1.1 Background

Rapid fuel-air mixing and combustion in a supersonic stream are needed for the development of supersonic combustion ramjet engines for hypersonic flight. Optimum combustor design requires a knowledge of the relationship between heat-release distribution and fuel injector design. References 1 and 2 provide a general background for this subject. Recent experimental studies of scramjet injectors and related configurations are described in references 3-17. Related studies of base flow with mass addition[18-23] indicate that: (1) the effect of base and injector orifice geometry on base pressure is only partially known, and very little is known of their effect on turbulence properties in the near field; (2) for single-orifice injection, the base drag, turbulence energy and turbulence length scale are strongly affected by d_J/d_B, the ratio of fuel jet diameter to injector base diameter. In the present study, a series of experiments has been planned to determine the effect of d_J/d_B on hydrogen-air mixing and combustion. Some details of the experimental plan are given in section 2 of this report.

An associated analytical problem is the prediction of time-average reaction rate in a turbulent, reacting flow. Flows of the type being considered generally have high temperature, and have chemical kinetic reaction times that are much smaller than a characteristic time of the large-scale turbulence. These flows are often called "diffusion-limited" flows, because the rate of chemical reaction is limited by the rate at which the fuel and air are brought together by mixing. This subject will be discussed further in section 3 of this report, where an approximation for the effect of turbulence on chemical reactions is proposed.

1.2 Objective

The overall objective of this study is to relate the characteristics of fuel injector shape to the turbulence produced and to the resultant fuel-air mixing and combustion. The particular objective of this study is to determine the effect of d_J/d_B on hydrogen-air mixing and combustion.

2. EXPERIMENTAL PLAN

2.1 Apparatus and Instrumentation

The experiments of this study will be performed in the Langley Ceramic-Heated Wind Tunnel, which is an open-jet tunnel. The test gas, air or nitrogen, is heated by a zirconia pebble bed. The maximum stagnation temperature is 2220°K and the maximum stagnation pressure is 40.5 atmospheres. Further details of this facility are given in reference 24. The stagnation temperature of the test gas has been correlated with the pebble bed temperature by Sutton[25].

For the present experiments, the tunnel will use an axisymmetric Mach 2, stainless steel, water-cooled nozzle. The exit diameter of the nozzle is 6.53 cm (2.57 in). The fuel injectors have an outer diameter of 1.59 cm (5/8 in) and will be mounted along the nozzle axis. Figure 1 shows a sketch of the nozzle and injector.

The stagnation pressure of the test gas will be set so that the nozzle exit static pressure is 1 atm. For this condition, the test gas properties at the nozzle exit are approximately:

$M_\infty = 2.04$

$P_\infty = 14.7$ psia

$T_\infty = 1210$ K

$U_\infty = 1420$ m/sec

$\dot{m}_a = 1.31$ kg/sec $= 2.89$ lb_m/sec

$T_{o\infty} = 2220$ K

$P_{o\infty} = 122$ psia

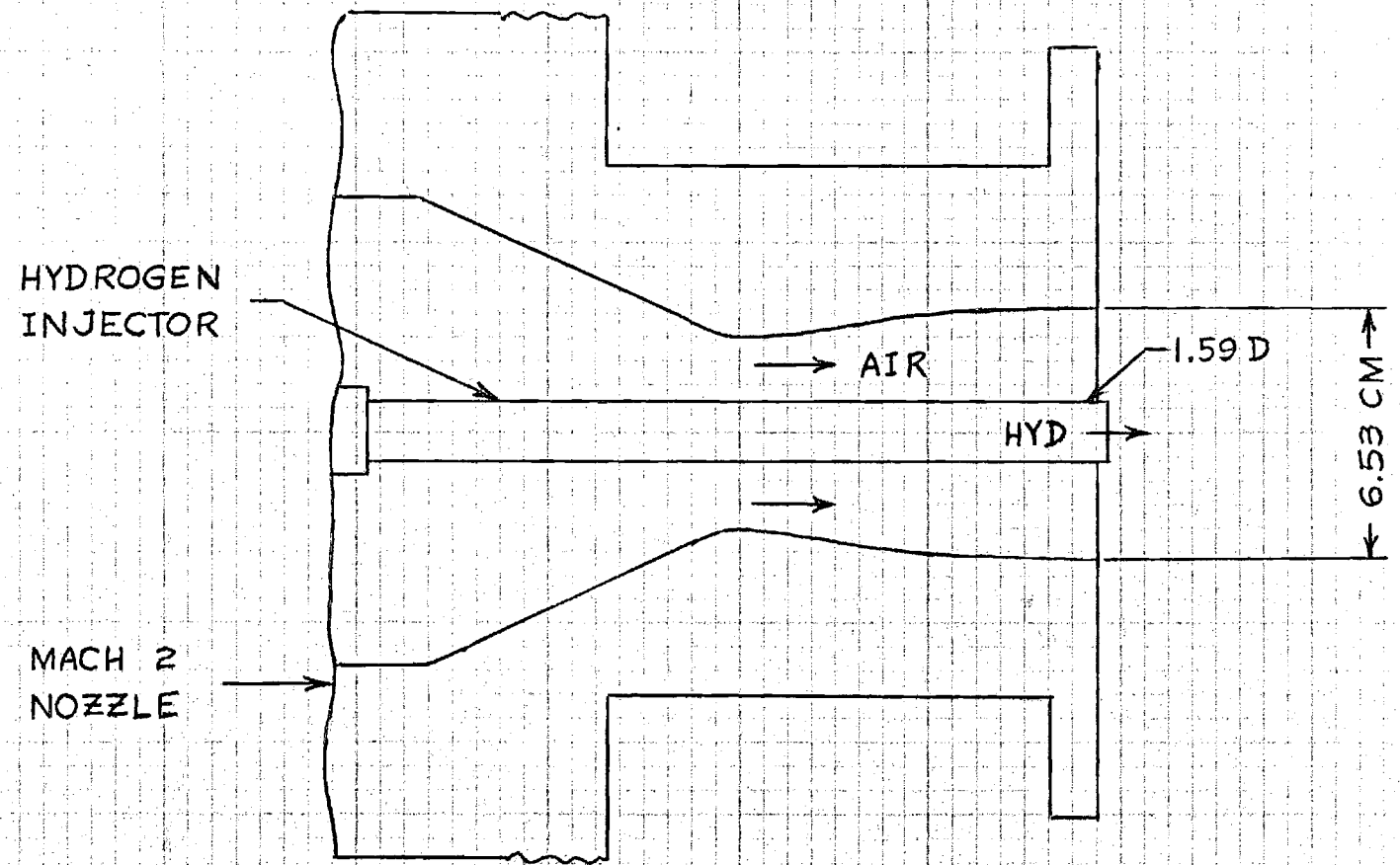

FIGURE 1. SKETCH OF WIND TUNNEL NOZZLE AND INJECTOR.

Three injectors will be tested. These injectors differ only in their values of d_J/d_B and in the shape of their internal nozzles. Sketches of these injectors are shown in Figure 2. The details of the designs are described in reference 26. Injector 1 has no internal nozzle, so that the tube wall thickness gives $d_J/d_B = 0.89$. Injectors 2 and 3 have internal converging nozzles with d_J/d_B equal to 0.60 and 0.48, respectively. The stagnation pressure of the hydrogen supply is adjusted to give the desired $\dot{m}_J$.

2.2 Types of Measurements

Three main types of measurements will be made: pitot pressures, species concentrations, and shadowgraph photographs. The pitot-pressure probe is of the same design as that described by Beach[11]. It is water-cooled, with a 0.63 cm (1/4 in) O.D. and a 30° tip half-angle. The measured pitot pressures will be recorded on magnetic tape, digitized, and computer-plotted.

The gas sampling probe for concentration measurements was designed by H. L. Beach, Jr. of NASA Langley. It is a water-cooled wedge with nine ports, and can simultaneously collect nine samples. The samples will be collected in sample bottles and then analyzed using a gas chromatograph. The amount of water that condenses in the sampling system will be inferred by a mass balance of oxygen. This is done by assuming that at each point oxygen and nitrogen are in the same proportion as in air. Then a measurement of the amount of nitrogen at a point will also indicate the total amount of oxygen at that point. The oxygen is divided among O_2, H_2O (g), and H_2O (ℓ). The first two of these are also measured.

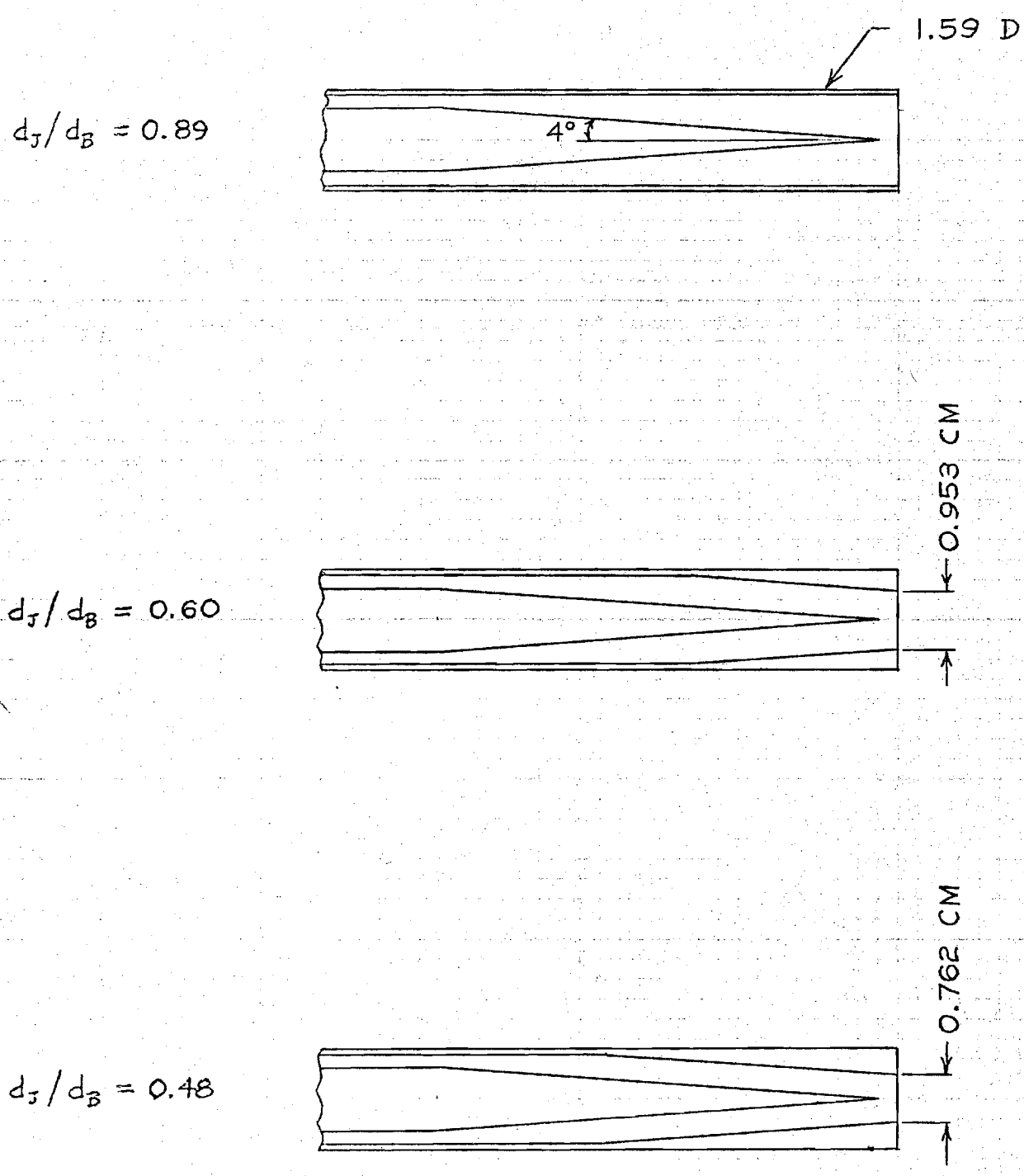

FIGURE 2. SKETCHES OF THE THREE INJECTORS

The shadowgraph is a part of the Langley Ceramic-Heated Wind Tunnel facility. These photographs will show shock waves and expansion waves and other regions of rapidly varying density. Some of the information that will be partially revealed by these shadowgraphs is: (1) regions where the pressure is different from P_∞ ; (2) the effects of combustion on wave angles and on the width of the mixing region; (3) the effect of changes in d_J/d_B on the width of the mixing region.

2.3 Run Schedule

Figure 3 gives the run schedule for the experiments. Figure 4 shows the test points on a plot of $\dot{m}_J/\rho_\infty U_\infty A_B$ versus $\rho_J U_J/\rho_\infty U_\infty$ with lines of d_J/d_B equal to 0.89, 0.60, and 0.48. Some of the experimental results that are expected to be significant are the effects of d_J/d_B and $\dot{m}_J/\rho_\infty U_\infty A_B$, with and without combustion, on:

(1) Centerline variation of pitot pressure;

(2) Variation of width of mixing region with axial distance;

(3) Pitot pressure profiles at different axial locations;

(4) Centerline variation of species mass fraction;

(5) Species mass fraction profile at different axial locations.

At the time of writing, repairs to the Langley Ceramic-Heated Wind Tunnel are nearing completion. It is now estimated that the experiments will begin in early September 1974.

RUN	d_J/d_B	$\dot{m}_J$ (GM/SEC)	TEST GAS	TYPE MEAS	PROFILE LOCATION (x/d_B)
1	0.60	7	AIR	PITOT	0, 2
2	"	"	"	"	4, 8, 16
3	"	"	"	SAMPLE	2
4	"	"	"	"	4
5	"	"	"	"	8
6	"	"	"	"	"
7	"	"	"	"	16
8	"	"	N_2	"	2
9	"	"	"	"	8
10	"	"	"	PITOT	2, 4, 8, 16
11-20	0.89	7			
21-30	0.48	7			
31-40	"	3			
41-50	0.89	3			
51-60	0.60	3			

FIGURE 3. RUN SCHEDULE

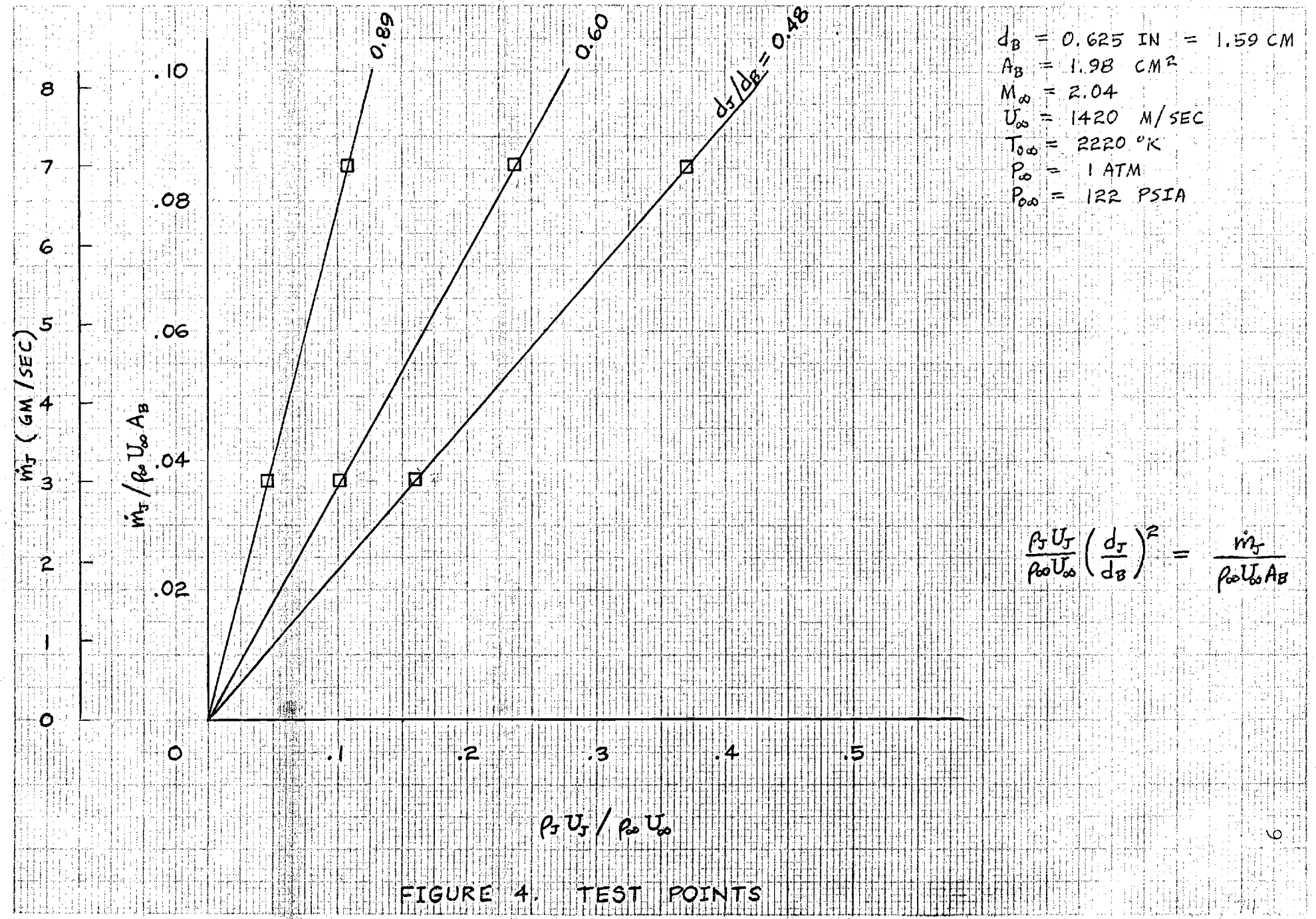

FIGURE 4. TEST POINTS

3. AN APPROXIMATION FOR THE EFFECT OF TURBULENCE ON CHEMICAL REACTIONS

3.1 Background

In the analysis of flow fields with chemical ractions, it is necessary to solve a species continuity equation for each specie involved in the reactions. For example, the general species continuity equation for specie f (fuel) is:

$$\frac{\partial}{\partial t}(\rho C_f) + \frac{\partial}{\partial x_i}(\rho u_i C_f) = \frac{\partial}{\partial x_i}\left(\rho D_f \frac{\partial C_f}{\partial x_i}\right) + \rho \dot{w}_f \tag{1}$$

Here $\dot{w}_f$ is the rate of production of specie f (negative for the fuel) caused by chemical reaction. Now assume that the chemical reaction is[27]:

$$a(\text{fuel}) + b(\text{oxidizer}) \xrightarrow{k} d(\text{product}) \tag{2}$$

where a, b and d are the number of moles. The rate constant k is given by:

$$k = k_o \exp\left[-\Delta E/RT\right] \tag{3}$$

Then the rate of generation of product, $\dot{w}_p$, is:

$$\dot{w}_p = K\, C_f^a\, C_o^b \exp\left[-(\Delta E/R)(T^{-1} - T^{*-1})\right] \tag{4}$$

where

$$K = k_o\left(dW_p/W_f^a\, W_o^b\right)\rho^{a+b-1} \exp\left(-\Delta E/RT^*\right) \tag{5}$$

The corresponding rate of depletion of the fuel f is:

$$\dot{w}_f = - \left(aW_f / dW_p \right) \dot{w}_p \qquad (6)$$

When the flow is turbulent, the usual procedure is to time-average (1). This introduces a term $\overline{\rho \dot{w}_f}$, which is theoretically obtainable from (4). This time-averaging of (4) introduces a number of unknown correlations, however. Spalding[28-30], Donaldson and Hilst[31], Chung[27], Libby[32], and Gibson and Libby[33] have treated this problem in different ways. A frequently-used procedure in the past was to replace each quantity in (4) by its time-average, in order to form $\overline{\rho \dot{w}_f}$. The above authors all point out that this is generally inaccurate for highly turbulent flows, and that an approximation for $\overline{\rho \dot{w}_f}$ is needed that better represents the influence of the turbulent fluctuations.

Spalding has proposed three models for $\overline{\rho \dot{w}_f}$. All are directed toward the case where the chemical reaction time is much less than a characteristic time for turbulent mixing, so that $\overline{\rho \dot{w}_f}$ is controlled by the rate at which the fuel and oxidizer are mixed. Spalding's first model[28] was applied to the case of initially unmixed reactants which react instantly on contact. He assumed that the instantaneous fuel-air ratio at a point, f, was equal to either $f_+ = \bar{f} + \overline{(f'^2)}^{0.5}$, or $f_- = \bar{f} - \overline{(f'^2)}^{0.5}$, and that f oscillated between these values. Spalding also introduced a modeled differential equation for $\overline{(f'^2)}^{0.5}$ to be solved simultaneously with the other flow equations. Thus, $\bar{f}$, f_+, and f_- can be calculated at each point. For each of these, the temperature and composition for equilibrium combustion can be computed. The calculated results indicate a flame of finite width,

which is qualitatively correct. The model has not been extensively compared with experiment, however.

Spalding's second and third models[29,30] were both developed for premixed flames, and are called the "eddy break-up" model. Each of these has $\overline{\rho \dot{w}_f}$ proportional to ϵ/q^2, which gives that the rate of chemical reaction is proportional to the rate of mixing of the larger eddies. These two models differ in that the first [29] has $\overline{\rho \dot{w}_f}$ proportional to the mean fuel mass fraction, while the second[30] has $\overline{\rho \dot{w}_f}$ proportional to the root-mean-square value of the fluctuation of fuel mass fraction. These models have achieved some success when compared with data for premixed flows. Their method of representing the dependence of $\overline{\rho \dot{w}_f}$ on the amount of each reactant present seems inadequate for flows that are not premixed, however.

Donaldson and Hilst[31] discuss in some detail the problem of representing $\overline{\rho \dot{w}_f}$. They do not propose an approximate closure that allows $\overline{\rho \dot{w}_f}$ to be calculated, however. Libby[32] also discusses the problem of fast chemical reactions in a turbulent flow, and emphasizes the effect of density fluctuations on the formulation. He also does not suggest a specific closure for $\overline{\rho \dot{w}_f}$, however.

In what follows, an approximation for $\overline{\rho \dot{w}_f}$ is proposed for the case where the chemical reaction time is much less than the turbulent mixing time. This is expected to be the usual case for the combustion of hydrogen in high-temperature air.

3.2 Proposed Relations between Mean Chemical Reaction Rate and Flow Turbulence

In this section, Chung's[27] analysis of homologous shear flow is used as the basis for modeling the effect of turbulence on reaction rate. Flow near solid boundaries will be excluded and large Reynolds number will

be assumed, so that turbulent transport is always much larger than molecular transport.

The one-dimensional flow analyzed by Chung is shown in the sketch below. In his analysis, ρ is constant, so that the velocity field is not

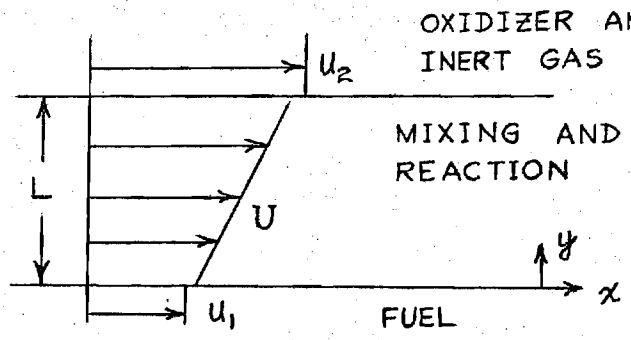

affected by the temperature field. Further, for this idealized flow, $\partial/\partial t = \partial/\partial x = \partial/\partial z = V = W = 0$. Molecular transport is also neglected compared to turbulent transport.

Following the usual procedure for turbulent flow, the Reynolds decomposition is introduced:

$$u_i = U_i + u_i'$$

$$C_f = \bar{C}_f + C_f' \qquad (7)$$

$$\rho = \bar{\rho} + \rho'$$

Taking the time average of (1) gives:

$$\frac{\partial}{\partial x_i}\left(\overline{\rho u_i C_f}\right) = \overline{\rho \dot{w}_f} \qquad (8)$$

When (8) is specialized to the flow studied by Chung[27], it becomes:

$$\frac{d}{dy}\left(\overline{v' C_f'}\right) = \overline{\dot{w}_f} \tag{9}$$

The details of Chung's[27] analysis can be found in his paper. Only the portions that are important for the present discussion will be repeated. First, the probability density $f(u_i', x_i)$ of the fluid elements was represented by the sum of two half-Maxwellian functions:

$$f = f_1 + f_2 \tag{10}$$

where for $v' > 0$,

$$f_1 = (3/2\pi E_1)^{1.5} \exp\left\{-(3/2E_1)\left[(u - u_1)^2 + v'^2 + w'^2\right]\right\}$$

$$f_2 = 0 \tag{11}$$

and for $v' < 0$,

$$f_1 = 0$$

$$f_2 = (3/2\pi E_2)^{1.5} \exp\left\{-(3/2E_2)\left[(u - u_2)^2 + v'^2 + w'^2\right]\right\} \tag{12}$$

A moment method was then used by Chung to solve for u_1, u_2, E_1 and E_2. These in turn determined mean velocity gradient, turbulence energy, and Reynolds stress.

Now let us consider Chung's[27] solution for temperature and mass fraction when the characteristic reaction time 1/K is much smaller than the characteristic time of the large eddies L/q. When the ratio of these times goes to zero, Chung's solution gives:

$$\overline{v'C_f'} = (E/6\pi)^{0.5} \quad (C_{f1} - C_{f2}) \tag{13}$$

where

$$C_f = C_{f1} + C_{f2}$$

and C_{f1} is zero for $v' < 0$ and C_{f2} is zero for $v' > 0$. In the combustion zone, C_{f2} is zero and

$$C_{f1} = 0.5 \ (aW_f/dW_p) \left[(m_1 + n_2) \ (1 - By/L)\right] + \text{constant} \tag{14}$$

where

$$m_1 = (dW_p/aW_f) \ C_{f1}$$

$$n_2 = (dW_p/bW_o) \ C_{O2}$$

and B is a constant related to the mean velocity gradient.

Although Chung did not explicitly do so, an equation for the reaction rate can be obtained by substituting (13) and (14) into (9):

$$\overline{\dot{w}_f} = - \ (aW_f/dW_p) \ (E/6\pi)^{0.5} \ (B/2L) \ (m_1 + n_2) \tag{15}$$

The following can also be inferred for the homologous shear flow:

$$m_1 = (dW_p/aW_f)\left[\bar{C}_f + g_f^{0.5}\right] \tag{16}$$

$$n_2 = (dW_p/bW_o)\left[\bar{C}_o + g_o^{0.5}\right] \tag{17}$$

$$(E/6\pi)^{0.5}\ (B/2L) = (3/8\pi)q/\ell \tag{18}$$

Here ℓ is the local integral scale of the turbulence. Substituting (16) - (18) into (15) gives:

$$\overline{\dot{w}_f} = -\ (3/8\pi)\ (q/\ell)\left[\bar{C}_f + g_f^{0.5}\right.$$

$$\left. +\ (aW_f/bW_o)\ (\bar{C}_o + g_o^{0.5})\right] \tag{19}$$

Equation (19) is a relation among $\overline{\dot{w}_f}$, q, ℓ, and the mass fractions of fuel and oxidizer. The rate q/ℓ is consistent with the condition that the turbulent motion controls the reaction rate. The quantity in brackets provides an estimate of the effect of the amount of each reactant on the reaction rate.

It is now proposed to assume that (19) is valid, at least approximately, for more complex flows than the one-dimensional shear flow analyzed by Chung. That is, assume that (19) remains a valid relationship among the quantities it contains, even though these quantities may vary from point to point in a complex way.

The hypothesis can be incorporated into a method of calculation as follows. First, make the approximation $\rho' = 0$, so that $\overline{\rho \dot{w}_f} = \bar{\rho}\,\dot{\bar{w}}_f$. Second, use a two-equation turbulence model with differential equations for q^2 and ϵ, and for convenience let

$$\ell = q^3/\epsilon \tag{20}$$

(20) is appropriate for flows with large Reynolds numbers. With (20), (19) becomes:

$$\overline{\dot{w}_f} = -A\,(\epsilon/q^2)\left[\bar{C}_f + g_f^{0.5} + (aW_f/bW_o)(\bar{C}_o + g_o^{0.5})\right] \tag{21}$$

The constant A is expected to be of order 0.1, but must be determined by comparison with experimental data. The dependence of $\overline{\dot{w}_f}$ on mass fraction, as given by the factor in brackets in (21), closely resembles a result derived by Gibson and Libby[33]. Their analysis was for a steady, laminar flow relative to a fixed flame front, with oxidizer and product on one side and fuel and product on the other. Thus, turbulence was not directly considered. Their steady, laminar solution has C_f instead of $\bar{C}_f + g_f^{0.5}$, and C_o instead $\bar{C}_o + g_o^{0.5}$.

Differential equations are also needed for g_f and g_o, as well as for q^2 and ϵ. An equation for g_f can be obtained as follows. First multiply (1) by C_f and take the time average:

$$\overline{C_f \frac{\partial}{\partial x_i}(\rho u_i C_f)} = \overline{C_f \frac{\partial}{\partial x_i}\left(\rho D_f \frac{\partial C_f}{\partial x_i}\right)} + \overline{\rho C_f \dot{w}_f} \tag{22}$$

Next, multiply (8) by $\bar{C}_f$ and subtract the result from (22):

$$\overline{C_f' \frac{\partial}{\partial x_i} (\rho u_i C_f)} = \overline{C_f' \frac{\partial}{\partial x_i} (\rho D_f \frac{\partial C_f}{\partial x_i})} + \overline{C_f' \rho \dot{w}_f} \tag{23}$$

The first two terms of (23) have been modeled previously; for example, by Spalding[34]. A suitable model is now needed for the last term.

If (22) is specialized for the one-dimensional flow studied by Chung[27], the result is:

$$\overline{C_f \frac{d}{dy} (v' C_f)} = \overline{C_f \dot{w}_f} \tag{24}$$

The left-hand side of (24) can also be written as $\overline{d(v' C_f^2/2)/dy}$. Using Chung's[27] solution to evaluate $\overline{v' C_f^2}$ gives:

$$\overline{C_f \dot{w}_f} = \left[C_f + g_f^{0.5} \right] \overline{\dot{w}_f} \tag{25}$$

Also,

$$\overline{C_f' \dot{w}_f} = \overline{C_f' \dot{w}_f'} \tag{26}$$

$$= \overline{C_f \dot{w}_f} - \bar{C}_f \bar{\dot{w}}_f$$

$$= g_f^{0.5} \overline{\dot{w}_f}$$

(26) can be used for the last term of (23) if the approximation $\rho = \bar{\rho}$ is again made. This latter approximation is not generally valid for flows with chemical reactions, but the error introduced cannot be accurately assessed at present.

3.3 Summary of Equations

At this point it is useful to list the equations to be solved. The solution will be carried out using the modified version of the Patankar-Spalding program[35] described in reference 36. As stated above, the approximation $\rho' = 0$ is made.

Continuity:

$$\frac{\partial}{\partial x}(\bar{\rho}Ur) + \frac{\partial}{\partial y}(\bar{\rho}Vr) = 0 \tag{27}$$

Conservation of x-momentum:

$$\bar{\rho}U\frac{\partial U}{\partial x} + \bar{\rho}V\frac{\partial U}{\partial y} = -\frac{dP}{dx} + \frac{1}{r}\frac{\partial}{\partial y}\left(r\mu_T\frac{\partial U}{\partial y}\right) \tag{28}$$

where the eddy viscosity is given by

$$\mu_T = C_\mu \bar{\rho} q^2 / 2\epsilon \tag{29}$$

where

$$\bar{C}_{\phi} = \bar{C}_o - (bW_o/aW_f)\ \bar{C}_f$$

(33) is easier to use than (32) in the numerical solution.

Conservation of $\overline{C_f'^2} = g_f$: From (23),

$$\bar{\rho}U \frac{\partial g_f}{\partial x} + \bar{\rho}V \frac{\partial g_f}{\partial y} = \frac{1}{r} \frac{\partial}{\partial y}\left(\frac{r\mu_T}{\sigma_g} \frac{\partial g_f}{\partial y}\right) \tag{34}$$

$$+ C_{g1}\, \mu_T \left(\frac{\partial \bar{C}_f}{\partial y}\right)^2 - C_{g2}\, \bar{\rho}^2 \left(q^2/2\right) g_f/\mu_T + 2\, \bar{\rho}\, g_f^{0.5}\, \dot{\bar{w}}_f$$

In (34) the first three terms on the right-hand side have been modeled in the form given by Spalding[34].

Conservation of $\overline{C_o'^2} = g_o$: From (34),

$$\bar{\rho}U \frac{\partial g_o}{\partial x} + \bar{\rho}V \frac{\partial g_o}{\partial y} = \frac{1}{r} \frac{\partial}{\partial y}\left(\frac{r\mu_T}{\sigma_g} \frac{\partial g_o}{\partial y}\right) \tag{35}$$

$$+ C_{g1}\, \mu_T \left(\frac{\partial \bar{C}_o}{\partial y}\right)^2 - C_{g2}\, \bar{\rho}^2 \left(q^2/2\right) g_o/\mu_T + 2\bar{\rho} g_o^{0.5}\, \dot{\bar{w}}_o$$

Conservation of turbulent kinetic energy:

$$\bar{\rho}U \frac{\partial}{\partial x}\left(q^2/2\right) + \bar{\rho}V \frac{\partial}{\partial y}\left(q^2/2\right) = \frac{1}{r} \frac{\partial}{\partial y}\left[\frac{r\mu_T}{\sigma_q} \frac{\partial}{\partial y}\left(q^2/2\right)\right] \qquad (36)$$

$$+ \mu_T \left(\partial U/\partial y\right)^2 - \bar{\rho}\epsilon$$

Conservation of ϵ:

$$\bar{\rho}U \frac{\partial \epsilon}{\partial x} + \bar{\rho}V \frac{\partial \epsilon}{\partial y} = \frac{1}{r} \frac{\partial}{\partial y}\left(\frac{r\mu_T}{\sigma_\epsilon} \frac{\partial \epsilon}{\partial y}\right) \qquad (37)$$

$$+ C_{\epsilon 1} \epsilon \mu_T \left(\frac{\partial U}{\partial y}\right)^2 / \left(q^2/2\right) - C_{\epsilon 2} \bar{\rho}\epsilon^2 / \left(q^2/2\right)$$

Equations (36) and (37) have been modeled from the exact equations in the form described by Launder and Spalding[37,38].

The differential equations to be solved are (27), (28), (30), (31), (33) - (37), plus an equation for the time-average mass fraction of nitrogen (N_2), $\bar{C}_N$. This last equation is the same as (33), with $\bar{C}_\phi$ replaced by $\bar{C}_N$. This set of differential equations is supplemented by algebraic equations of state, which assume a mixture of perfect gases. These equations are:

$$\bar{\rho} = PW_{mix}/R_u \bar{T} \qquad (35)$$

$$W_{mix} = \left(\sum_i \bar{C}_i / W_i \right)^{-1} \tag{36}$$

$$\bar{h} = C_{p,mix} \bar{T} = \bar{h}_o - \frac{1}{2} U^2 - H_f \bar{C}_f \tag{37}$$

$$C_{p,mix} = \sum_i \bar{C}_i C_{pi} \tag{38}$$

Calculations are now being made to compare the proposed model, equations (21) and (26), with experimental data. The calculations will be compared with the data of Cohen and Giule[5], and with the data of the present investigation.

4. SUMMARY

The principal accomplishments of this research program for the period March through August 1974 are:

(1) A detailed experimental plan has been prepared, including test conditions, run schedule, and consideration of methods of data presentation and analysis.

(2) An approximation for the effect of turbulence on chemical reactions in flows with fast chemical reactions has been developed. Calculations are now being made to compare predictions of this model with experimental data.

SYMBOLS

A_B	base area of injector, equal to $\pi d_B^2/4$ (m^2)
C_i	mass fraction of specie i
$C_{\epsilon 1}$, $C_{\epsilon 2}$	empirical constants in ϵ-equation, approximately equal to 1.43 and 1.92, respectively
C_{g1}, C_{g2}	empirical constants in equations for mean-square mass fraction fluctuations, approximately equal to 3.0 and 0.20, respectively
C_μ	empirical constant in relation among μ_T, q^2, and ϵ ; approximately equal to 0.09
c_{pi}	specific heat at constant pressure of specie i (joule/kg.K)
D	molecular diffusion coefficient (m^2/sec)
d_B	base diameter of injector (m)
d_J	fuel jet diameter (m)
f	probability density; i.e., the probability that a fluid element has velocity between u_i and $u_i + du_i$
g_i	$\overline{(c_i')^2}$
h	static enthalpy (joule/kg)
h_o	stagnation enthalpy (joule/kg)
H_f	heat of combustion of fuel (joule/kg)
k	chemical reaction rate coefficient (1/sec)
M	Mach number
$\dot{m}_a$	mass flow rate of test gas (air or nitrogen) through wind tunnel nozzle (kg/sec)
$\dot{m}_J$	mass flow rate of fuel (hydrogen) from injector (kg/sec)
P	pressure (newton/m^2)

P_o	stagnation pressure (newton/m^2)
q	$\left(\overline{u_i' u_i'}\right)^{0.5}$, the root-mean-square of the resultant velocity fluctuation (m/sec)
R	gas constant (joule/kg.K)
R_u	universal gas constant, 8314 joule/kg-mole.K
r	radial distance from the axis of symmetry (m)
T	temperature (K)
T_o	stagnation temperature (K)
T^*	temperature at chemical equilibrium (K)
t	time (sec)
u_i, U_i	instantaneous velocity and mean velocity in i-Cartesian coordinate direction (m/sec)
u, v, w	instantaneous velocity in x, y, z directions
U,V,W	mean velocity in x,y,z directions
W_i	molecular weight of specie i (kg/kg-mole)
$\dot{w}_i$	reaction rate of specie i (1/sec)
x_i	Cartesian coordinate in i-direction (m)
x, y, z	Cartesian coordinates, x in general direction of flow, y normal to plane of shear layer (m)

ΔE	activation energy (joule/kg)
ϵ	dissipation rate of turbulent kinetic energy (joule/kg.sec)
μ_T	eddy viscosity (newton.sec/m^2)
ρ	density (kg/m^3)
σ_j	turbulent Prandtl-Schmidt number for transport of quantity j
$\overline{( )}$	mean or time-average value of ( )
$( )'$	fluctuating part of ( ), e.g., equation (7)

Subscripts

f	fuel
J	fuel jet at injection location
N	nitrogen
o	oxygen
p	product of combustion
mix	mixture of gases
∞	free-stream conditions outside mixing region

REFERENCES

1. Ramjets, G. L. Dugger, editor, AIAA Selected Reprint Series, June 1969.

2. Henry, J. R. and Anderson, G. Y., "Design Considerations for the Airframe-Integrated Scramjet," 1st International Symposium on Air Breathing Engines, Marseille, France, June 19 - 23, 1972.

3. Cookson, R. A., Flanagan, P. and Penny, G. S., "A Study of Free-Jet and Enclosed Supersonic Diffusion Flames," 12th (Int.) Symposium on Combustion, July 1968. The Combustion Institute, 1969, 1115-1124.

4. Eggers, J. M. and Torrence, M. G., "An Experimental Investigation of the Mixing of Compressible Air Jets in a Coaxial Configuration," NASA TN D-5315, 1969.

5. Cohen, L. S. and Giule, R. N., "Measurements in Freejet Mixing/Combustion Flow," AIAA Journal, Vol. 8, June 1970, 1053-1061.

6. Bray, K. N. C., Fletcher, R. S. and Spalding, D. B., "Ignition and Combustion in Ducted Turbulent Supersonic Flow," AIAA Paper 70-720, June 1970.

7. Anderson, G. Y., Agnone, A. M. and Russin, W. R., "Composition Distribution and Equivalent Body Shape for a Reacting, Coaxial, Supersonic Hydrogen-Air Flow," NASA TN D-6123, January 1971.

8. Jacques, M. T., "Mixing and Combustion of Hydrogen in a Supersonic Airstream," Ph.D. Thesis, University of Sheffield Report H.I.C. 170, February 1971.

9. Eggers, J. M., "Turbulent Mixing of Coaxial Compressible Hydrogen-Air Jets," NASA TN D-6487, September 1971.

10. Metzler, A. J. and Mertz, T. W., "Preliminary Results of Large Supersonic Burning Combustor Testing," J. Aircraft, Vol. 9, January 1972, 23-30.

11. Beach, H. L., Jr., "Supersonic Mixing and Combustion of a Hydrogen Jet in a Coaxial High-Temperature Test Gas," AIAA Paper No. 72-1179, November 1972.

12. Burrows, M. C. and Kurkov, A. P., "Analytical and Experimental Study of Supersonic Combustion of Hydrogen in a Vitiated Air Stream," AIAA J. Vol. 11, September 1973, 1217-1218.

13. Kent, J. H. and Bilger, R. W., "Turbulent Diffusion Flames," 14th Int. Sym. on Combustion, August 1972, The Combustion Institute 1973, 615-624.

14. Anderson, G. Y. and Gooderum, P. B., "Exploratory Tests of Two Strut Fuel Injectors for Supersonic Combustion," February 1974, NASA TN-D-7581.

15. Drewry, J. E., Neer, M. E. and Scaggs, N. E.,"Supersonic Mixing and Combustion Studies of Ducted Hydrogen-Air Flows at an Inlet Air Mach Number of 2.6," AIAA Paper 73-1320, November 1973.

16. Alpinieri, L. J., "Turbulent Mixing of Coaxial Jets," AIAA J. Vol. 2, September 1964, 1560-1567.

17. Antonia, R. A. and Bilger, R. W., "An Experimental Investigation of an Axisymmetric Jet in a Co-Flowing Air Stream," J. of Fluid Mechanics, Vol. 61, 1973, 805, 822.

18. Lewis, J. E. and Behrens, W., "Fluctuation Measurements in the Near Wake of a Wedge with and Without Base Injections," AIAA J., Vol. 7, April 1969, pp. 664-670.

19. Lewis, J. E. and Chapkis, R. L., "Mean Properties of the Turbulent Near Wake of a Slender Body With and Without Base Injection," AIAA J. Vol. 7, May 1969, pp. 835-841.

20. Lewis, J. E., Behrens, W. and Collins, D. J., "Experimental Investigation of the Effects of Base Mass Addition on the Near Wake of a Slender Body,"AIAA J.,Vol.9, August 1971, pp. 1506-1513.

21. Bauer, A. B., "Near-Wake Injection Experiments," AIAA J., Vol. 6, Aug. 1968, pp. 1597-1599.

22. Valentine, D. T. and Prizirembel, C.E.G., "Turbulent Axisymmetric Near-Wake at Mach Four with Base Injection," AIAA J. Vol. 8, December 1970, pp. 2279-2280.

23. Matsumoto, I. R., Kimoto, K., and Tsuchimoto, N., "A Study on Double Concentric Jets," JSME Bulletin, V. 16, March 1973, 529-540.

24. Trout, O. F., Jr., "Design, Operation, and Testing Capabilities of the Langley 11-Inch Ceramic-Heated Tunnel," NASA TN D-1598, 1963.

25. Sutton, K., "Descriptions and Operation Parameters of a Mach 2 Nozzle System for the Langley 11-Inch Ceramic-Heated Tunnel," NASA TN D-4750, September 1968.

26. Bangert, L. H., "Study of Effects of Injector Geometry on Fuel-Air Mixing and Combustion," Progress Report 1, NGR-11-002-177, August 1973.

27. Chung, P. M., "Diffusion Flame in Homologous Turbulent Shear Flows," Physics of Fluids, Vol. 15, October 1972, 1735-1746.

28. Spalding, D. B., "Mathematische Modelle Turbulenter Flammen," V.D.I. Berichsheft 146, V.D.I. Verlag, Dusseldorf, 25, 1970.

29. Spalding, D. B., "Mixing and Chemical Reaction in Steady Confined Turbulent Flames," 13th (Int.) Symposium on Combustion, August 1970. The Combustion Institute, 1971, 649-657.

30. Lilley, D. G., "Turbulent Swirling Flame Prediction," AIAA Paper 73-651, July 1973.

31. Donaldson, C. duP. and Hilst, G. R., "Chemical Reactions in homogeneous Mixtures - The Effect of the Scale of Turbulent Mixing," Proc. Heat Transfer and Fluid Mechanics Institute, June 1972, 253-261, Stanford University Press.

32. Libby, P. A., "On Turbulent Flows with Fast Chemical Reactions. Part I: The Closure Problem," Combustion Science and Technology, Vol. 6, 1972, 23-28.

33. Gibson, C. H. and Libby, P. A., "On Turbulent Flows with Fast Chemical Reactions. Part II: The Distribution of Reactants and Products Near a Reacting Surface," Combustion Science and Technology, Vol. 6, 1972, 29-35.

34. Spalding, D.B., "Concentration Fluctuations in a Round Turbulent Free Jet," Chemical Engineering Science, Vol. 26, 1971, 95-107.

35. Patankar, S. V. and Spalding, D. B., Heat and Mass Transfer in Boundary Layers, 2nd ed., Intertext Books, London, 1970.

36. Bangert, L. H., "Study of Effects of Injector Geometry on Fuel-Air Mixing and Combustion," Semi-Annual Progress Report, September 1973-February 1974, NASA Grant NGR-11-002-177, February 1974.

37. Launder, B. E. and Spalding, D. B., "Turbulence Models and Their Application to the Prediction of Internal Flow," Heat and Fluid Flow, Vol. 2, January 1972, 43-54.

38. Launder, B. E., Morse, A. Rodi, W. and Spalding, D. B., "Prediction of Free Shear Flows - A Comparison of the Performance of Six Turbulence Models." In: Free Turbulent Shear Flows, NASA SP - 321, July 1972, 361-422.

NASA Grant No. NGR-11-002-177

Final Report

August 1977

STUDY OF EFFECTS OF INJECTOR GEOMETRY ON FUEL-AIR MIXING AND COMBUSTION

by

Louis H. Bangert

Robert L. Roach

School of Aerospace Engineering

Georgia Institute of Technology

Atlanta, Georgia 30332

Prepared for

NATIONAL AERONAUTICS AND SPACE ADMINISTRATION

Langley Research Center

Hampton, Virginia 23665

Mr. James M. Eggers, Technical Officer

ABSTRACT

An implicit finite-difference method has been developed for computing the flow in the near field of a fuel injector. This work was done as part of a broader study of the effects of fuel injector geometry on fuel-air mixing and combustion. Detailed numerical results have been obtained for cases of laminar and turbulent flow without base injection, corresponding to the supersonic base flow problem. These numerical results indicated that the method is stable and convergent, and that significant savings in computer time can be achieved, compared with explicit methods.

1.0 INTRODUCTION

This research program involved experiments and analysis to relate characteristics of fuel injector geometry to the fuel-air mixing and combustion. The original experimental program has been only partially completed at this time, because of numerous mechanical difficulties in the test facility and the instrumentation. References 1-3 give details of the experimental plan and also describe most of the experimental results and conclusions obtained to this point. In developing computational methods for the turbulent mixing and reacting flow, it became necessary to model the time-average rate of fuel consumption by chemical reaction at each point in the flow. References 3 and 4 describe the main results of this effort.

The present report is concerned with the last phase of the research program, which was the development of a numerical method for computing the flow properties in the near field of a fuel injector. This effort was a natural part of a study of effects of injector geometry on fuel-air mixing and combustion, because the principal effects of changes in injector geometry occur in the near field of the injector. This near field is of great interest for fuel injector design, because of the need for mixing and combustion of the reactants in minimum combustor length. Important features of the near field are: (1) regions of reverse flow (as at the base of an injector or downstream of transverse fuel jets); (2) turning of the fuel and air streams, with significant transverse pressure gradients; (3) shock waves and expansion waves (for supersonic air and/or fuel streams). It is not possible to use the boundary-layer form of the conservation equations to compute even the qualitative flow behavior near the injector. This is because the boundary-layer equations tell nothing about the three flow features named in the preceeding.

In developing the computational method and in calculating test cases, attention was directed toward a fuel injector in which the fuel jet emerged from the base of the injector. The method is not restricted to this type of injection, however. For example, transverse fuel injection into a supersonic stream could also be computed. No test cases have been computed for such a flow field as yet, however. When fuel injection is through the injector base, the flow field resembles that of the well-known base flow problem, but with the added complications of fuel injection and subsequent mixing and combustion. For this reason, the numerical method was first tested against the supersonic, laminar base flow calculations of Allen and Cheng[5], and then against the supersonic, turbulent base flow measurements of Lewis and Chapkis[13]. Both of these cases involve homogeneous, nonreacting flows. They serve to evaluate the capability of the numerical method to compute a flow with shocks, reverse flow, and a wide variety of boundary conditions. A sketch of this flow field is shown in Figure 1.

The specific objective of the present work was to develop a finite-difference method for computing the flow in the near field of a fuel injector. The general approach was to solve the time-average conservation equations for mass, momentum, energy, species, turbulence energy, and turbulence dissipation, subject to appropriate boundary conditions. These equations were written in time-dependent form, and the steady-state solution was taken to be the solution for large time. This is usually the more convenient approach from a numerical viewpoint[7]. The turbulence transport model was that of Launder and Spalding[8], modified for compressibility effects. The main feature of this model is that the turbulence velocity scale and length scale (macroscales) at each point are determined from modeled equations for k and ϵ. These then yield the eddy viscosity (proportional to $\rho k^2/\epsilon$) and the other turbulent transport coefficients (each proportional to eddy viscosity).

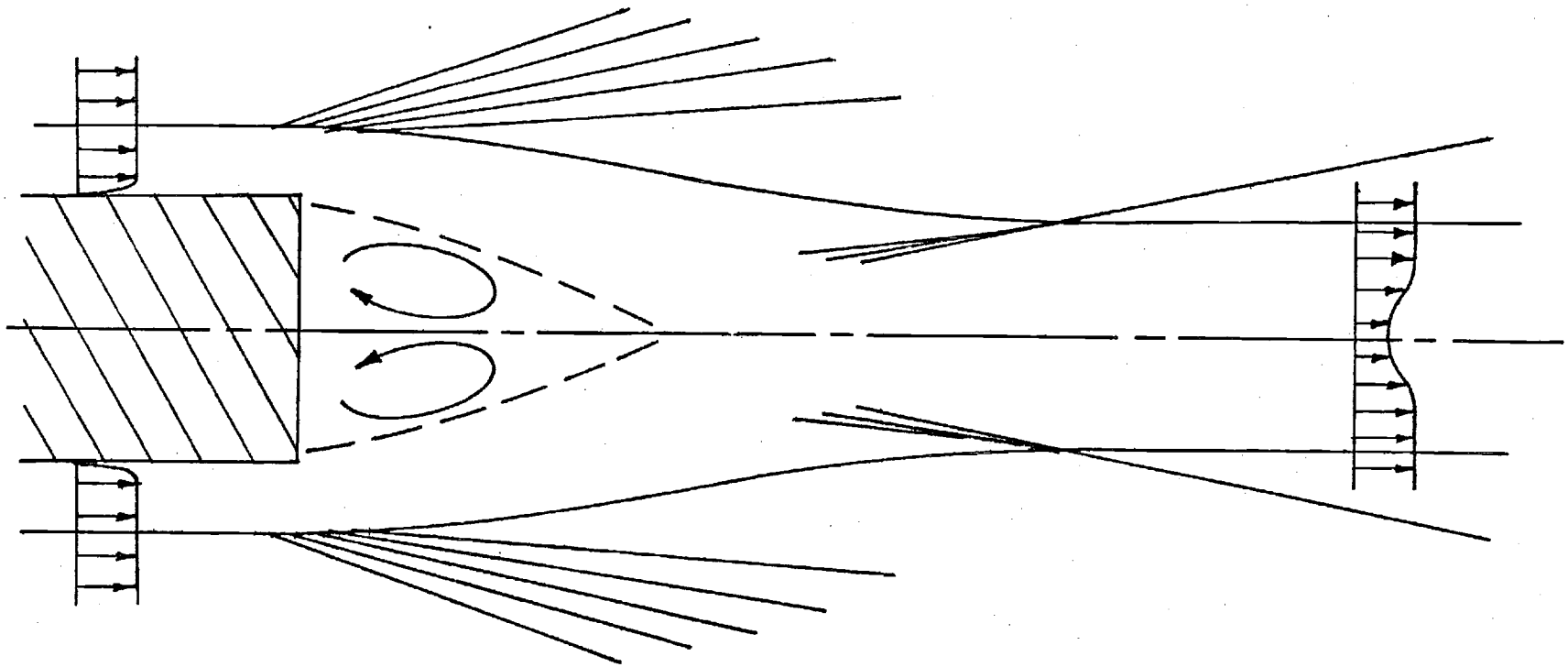

Figure 1. Sketch of flow field in the absence of base injection.

A comment may be made regarding the choice of a turbulent transport model that requires two additional partial differential equations, instead of a simpler mixing-length model. The attributes and defects of these approaches to turbulent transport modeling have been much discussed in recent years. It seems worthwhile to point out that there are some tradeoffs involved. For the mixing-length model, initial conditions are simplified, whereas initial conditions for k and ϵ are usually not available and must be guessed. On the other hand, it is difficult to specify an appropriate spatial mixing length distribution unless a great deal is already known about the flow. Finally, personal computational experience suggests that the ϵ-equation is not very well conditioned, in the sense that a poor choice of initial conditions or too coarse a grid may lead to difficulties in obtaining a numerical solution.

2.0 NUMERICAL METHOD

The numerical method used was based on that of Briley and McDonald[9,10]. As the method is implicit in time, it offers the possibility of significant reductions in computation time to obtain a steady-state solution. In the Briley-McDonald method, backward time differencing is applied to the conservation equations. Then these equations are linearized, with respect to time level, by a Taylor series expansion about the nth time level. (Flow properties are known at the nth time level from a previous calculation). Central differences are used to replace the spatial derivatives. The result is a system of simultaneous linear algebraic equations for the flow properties at the (n+1)th time level. An alternating direction implicit (ADI) technique is used to solve this system of equations.

In the present work attention has been restricted to two-dimensional plane flow. This was done because, considering the complexity of the flow, it seemed prudent to first develop the method for the simpler two-dimensional case.

Figure 2 illustrates the grid into which the flow field is subdivided and the corresponding nomenclature. The finite-difference forms of the conservation equations were derived by applying each of these equations to a control volume surrounding each grid point. This control volume is identical with the cell of dimensions Δx, Δy that encloses the grid point. (See Figure 2). This approach has distinct advantages. First, it tends to force the conservation laws to be satisfied macroscopically, not only in the limit as Δx, Δy, Δt go to zero (reference 7, p. 28). Second, it greatly aids in formulating boundary conditions, and helps assure that physically meaningful boundary conditions are applied[5].

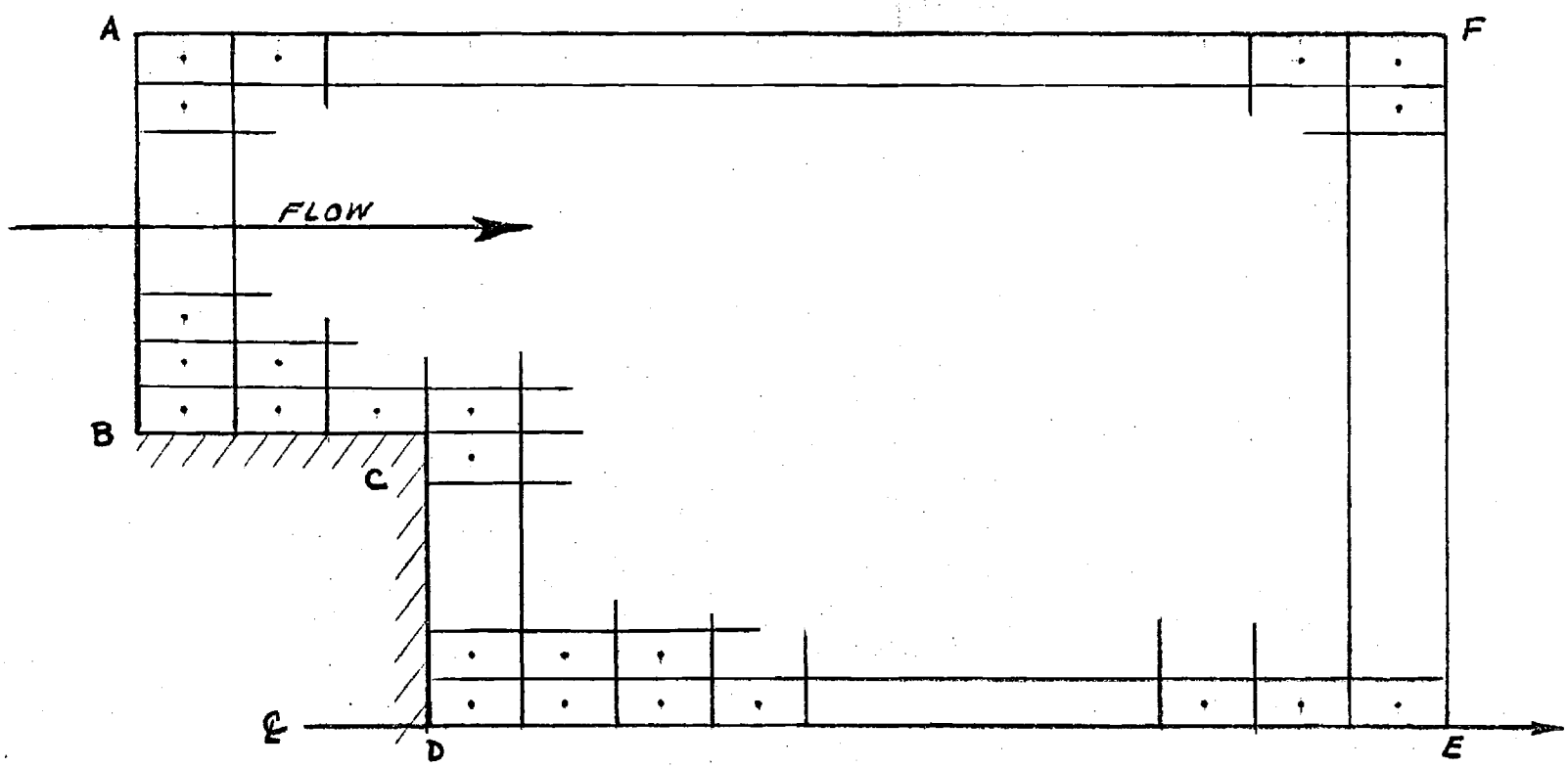

Figure 2. Flow geometry and computational field.

The derivation of the finite-difference forms of the conservation equations is given in Appendix A.

The linearization about time step n can be illustrated by considering the finite-difference equation for conservation of mass. From Appendix A, Eq. (A5), at point ij:

$$\partial\rho/\partial t = - \delta_x(\rho u) - \delta_y(\rho v) \tag{2-1}$$

Backward time-differencing is then applied to $\partial\rho/\partial t$, and the right-hand side is treated implicitly by evaluating it at the (n+1) level. Eq. (2-1) then becomes:

$$(\rho^{n+1} - \rho^n)_{ij}/\Delta t = - \delta_x(\rho u)^{n+1}_{ij} - \delta_y(\rho v)^{n+1}_{ij} \tag{2-2}$$

Eq. (2-2) is nonlinear in properties at the (n+1) level. So also are the remaining conservation equations after being differenced in the same way as conservation of mass. The full set of conservation equations in this finite-difference form is then a set of simultaneous nonlinear difference equations for flow properties at the (n+1) level. The solution of this set of equations would require some time-consuming iterative scheme[9].

To avoid an iterative solution, the right hand side of eq. (2-2) is linearized about the n level as follows:

$$(\rho^{n+1} - \rho^n)/\Delta t = - \delta_x \left[(\rho u)^n + (\partial\rho u/\partial t)^n \Delta t \right]$$

$$- \delta_y \left[(\rho v)^n + (\partial\rho v/\partial t)^n \Delta t \right] \tag{2-3}$$

The quantity $(\partial\rho u/\partial t)^n$ is expressed in finite-difference form as:

$$(\partial\rho u/\partial t)^n = (\rho^{n+1} - \rho^n)u^n/\Delta t + \rho^n(u^{n+1} - u^n)/\Delta t \tag{2-4}$$

Using this method for $(\partial\rho v/\partial t)^n$ and collecting terms, eq. (2-3) reduces to:

$$(\rho^{n+1} - \rho^n)/\Delta t = - \delta_x(\rho^{n+1}\, u^n + \rho^n\, u^{n+1} - \rho^n\, u^n)$$

$$- \delta_y(\rho^{n+1}\, v^n + \rho^n\, v^{n+1} - \rho^n\, v^n) \tag{2-5}$$

The subscript ij is to be understood in eqs. (2-3) to (2-5).

Equation (2-5) is linear in (n+1)-level variables. The other conservation equations can be treated in a similar way. This set of equations could be written in the form:

$$a^n\, \phi^{n+1}_{i+1,j} + b^n\, \phi^{n+1}_{i,j+1} + c^n\, \phi^{n+1}_{ij} + d^n\, \phi^{n+1}_{i,j-1}$$

$$+ e^n\, \phi^{n+1}_{i-1,j} = f^n \tag{2-6}$$

Here, a^n, b^n, etc., are matrices whose order is equal to the number of dependent variables. ϕ^{n+1} is a column vector whose components are the dependent variables. f^n is a column vector containing the same number of elements as there are dependent variables.

A set of multidimensional equations such as (2-6) is usually very time consuming to solve. Considerable time savings can be realized by splitting the multidimensional equation into a series of one-dimensional equations. This was done in the present case by applying the Douglas-Gunn[9] ADI method to each equation to obtain the intermediate steps. Each step involves implicit

solution in one of the coordinate directions. The solution of the resulting system of one-dimensional linear equations then only requires inversion of a tridiagonal matrix.

To illustrate the ADI method, consider the conservation of mass eq. (2-5). For the one-dimensional equations in the x-direction (x-sweep), (n+1)- level quantities are evaluated at an intermediate level, denoted by *. The exception is that the argument of δ_y is evaluated at the n - level. The result is:

$$(\rho^* - \rho^n)/\Delta t = - \delta_x(\rho^* u^n + \rho^n u^* - \rho^n u^n) - \delta_y(\rho^n v^n) \qquad (2\text{-}7)$$

Equation (2-7) is the x-sweep part of the conservation of mass equation.

The y-sweep equation is formed from eq. (2-5) by evaluating (n+1)-level quantities at ** , except for the argument of δ_x, in which (n+1)-level quantities are evaluated at *. Thus:

$$(\rho^{**} - \rho^n)/\Delta t = - \delta_x(\rho^* u^n + \rho^n u^* - \rho^n u^n) - \delta_y(\rho^{**} v^n + \rho^n v^{**} - \rho^n v^n) \qquad (2\text{-}8)$$

Finally, it is convenient to subtract eq. (2-7) from eq. (2-8) and use the result as the y-sweep equation. This is:

$$(\rho^{**} - \rho^*)/\Delta t = - \delta_y(\rho^{**} v^n + \rho^n v^{**} - 2\ \rho^n v^n) \qquad (2\text{-}9)$$

Quantities denoted by the superscript * are intermediate results obtained from the solution of the set of one-dimensional (x-direction) equations of which eq. (2-7) is a member. The other equations in this set are formed

from the other conservation equations in a manner similar to that of eq. (2-7). Likewise, each of the conservation equations is used to form y-sweep equations corresponding to eqs. (2-8) and (2-9). The use of eq. (2-9) instead of eq. (2-8) halves the storage requirement and reduces the computational effort. It has been shown[9] that ϕ^{**} is within order $(\Delta t)^2$ of ϕ^{n+1}, and so is taken as ϕ^{n+1}. The complete set of x-sweep and y-sweep equations is given in Appendix B.

The finite-difference forms of the conservation equations, such as eqs. (2-7) and (2-9), can be written in the following general form:

$$c_i^n \phi^*_{i-1,j} + b_i^n \phi^*_{ij} + a_i^n \phi^*_{i+1,j} = d_i^n \tag{2-10}$$

$$\gamma_j^n \phi^{**}_{i,j-1} + \beta_j^n \phi^{**}_{ij} + \alpha_j^n \phi^{**}_{i,j+1} = \xi_j^* + \eta_j^n \tag{2-11}$$

Here c, b, a, γ, β, and α are two-dimensional matrices. ϕ is the dependent variable column matrix, and d, ξ, and η are column matrices.

The solution procedure for a single time step is as follows. First, eq. (2-10) is applied to successive rows (x-direction) to generate a set of coupled, one-dimensional equations. These implicit equations are arranged into a block tridiagonal matrix for each row, and solved for ϕ^* by a standard elimination technique. Second, eq. (2-11) is applied to successive columns (y-direction). Following the same procedure, ϕ^{**} is computed at each grid point.

The technique used to solve these equations is the LU decomposition and back-substitution (LUBS) method of Isaacson and Keller[11]. A discussion of the application of this method to the present problem is given in reference 3.

3.0 BOUNDARY CONDITIONS

The finite-difference equations have the same form for each of the interior grid points. These equations must be modified for cells which are adjacent to the boundaries of the computational field, however, to properly represent the physical boundary conditions. The particular boundary conditions are described here relative to the injector flow field sketch in Figure 2.

3.1. Upper Wall (BC)

Consider the cell with grid point ij adjacent to wall BC. (See Figure 3). Because this is an impermeable wall,

$$(v)_{y-} = 0 \tag{3-1}$$

Also, to satisfy the no-slip condition,

$$(u)_{y-} = 0 \tag{3-2}$$

In the x-momentum equation, the nondimensional shear stress at the wall is $\left[(\mu_T + \mu/R_1)s_{xy}\right]_{y-}$. Thus,

$$\left[(\mu_T + \mu/R_1)s_{xy}\right]_{y-} = \rho_{ij}\, u_*^2 \tag{3-3}$$

and u_* is calculated from the Law of the Wall for a smooth wall:

$$u_{ij}/u_* = (1/\kappa)\, \ell n \left[(\rho y/\mu)_{ij}\, u_*\, R_1\right] + 5 \tag{3-4}$$

In applying (3-4), care was taken that $(\rho y/\mu)_{ij}\, u_*\, R_1 > 30$. It was also assumed that eq. (3-4) was valid between (y-) and (y+). Then, $\partial u/\partial y = u_*/\kappa y$. This provided a method of treating the shear stress terms in the y-momentum equation. Thus,

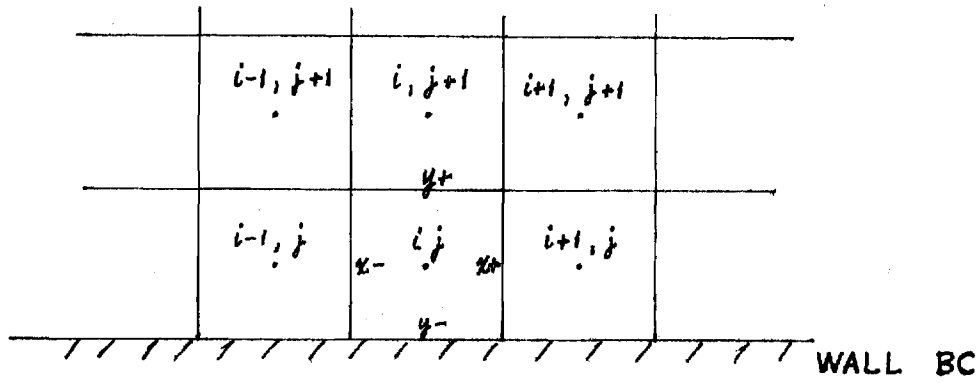

Figure 3. Cell adjacent to wall BC.

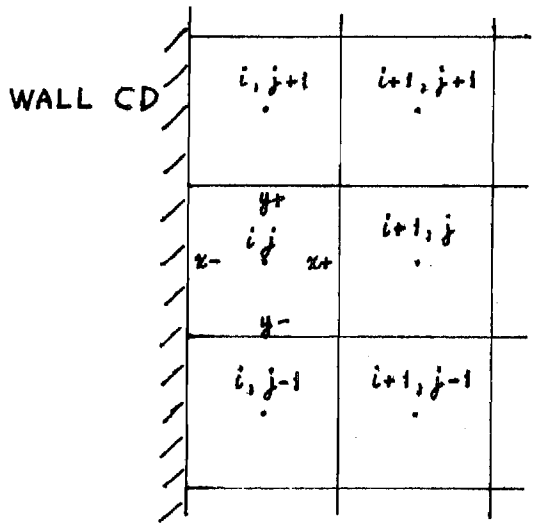

Figure 4. Cell adjacent to wall CD.

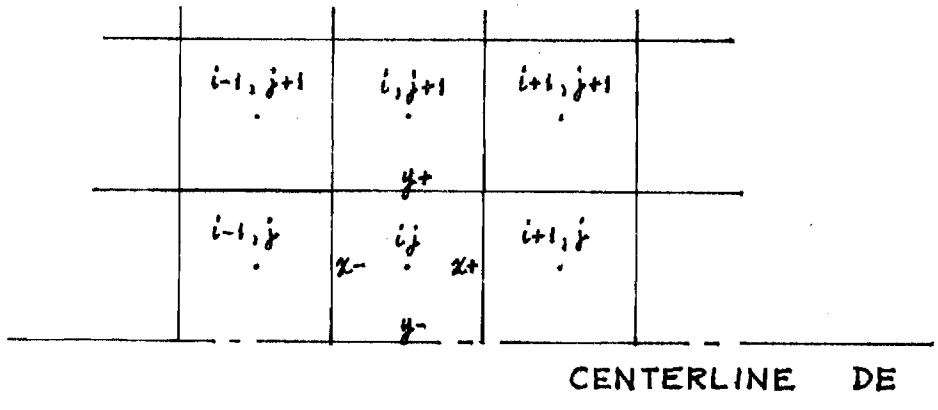

Figure 5. Cell adjacent to centerline DE.

$$\left[(\mu_T + \mu/R_1)s_{xy}\right]_{x+} = \left[(\mu_T + \mu/R_1)\partial v/\partial x\right]_{x+} + (\rho u_*^2)_{x+} \qquad (3\text{-}5)$$

and similarly for $\left[(\mu_T + \mu/R_1)s_{xy}\right]_{x-}$.

The nondimensional pressure at the wall is equal to $(\rho e)_{y-}$. This quantity was evaluated by a linear extrapolation through (ij) and (i,j+1), so that,

$$(\rho e)_{y-} = 1.5\ (\rho e)_{ij} - 0.5\ (\rho e)_{i,j+1} \qquad (3\text{-}6)$$

Because of eq. (3-2), it was also required that,

$$(\partial u/\partial x)_{y-} = 0 \qquad (3\text{-}7)$$

Normal derivatives at a surface were represented by a second-order accurate, one-sided difference approximation[5]:

$$(\partial\phi/\partial y)_{y-} = (-8\ \phi_{y-} + 9\ \phi_{ij} - \phi_{i,j+1})/3\ \Delta y \qquad (3\text{-}8)$$

This gives:
$$(\partial v/\partial y)_{y-} = (9\ v_{ij} - v_{i,j+1})/3\ \Delta y \qquad (3\text{-}9)$$

Because turbulent velocity fluctuations go to zero at a solid boundary, it was required that,

$$(\mu_T)_{y-} = 0 \qquad (3\text{-}10)$$

and,

$$(k)_{y-} = 0 \qquad (3\text{-}11)$$

Following the approach used in eq. (3-5), the condition,

$$\left[(\mu_T + \mu/R_1)(\partial u/\partial y)\right]_{x+} = (\rho u_*^2)_{x+} \tag{3-12}$$

was imposed, and similarly for the value at x-.

For the present calculations, it was assumed that the wall was adiabatic. Then,

$$(q_y)_{y-} = - (\partial e/\partial y)_{y-} = 0 \tag{3-13}$$

It was assumed that there is no variation in composition normal to the wall at the wall. Thus,

$$(\partial C_a/\partial y)_{y-} = 0 \tag{3-14}$$

The Law of the Wall was also used to determine certain quantities at (ij). Thus,

$$(\partial u/\partial y)_{ij} = u_*/\kappa\, y_{ij} \tag{3-15}$$

$$k_{ij} = u_*^2/C_\mu^{0.5} \tag{3-16}$$

$$\epsilon_{ij} = u_*^3/\kappa\, y_{ij} \tag{3-17}$$

3.2 Back Wall (CD)

Now consider the cell with grid point (ij) whose (x-) edge coincides with the back wall. (See Figure 4).

For an impermeable wall,

$$(u)_{x-} = 0 \tag{3-18}$$

and for no slip at the wall,

$$(v)_{x-} = 0 \tag{3-19}$$

Also from eqs. (3-18) and (3-19):

$$(\partial u/\partial y)_{x-} = 0 \tag{3-20}$$

$$(\partial v/\partial y)_{x-} = 0 \tag{3-21}$$

Using eq. (3-8) for normal derivatives at the wall gives:

$$(\partial u/\partial x)_{x-} = (9\, u_{ij} - u_{i+1,j})/3\, \Delta x \tag{3-22}$$

and

$$(\partial v/\partial x)_{x-} = (9\, v_{ij} - v_{i+1,j})/3\, \Delta x \tag{3-23}$$

The pressure at the back wall was obtained in the same way as on the upper wall by eq. (3-6).

$$(\rho e)_{x-} = 1.5(\rho e)_{ij} - 0.5(\rho e)_{i+1,j} \tag{3-24}$$

For an adiabatic wall,

$$(q_x)_{x-} = -(\partial e/\partial x)_{x-} = 0 \tag{3-25}$$

Because of eqs. (3-18) and (3-19), the shear-work terms are zero:

$$(s_{ix}\, u_i)_{x-} = 0 \tag{3-26}$$

At the wall, the turbulent velocity fluctuations are zero. Thus

$$(k)_{x-} = 0 \tag{3-27}$$

and,

$$(\mu_T)_{x-} = 0 \tag{3-28}$$

Also, similar to eq. (3-14), the assumption was made that,

$$(\partial C_a/\partial x)_{x-} = 0 \qquad (3\text{-}20)$$

3.3 Centerline (DE)

Because DE is a plane of symmetry, there is no mass flux across it. Figure 5 shows a typical cell adjacent to DE.

$$(v)_{y-} = 0 \qquad (3\text{-}30)$$

This also gives,

$$(\partial v/\partial x)_{y-} = 0 \qquad (3\text{-}31)$$

and, $$(\partial v/\partial y)_{y-} = (9v_{ij} - v_{i,j+1})/3\Delta y$$

Also because of symmetry,

$$(\partial \phi/\partial y)_{y-} = 0 \qquad (3\text{-}32)$$

Combining eq. (3-32) with eq. (3-8) gives a formula for any dependent variable except v at (y-):

$$\phi_{y-} = (9/8)\phi_{ij} - (1/8)\phi_{i,j+1} \qquad (3\text{-}33)$$

Equations (3-30) through (3-32) also give:

$$(s_{iy}\, u_i)_{y-} = 0 \qquad (3\text{-}34)$$

3.4 Outflow Boundary (EF)

For this case the x+ cell boundary is located along EF. The approach followed here was the same as that recommended by Roache (reference 7, pp. 279-281). Properties at (ij) are determined by a linear extrapolation

through (i-1,j) and (i-2,j), giving:

$$\phi_{ij} = 2\phi_{i-1,j} - \phi_{1-2,j} \tag{3-35}$$

3.5 Upper Boundary (AF)

The cell with grid point (ij) has its y+ edge along AF. Flow properties at (ij) were determined by considering the straight left-running characteristic that passes through (ij). Properties are approximately constant along this characteristic, and can be determined by suitable interpolation from the properties at (i-1,j-1) and (i,j-1), or (i-1,j-1) and (i-1,j). The procedure is described by Roache (reference 7, pp. 282-283). Referring to Figure 6a, when $\tan (\mu_M + \theta)_{i-1,j-1} > \Delta y/\Delta x$, then:

$$\phi_p = \phi_{i-1,j-1} + (\ell/\Delta x)(\phi_{i,j-1} - \phi_{i-1,j-1}) \tag{3-36}$$

By this approximation, $\phi_p = \phi_{ij}$. Next, let

$$w_p' = \tan\left[90^o - (\mu_M + \theta)_p\right]$$

Now, $w_p' = (\Delta x - \ell)/\Delta y$ by geometry. An expression for w_p' can also be obtained from eq. (3-36). Equating these two and solving for ℓ gives,

$$\ell = (\Delta x/\Delta y - w'_{i-1,j-1}) \; / \left[(w'_{i,j-1} - w'_{i-1,j-1}) \; / \; \Delta x + 1/\Delta y\right] \tag{3-37}$$

when $\tan (\mu_M + \theta)_{i-1,j-1} > \Delta y/\Delta x$.

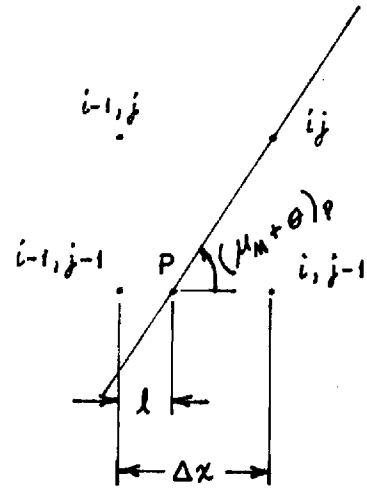

Figure 6a. Upper boundary AF. $\tan(\mu_M + \theta)_{i-1,j-1} > \Delta y/\Delta x$.

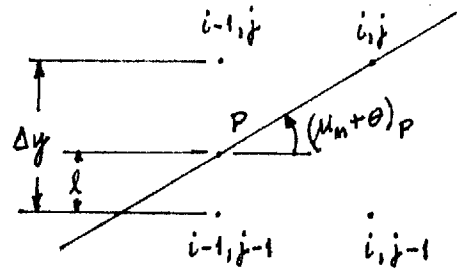

Figure 6b. Upper boundary AF. $\tan(\mu_M + \theta)_{i-1,j-1} < \Delta y/\Delta x$.

Next, consider Figure 6b, which depicts the case when $\tan (\mu_M + \theta)_{i-1,j-1} < \Delta y/\Delta x$. Let,

$$w_p = \tan (\mu_M + \theta)_p$$

For constant properties along a left-running characteristic,

$$\phi_p = \phi_{i-1,j-1} + (\ell/\Delta y)(\phi_{i-1,j} - \phi_{i-1,j-1}) \tag{3-38}$$

Also, by geometry, $w_p = (\Delta y - \ell)/\Delta x$. As before, these relationships yield a formula for ℓ:

$$\ell = (\Delta y/\Delta x - w_{i-1,j-1}) / \left[(w_{i-1,j} - w_{i-1,j-1})/\Delta y + 1/\Delta x\right] \tag{3-39}$$

for $\tan (\mu_M + \theta)_{i-1,j-1} < \Delta y/\Delta x$.

Equations (3-37) and (3-39) are then used in eqs. (3-36) and (3-38), respectively, to compute the remaining properties at p.

3.6 Inflow Boundary (AB)

Flow properties at the inflow boundaries were specified and kept fixed as the solution developed in time.

4.0 RESULTS

In this section some results of computations using the present numerical method are given. Two sets of calculations are described. The first is for a supersonic, laminar base flow at conditions previously computed by Allen and Cheng[5]. The second is for a supersonic, turbulent base flow at the conditions of the experiments of Lewis and Chapkis.[12]

The laminar flow case is simpler, as it involves fewer differential equations (four). These laminar flow calculations have been very important to the program development, because they have served to establish effects of variations in boundary conditions, grid size, time step, and other parameters, without the additional complications of turbulent flow. Some of this work is still continuing, as indicated in what follows. These calculations have also served to establish that the numerical method is stable and convergent.

The laminar flow calculations were made for $M_1 = 3$, $R_1 = 550$, and nondimensional initial boundary-layer thickness $\delta = 0.41$. The initial u-profile was the polynomial in y used by Allen and Cheng. The corresponding v was obtained from the continuity and x-momentum boundary-layer equations.[5] e was given by the Busemann integral for an adiabatic wall, and p was uniform and equal to its freestream value. The computational mesh size was $\Delta x = 1/6$ and $\Delta y = 1/12$. This is coarser than that used by Allen and Cheng, and was chosen to increase economy while retaining reasonable accuracy during program development. The computational time step used was four times the Courant-Friedricks-Lewy (CFL) time step, which is the maximum time step for stable calculation using an explicit, finite-difference method. Stable and convergent solutions were obtained with the larger time step using the present implicit method, thus demonstrating potentially large savings in computer time.

Figures 7 - 13 show computed results for the laminar flow case

described in the preceding. Figure 7 shows the field of velocity vectors. All the main features of the flow are evident here, including the initial boundary layer, the expansion and turning at the corner, the weak recompression shock and turning downstream, the recirculation region near the base, and the retarded flow near the plane of symmetry. The location of the rear stagnation point is about 20% closer to the base than that calculated by Allen and Cheng.[5] The dividing streamline separates just below the corner, in agreement with previous experiments and calculations.[5]

The streamline plot of Figure 8 shows the flow turning due to expansion and recompression even more clearly. Also, the recirculation region and the dividing streamline are indicated. The pressure contours of Figure 9 very effectively illustrate the corner expansion and the recompression shock. Also note that downstream of the recirculation region there is a growing region where $\partial p/\partial y \cong 0$ near the plane of symmetry. Results of this kind indicate the region of validity of the boundary-layer equations, which are usually used to describe the wake at some distance from the body. The density contours of Figure 10 also show the expansion and recompression. For the case of an adiabatic wall, the density near the wall is less than the free-stream value, and this is indicated in the solution. Corresponding internal energy contours are shown in Figure 11.

The computed centerline pressure distribution is given in Figure 12. Also shown are the calculated results of Allen and Cheng.[5] The two are in close agreement.

Centerline Mach number distribution is shown in Figure 13. This figure illustrates the extent of the recirculation region and the acceleration of the flow in the downstream direction. Downstream of the region of the present computation, the centerline Mach number will exceed one. A short

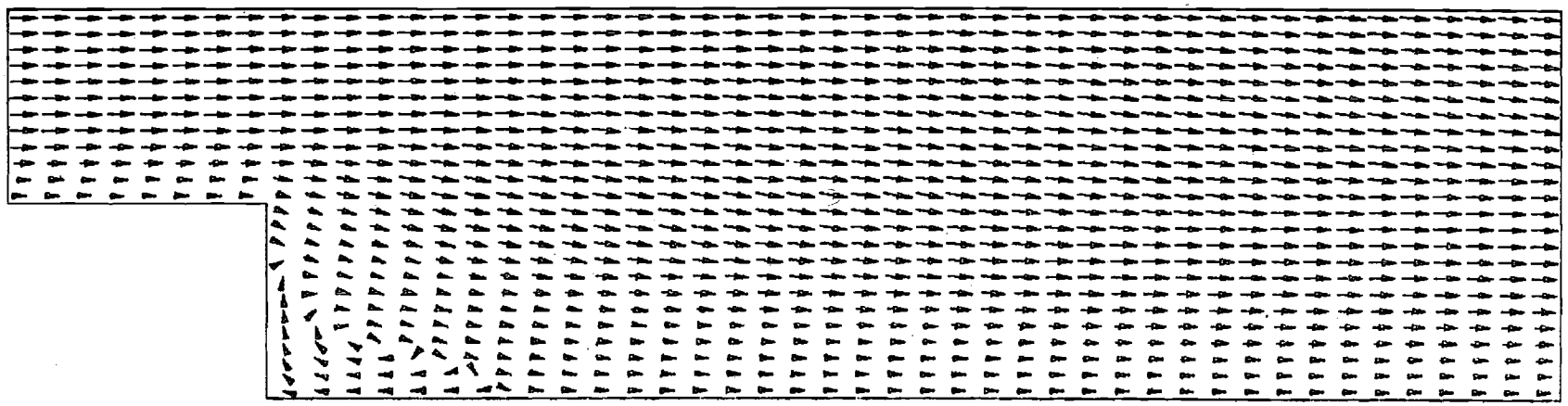

Figure 7. Velocity vectors. Laminar flow.

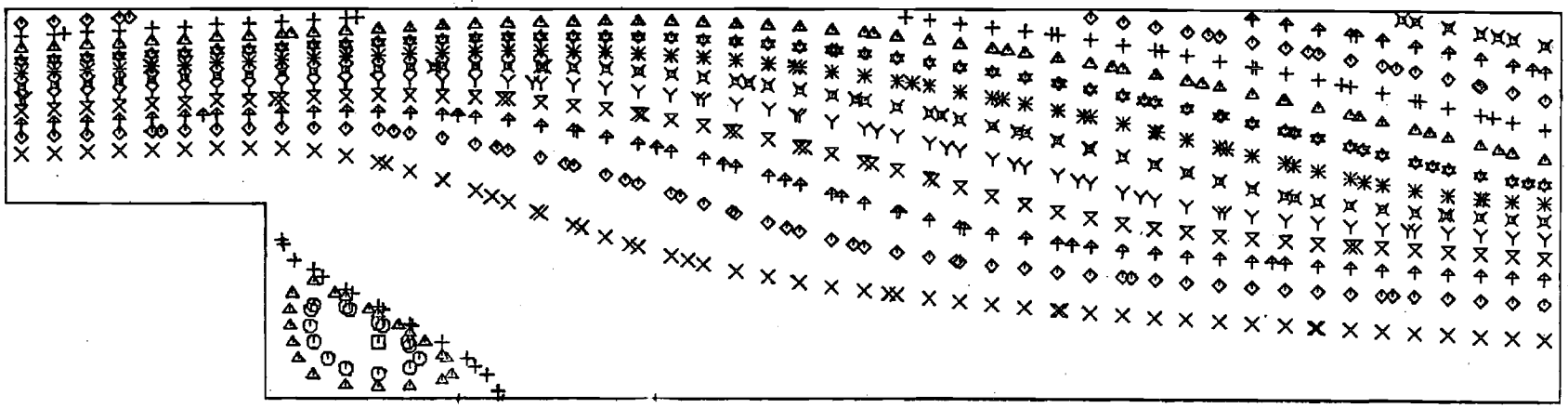

Figure 8. Streamlines. Laminar flow.

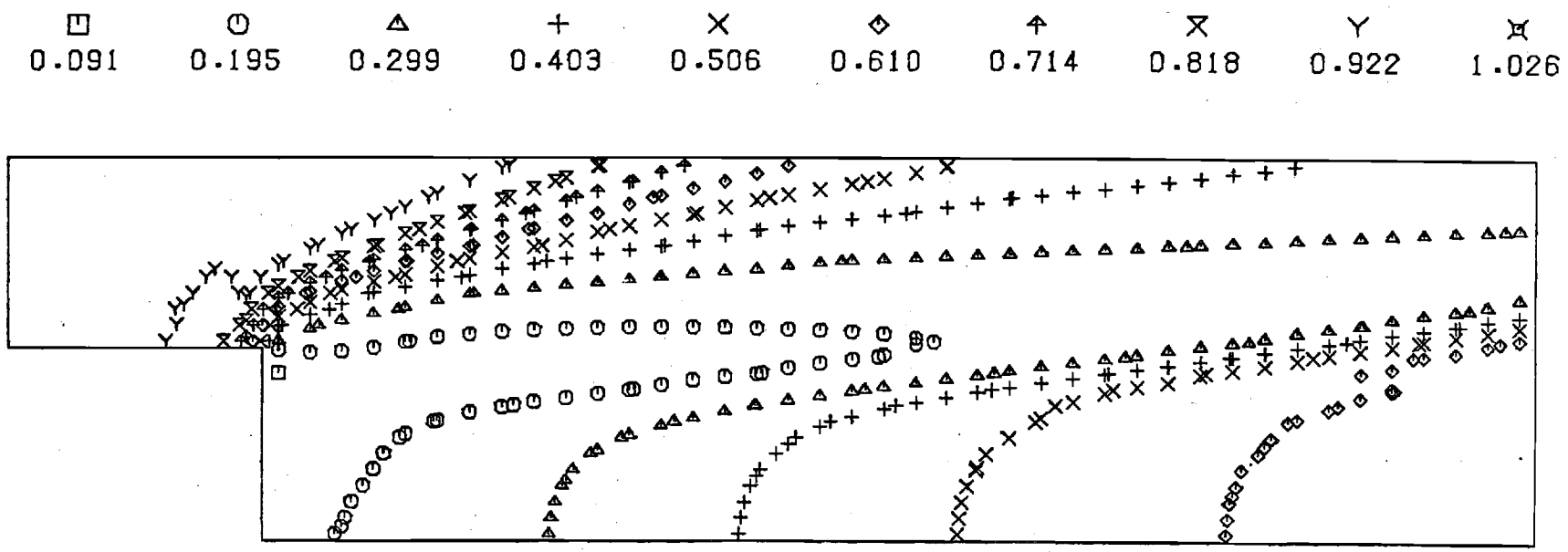

Figure 9. Pressure contours. Laminar flow.

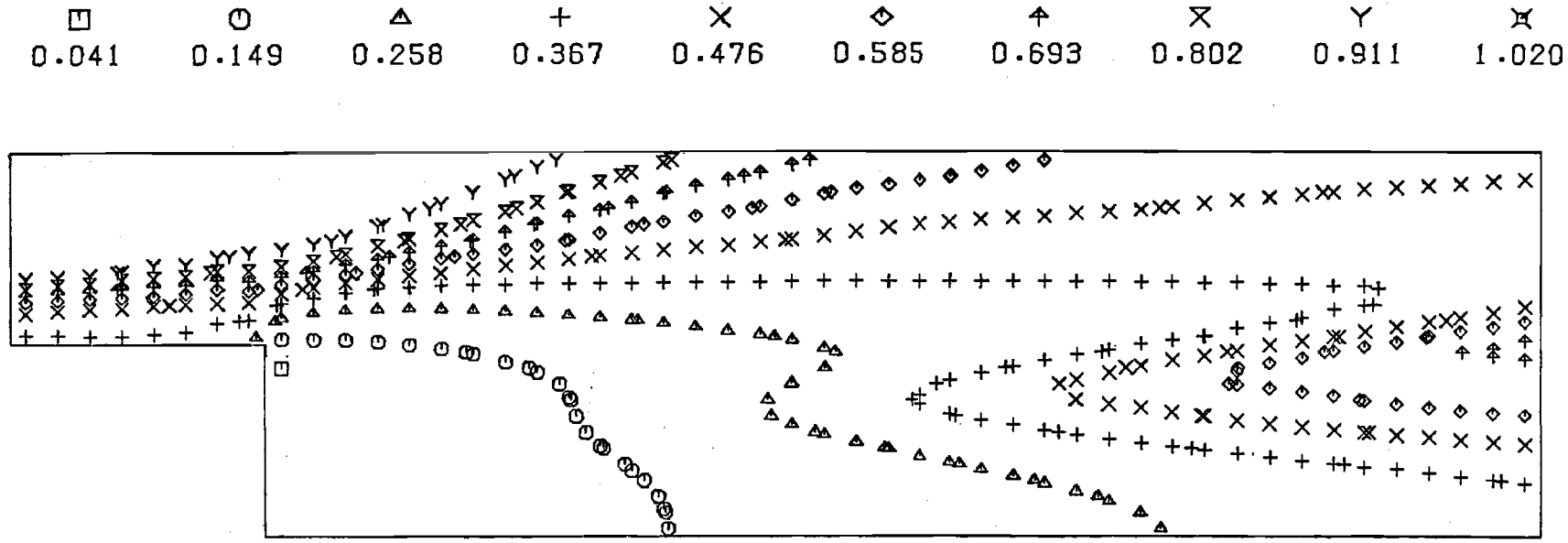

Figure 10. Density contours. Laminar flow.

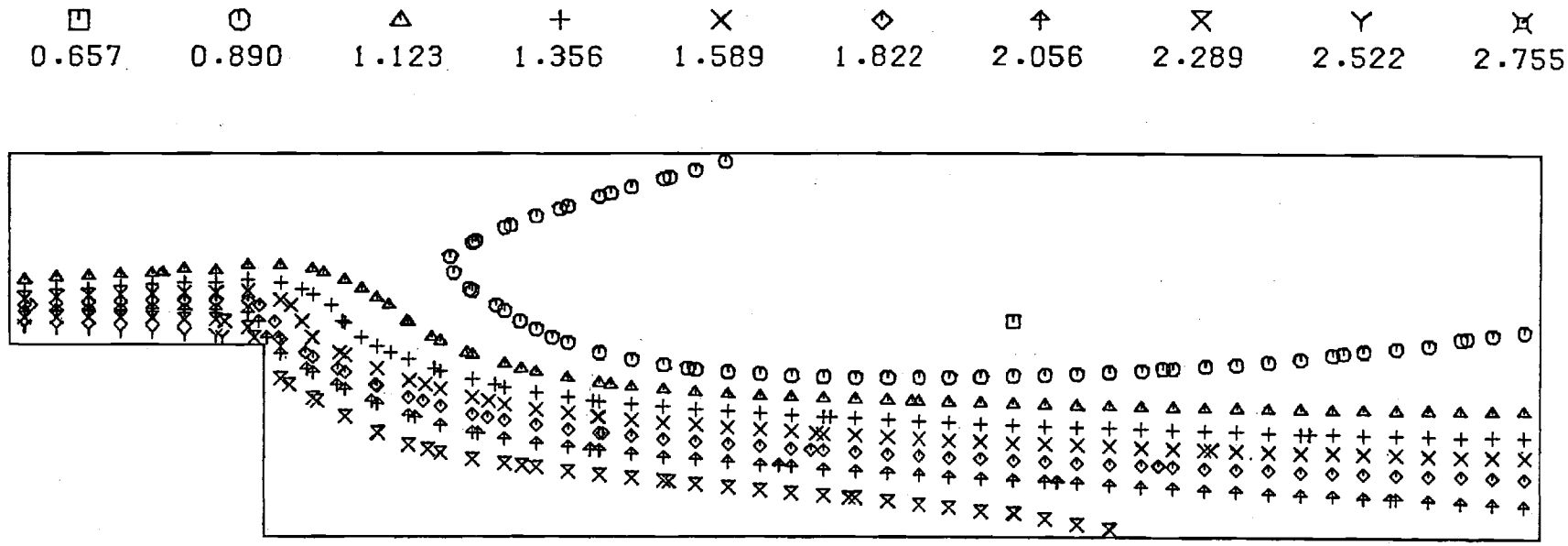

Figure 11. Internal energy contours. Laminar flow.

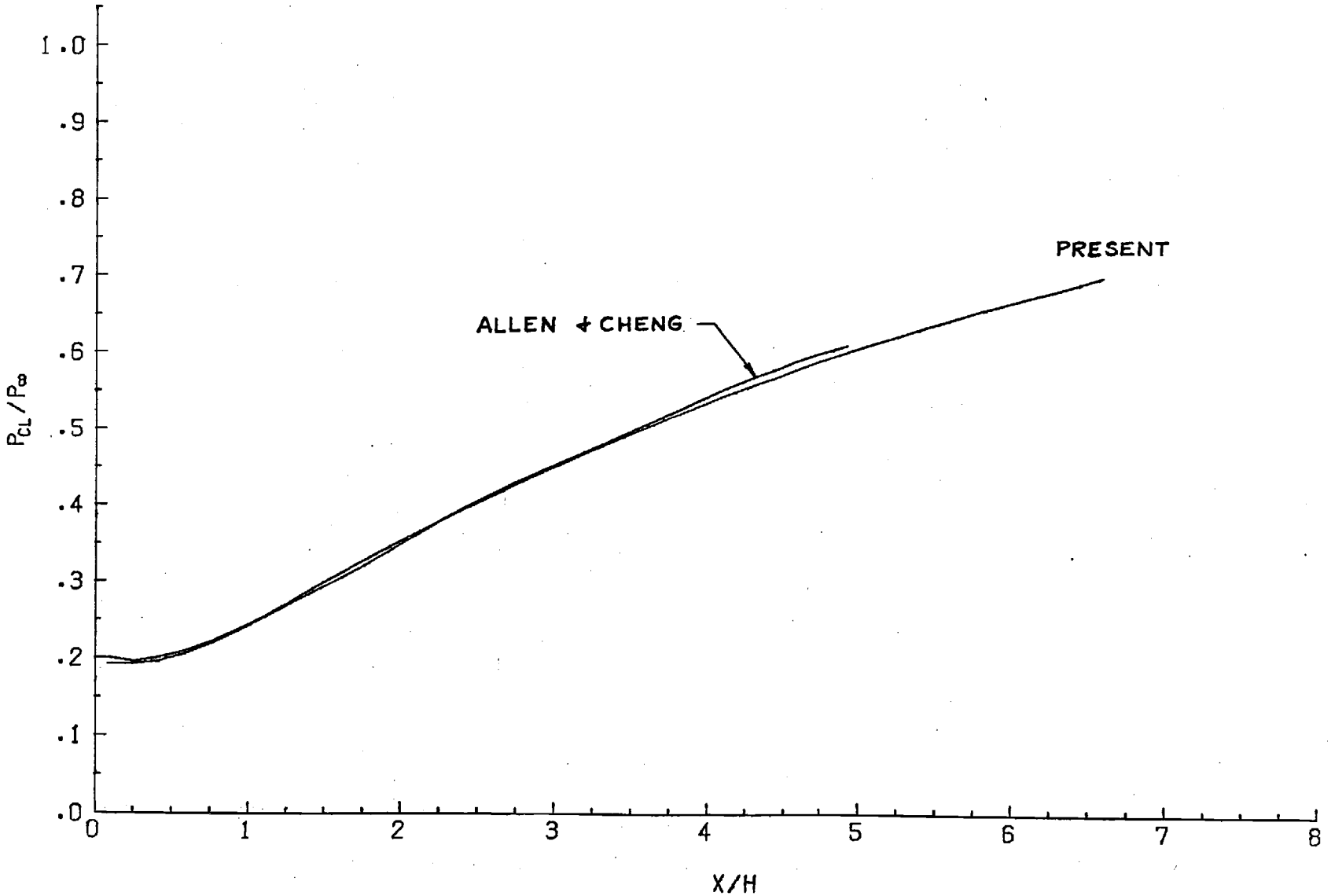

Figure 12. Centerline pressure distribution. Laminar flow.

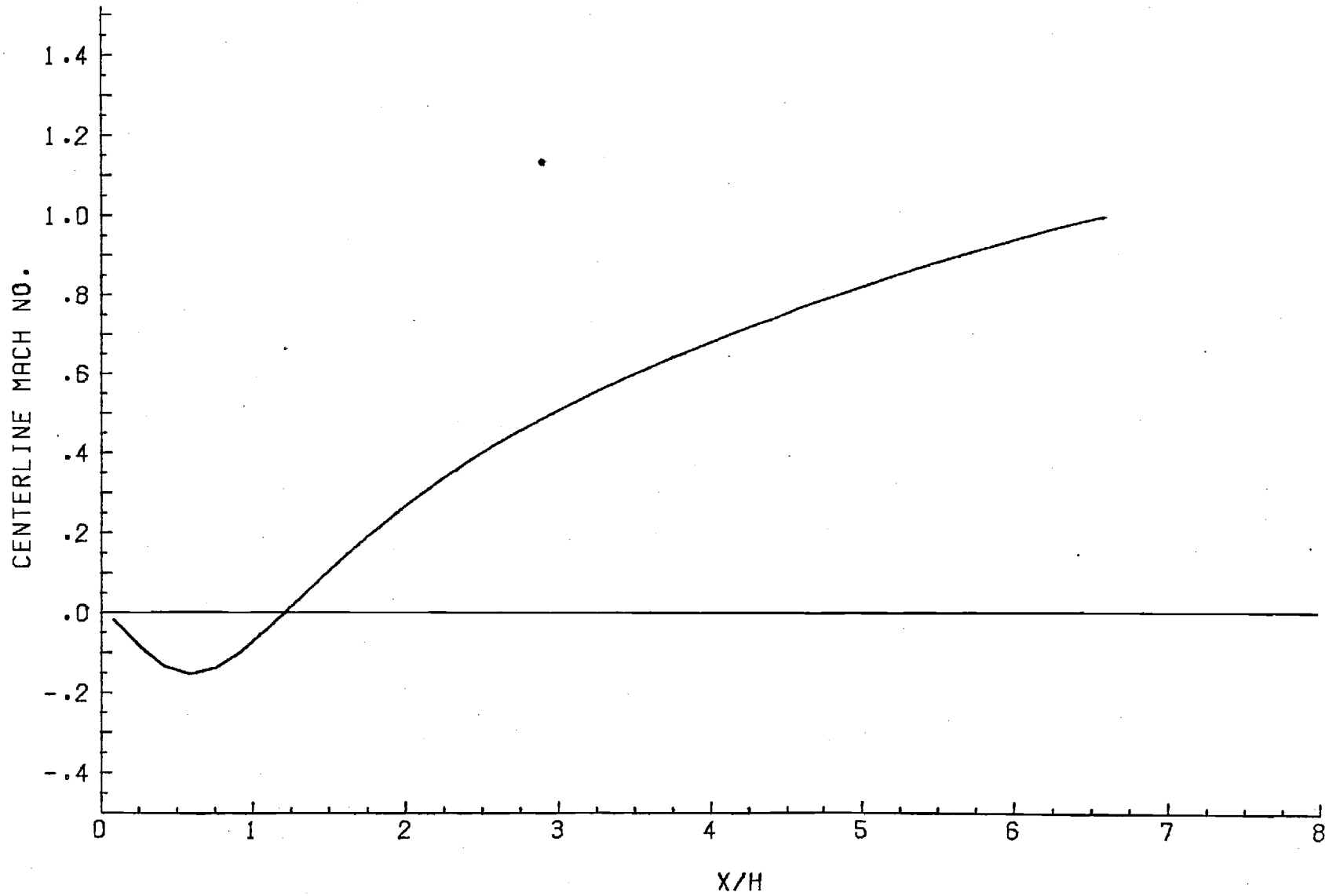

Figure 13. Centerline Mach number distribution. Laminar flow.

distance away from the centerline at the outflow boundary, the flow is already supersonic. It is perhaps worth noting that there is no singularity encountered, such as the Crocco-Lees singularity, associated with the Mach one condition.

Information concerning the convergence and the computation time of the present method is given in Figure 14. To evaluate the degree of convergence of the solution, the fractional change in each variable between successive time steps is evaluated at each grid point. The maximum fractional change for each variable and its location are then printed for each time step. Experience with the present method indicates that the density variation is a sensitive measure of convergence. Of course, by examining the changes in all the variables, as is being done, larger variations in some other variable can be easily detected. Figure 14 shows the fractional change in density plotted against number of time steps and against total computation time. Up to step 110, the maximum density change shown occurred on the centerline at the downstream boundary. Starting with step 111, the maximum change occurred on the back wall at about 0.6 H from the centerline. The maximum change remained close to the back wall for the rest of the computation. At step 450 the computation was stopped when the maximum fractional change in density had fallen to 0.0001.

The computational time step was four times the CFL time step. This value was chosen arbitrarily, as being significantly larger than the explicit stability limit, yet not so large as to cause excessive problems related to the choice of initial conditions. Briley and McDonald[9,10] used much larger time steps, but confined their attention to a much simpler flow. It is believed that the present resultsprovide a significant demonstration of the basic stability and convergence of the method. Other tests, including the

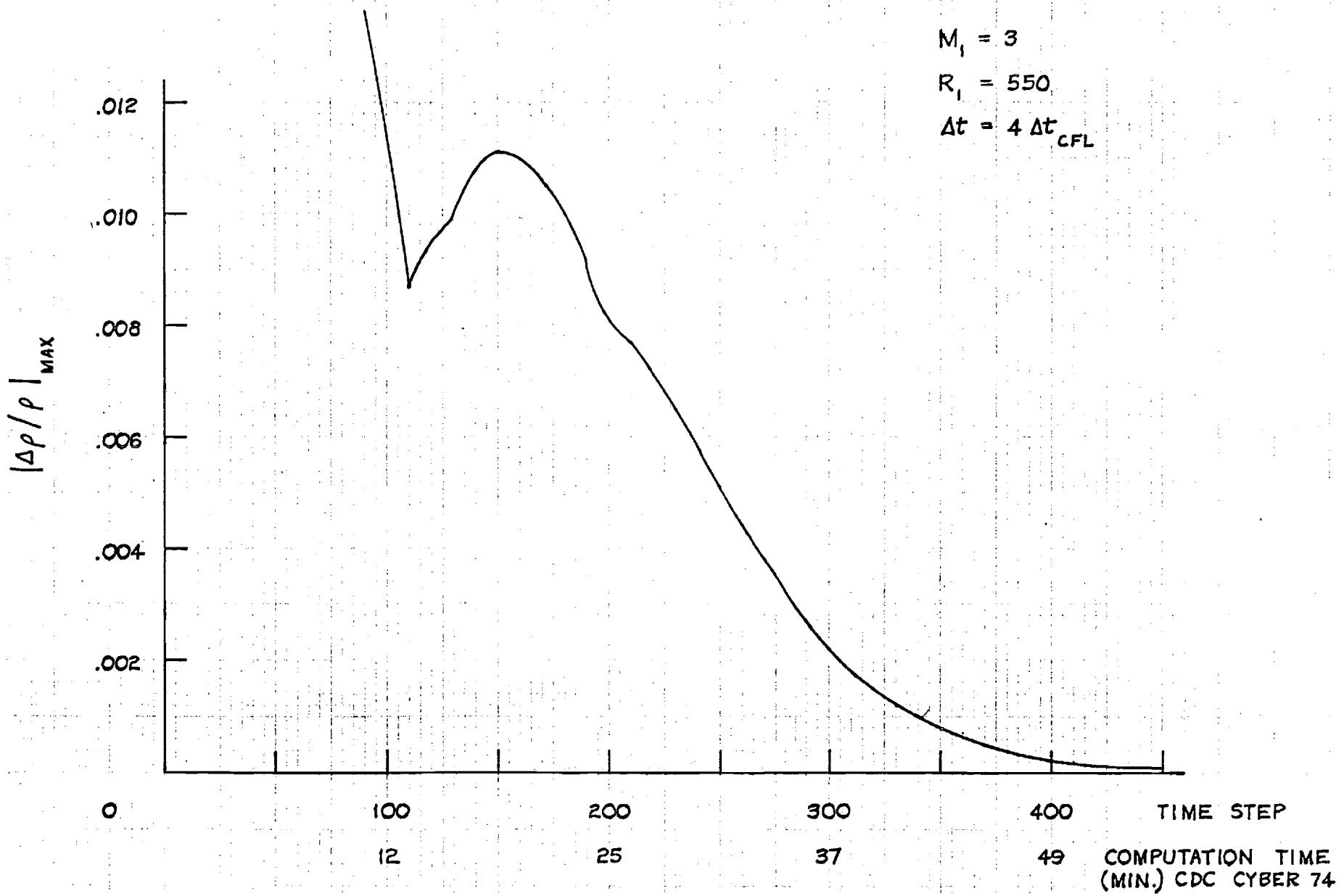

Figure 14. Variation of maximum fractional change in density. Laminar flow.

use of widely varying initial conditions and different time step sizes, must be performed in order to develop a more complete picture of the behavior of the method. This work is still being performed. The present computations had initial ρ and e equal to freestream values everywhere except in the inflow boundary layer. For $y > H$, $u = 1$ (freestream velocity) except in the inflow boundary layer, and for $y < H$, $u = 0.3$. Finally, $v = 0$ everywhere initially, except in the inflow boundary layer.

The net mass flux through the field of computation was also monitored in these calculations. In the steady state, the net mass flux should be zero. At time step 450, where the calculations were halted, the total inflow differed from the total outflow by 1.8%.

It seems significant that while conditions near the expansion corner converged most slowly, the remainder of the flow was almost unchanged after about time step 100. In a complex flow such as this, with a number of different length scales and velocity scales, different parts of the flow will converge to the steady state at different rates. Thus, it may be possible to shorten the calculation in cases where the most slowly converging portion is not of primary interest.

The potential advantages in computation time of using even larger time steps have not yet been explored. This is now being done, as reduced computation time is probably the most attractive feature of the present numerical method. In this connection, the second abscissa of Figure 14 is of interest. Here the computation (CPU) time is indicated. For laminar flow, the method takes about 7 milliseconds per grid point per time step on a CDC-CYBER 74 machine. The present grid has 1056 points. These computation times seem promising, especially if significantly larger time steps can be taken.

A calculation of a supersonic, two-dimensional, turbulent base flow

was made at the conditions of the experiments of Lewis and Chapkis.[12] These were $M_1 = 4.0$, $R_1 = 162{,}000$, and $\delta = 0.31$. The initial u-profile in the boundary layer at AB was a power-law profile with exponent 1/3.7. v was zero. e was given by the Busemann integral for an adiabatic wall.[5] The pressure was uniform and equal to the freestream value. As before, $\Delta x = 1/6$ and $\Delta y = 1/12$. The time step was again four times the CFL value. In this case, however, the k and ϵ equations were solved to give $\mu_T = C_\mu \rho k^2/\epsilon$.

In the experiments[12], the expansion corner was preceeded by a 6^o half-angle wedge. This precompression was omitted from the present calculations for simplicity, so that the inflow would be parallel to x. Thus, the 2% loss in stagnation pressure across the bow shock was not simulated.

Figure 15 shows the field of mean velocity vectors for this turbulent flow case. All the qualitative features of the flow are present, including the initial boundary layer, the turning by the corner expansion, the turning by the recompression shock, the recirculation near the base, and the retarded viscous wake. The streamlines are shown in Figure 16. Again the flow turning because of expansion, recompression, and recirculation is evident. The streamline spacing increases during expansion and decreases during compression. The extent of the recirculation region is too small, however, compared with the experimental data. Also, the dividing streamline is not clearly shown. This may be partly due to the pressure wiggles that appear in Figures 17 and 22.

Figures 17, 18, and 19 show the contours of pressure, density, and internal energy, respectively. These all show the correct qualitative behavior, in that the expansion, recompression shock, and recirculation are clearly shown. Figures 20 and 21 show the k and ϵ contours, respectively. The numerical values on the figures are one hundred times the

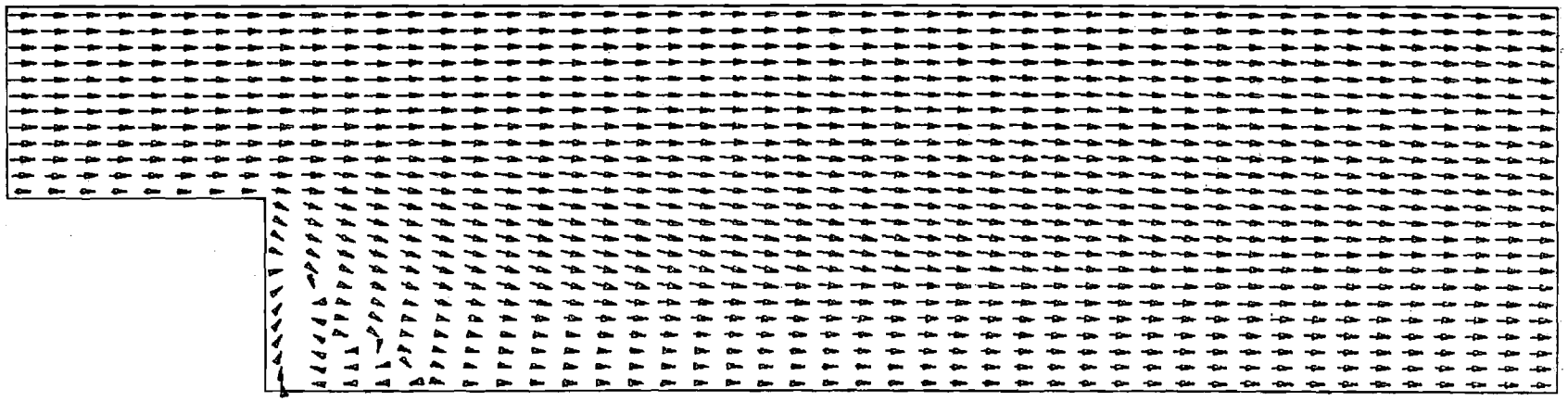

Figure 15. Velocity vectors. Turbulent flow.

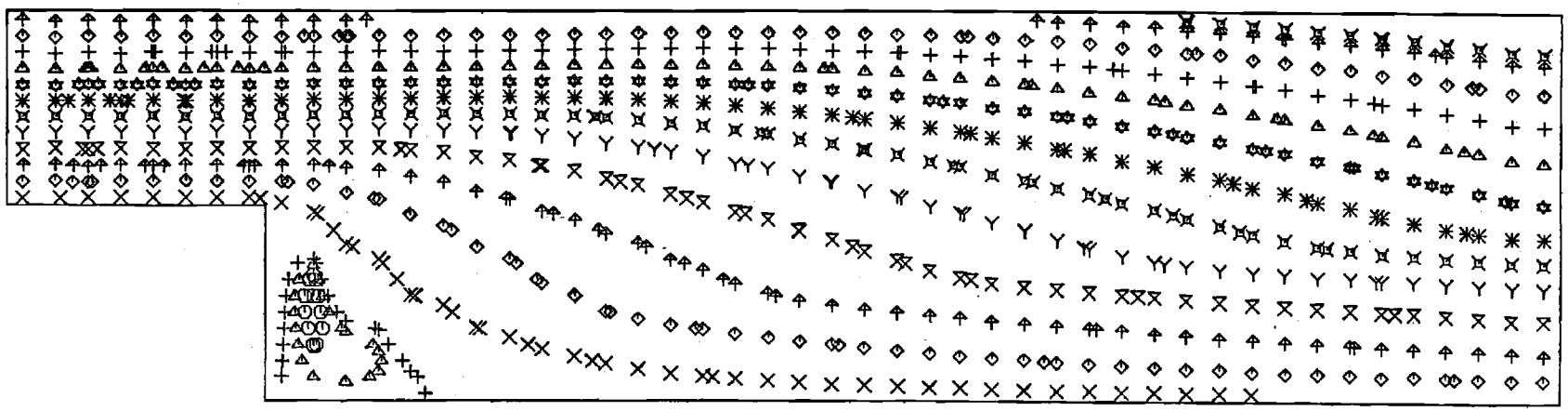

Figure 16. Streamlines. Turbulent flow.

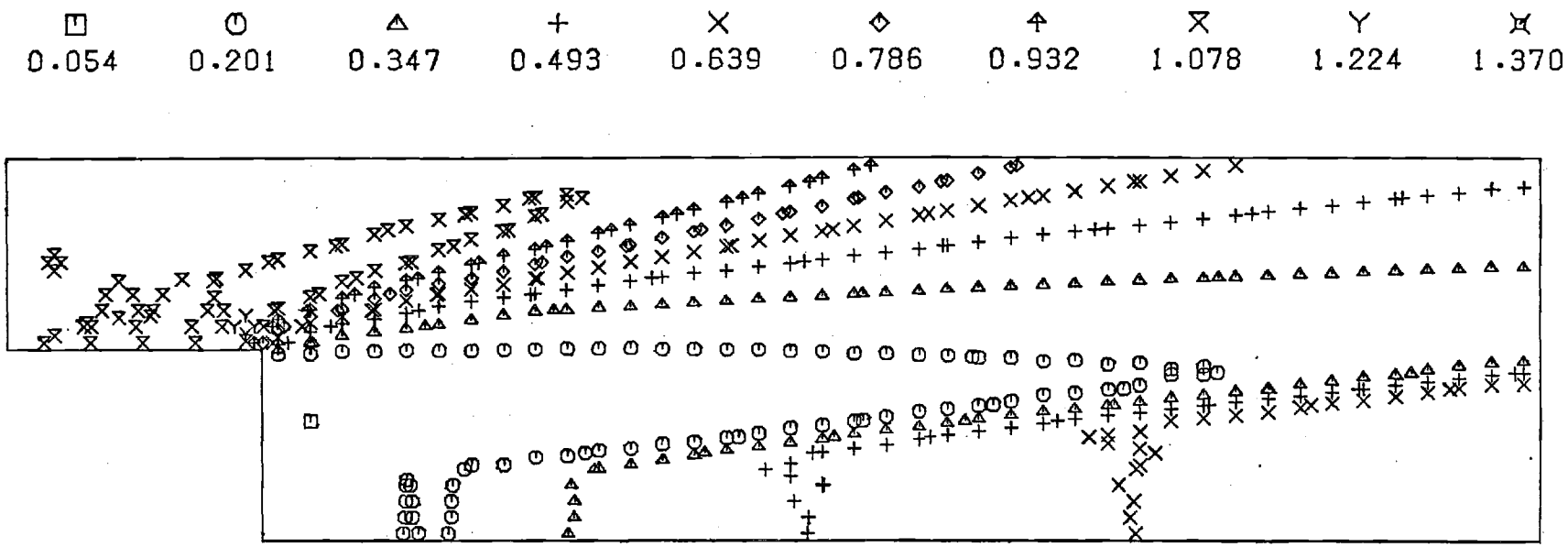

Figure 17. Pressure contours. Turbulent flow.

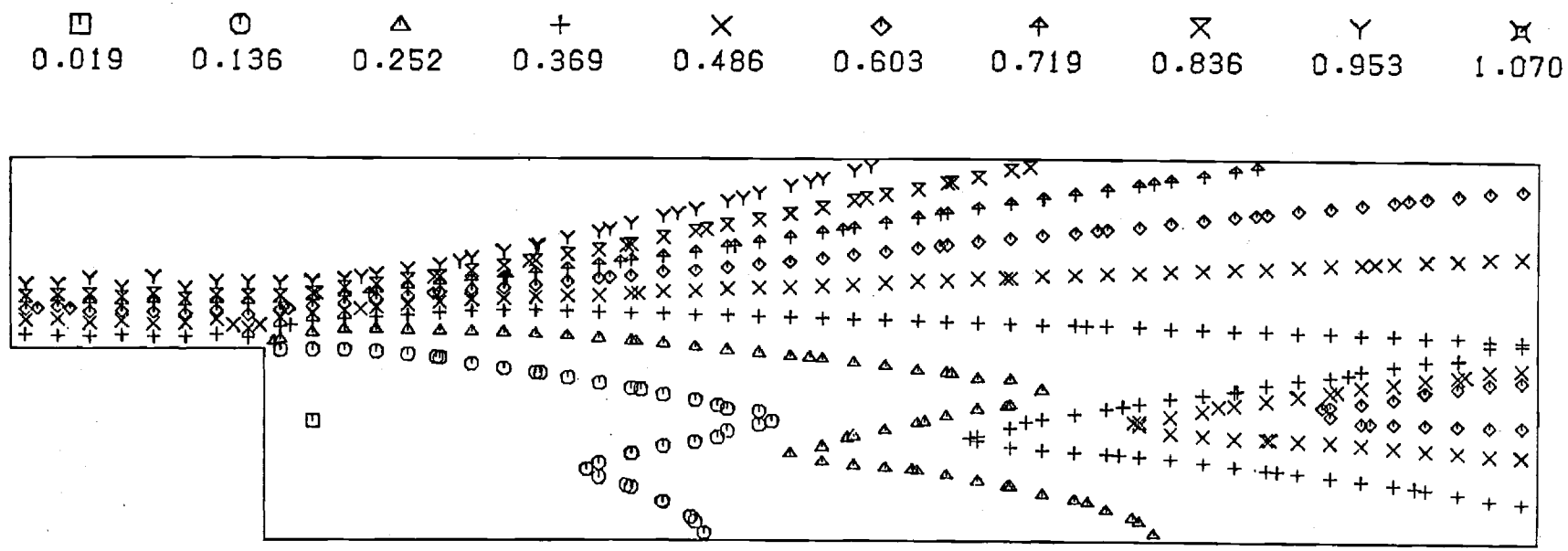

Figure 18. Density contours. Turbulent flow.

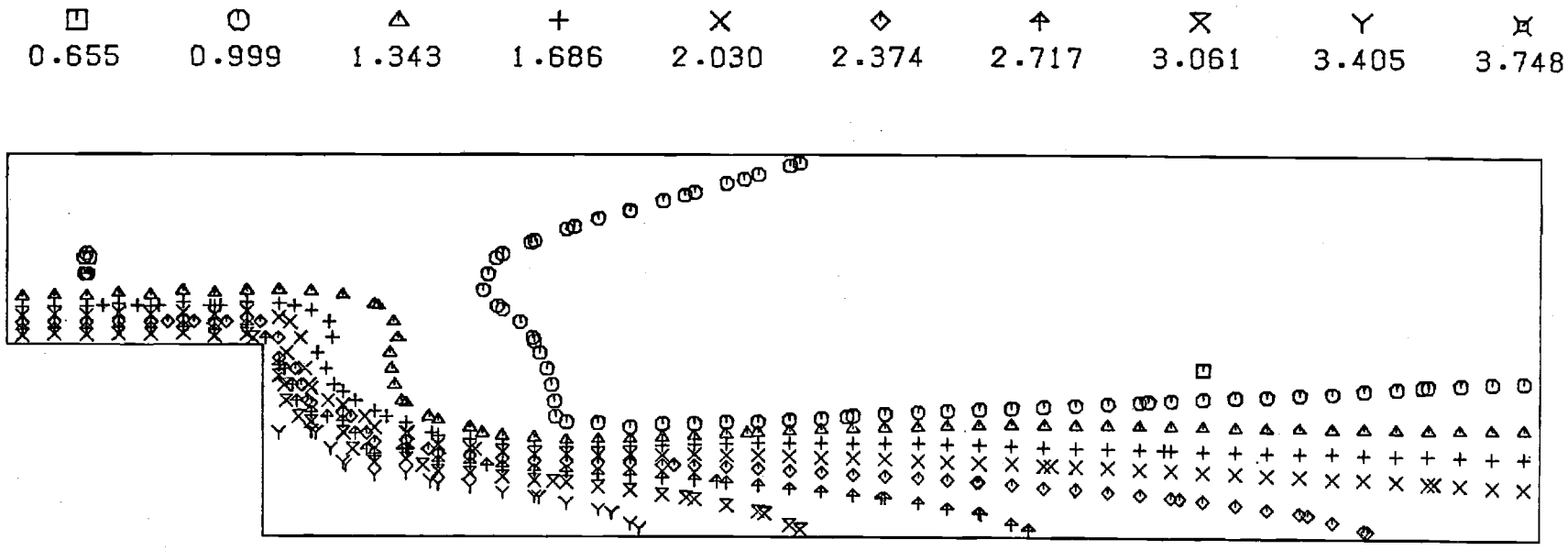

Figure 19. Internal energy contours. Turbulent flow.

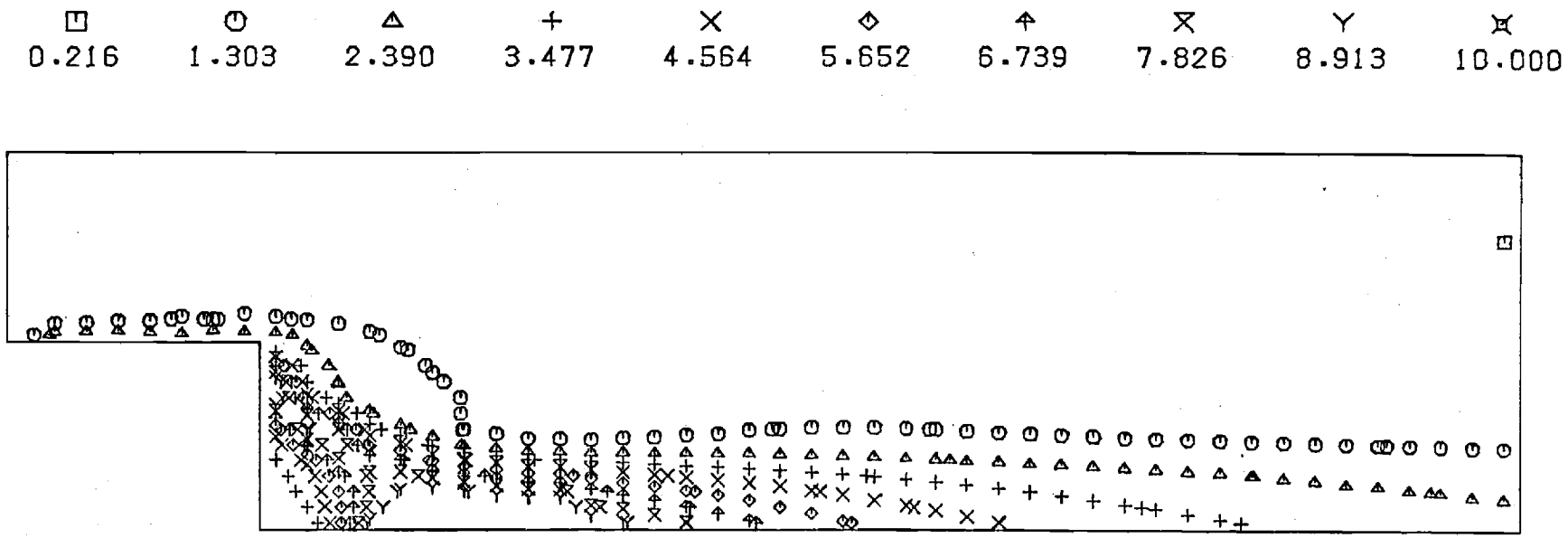

Figure 20. Turbulence kinetic energy contours.

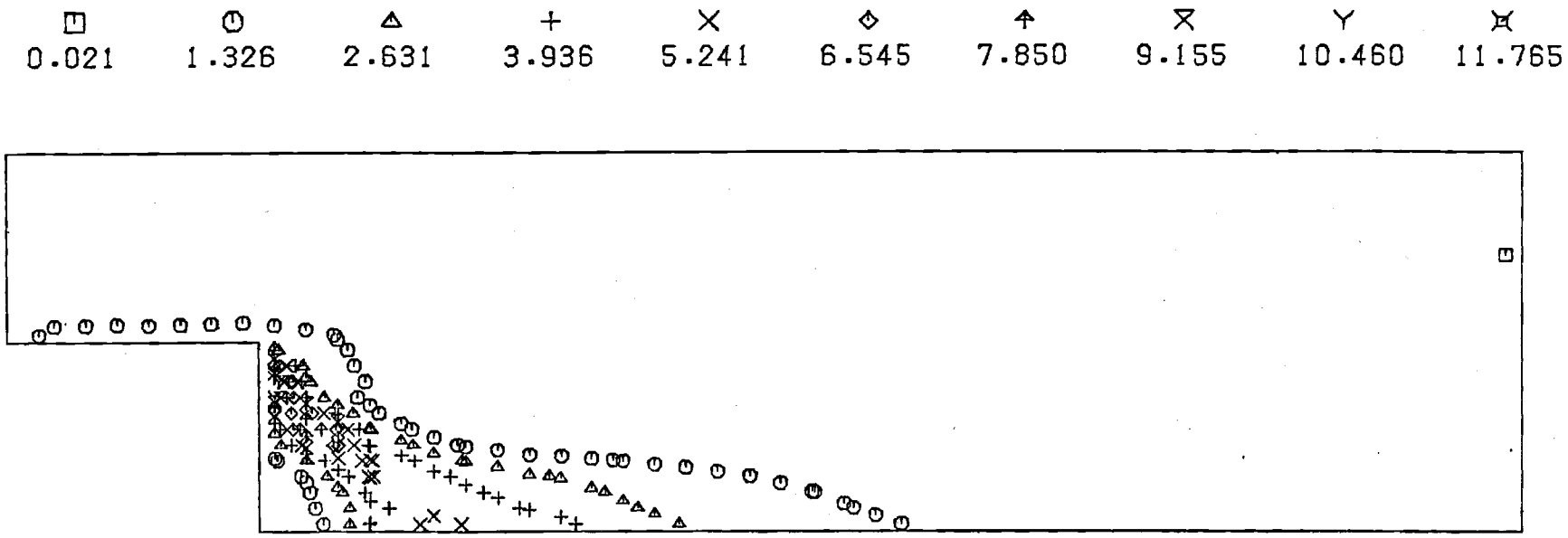

Figure 21. Turbulence dissipation rate contours.

computed values. k and ϵ take on their largest values where the shear stresses are largest.

The centerline pressure distribution is shown in Figure 22, along with the data of Lewis and Chapkis.[12] The calculation is fairly consistent with the experimental data, except that it does not show the sharp rise in pressure near $x/H = 2$. This result, plus the smaller computed recirculation region, may be caused by the turbulence model. The effect of the turbulence model on mean flow properties such as these would seem to be a useful area for further research.

Figure 23 shows the corresponding Mach number distribution.

Figure 24 is a plot of $|\Delta\rho/\rho|_{max}$ versus time step, showing the approach of the solution to convergence. The flow field was virtually unchanged after step 150. Between steps 156 and 254, $|\Delta\rho/\rho|_{max}$ occurred close to the back wall, about halfway up. From steps 255 to 300, the location shifted among four places in or near the recirculation region. The calculation was stopped at step 300 where $|\Delta\rho/\rho|_{max} = 0.0002$. Also, at this step the net mass inflow differed from the net mass outflow by 2.3%.

Careful examination of the calculations makes it clear that the pressure wiggles originate at the outflow boundary near the recompression shock. Similar behavior was previously encountered with the laminar flow calculations, when the condition $\partial\phi/\partial x = 0$ was imposed along EF. This condition, when combined with either a linear or a quadratic variation of $\phi(x)$, produced wiggles that had their largest amplitude near the back wall. Use of equation (3-35) eliminated the wiggles for the laminar flow case. Further study of the outflow boundary condition is needed, in particular to determine whether the turbulence model has any effect on the appearance of wiggles.

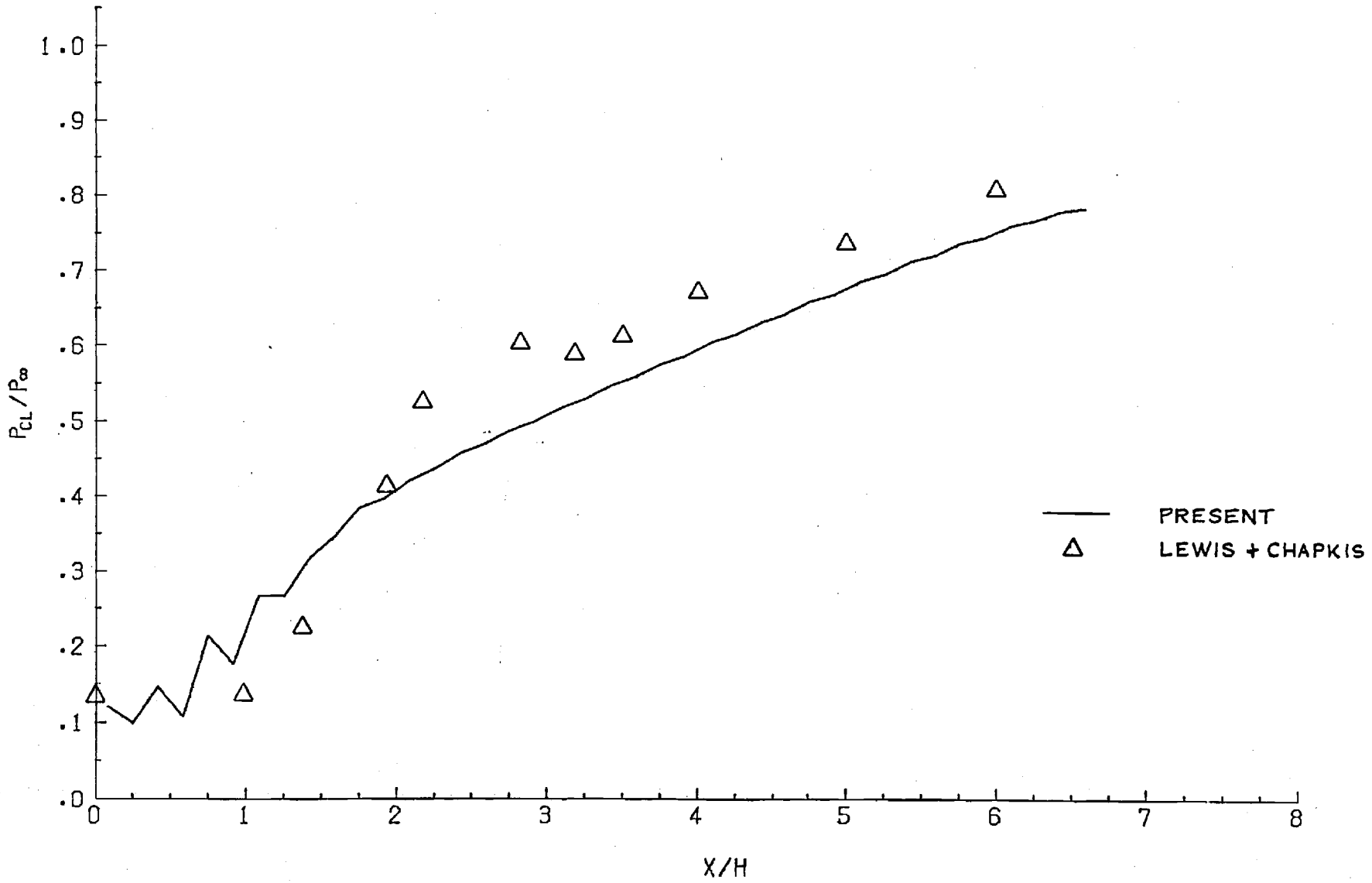

Figure 22. Centerline pressure distribution. Turbulent flow.

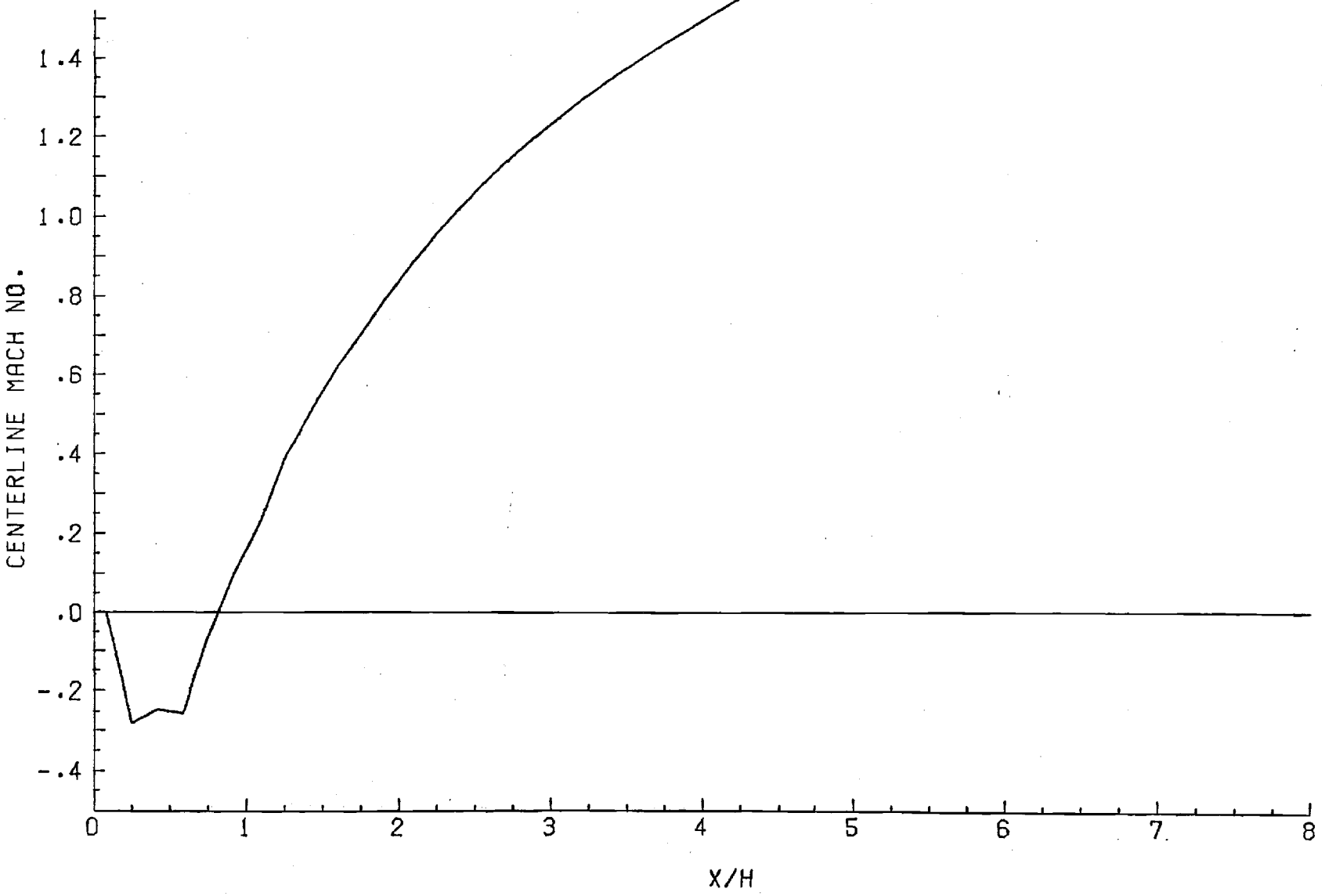

Figure 23. Centerline Mach number distribution. Turbulent flow.

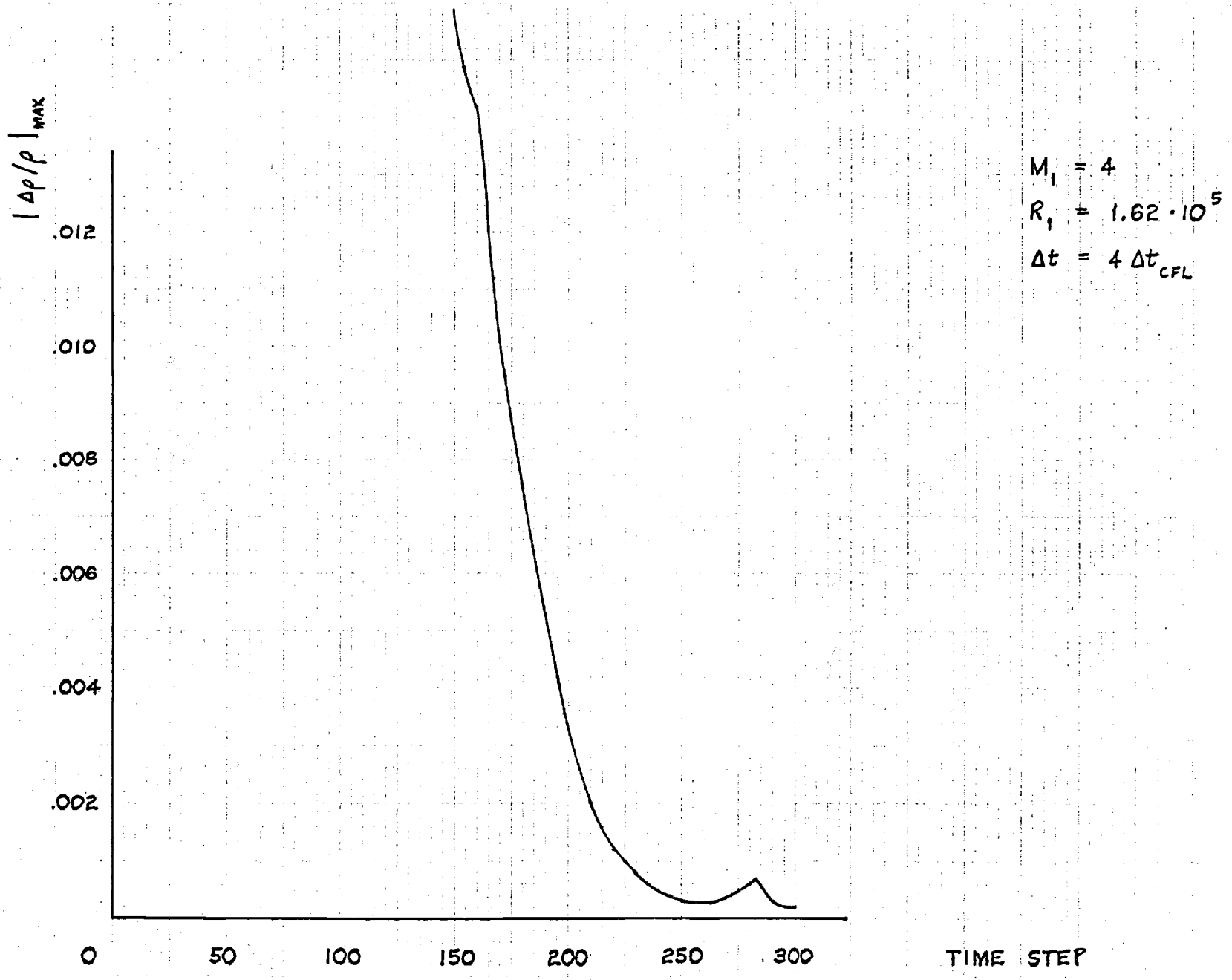

Figure 24. Variation of maximum fractional change in density. Turbulent flow.

Earlier turbulent flow calculations were made at the experimental conditions of Badrinarayanan.[6] These were $M_1 = 2.07$, $R_1 = 129{,}000$, and $\delta = 0.55$. The calculated results showed a much larger rise in pressure in the down-stream direction than did the experimental data. Because of the value of M_1 and the grid dimensions, the recompression shock passed through the upper boundary AF near F, instead of through EF as in the preceding cases. After studying the results, it became apparent that the higher pressures were associated with the simple-wave boundary conditions along AF. The left-running compression waves near the shock intersected near AF, in violation of the simple-wave condition. Numerical compression waves were reflected toward the centerline, producing an artificial pressure rise. A possible solution for this is to move AF upward, so that the shock exits through EF. The obvious disadvantage is that more grid points would be required. Alternate boundary conditions are also being considered.

5.0 CONCLUSIONS

(1) The present numerical method computed all of the main features of the supersonic base flows examined, for both the laminar and turbulent cases. These included the corner expansion, the recompression shock, the recirculation region near the base, and the viscous wake near the centerline.

(2) The flow calculations provided a demonstration of the basic stability and convergence of the numerical method.

(3) The numerical results suggest that significant savings in computer time can be achieved, compared with explicit methods, by taking large time steps.

(4) Further study is required to evaluate the effect of the particular two-equation turbulence model being used on the accuracy of the solution. In this connection other turbulence models should also be evaluated.

6.0 REFERENCES

1. Bangert, L. H., "Study of Effects of Injector Geometry on Fuel-Air Mixing and Combustion", Progress Report, NASA Grant NGR 11-002-177, Georgia Institute of Technology, August 1974.

2. Bangert, L. H. and Sebacher, D. I., "Some Effects of Combustion on Turbulent Mixing", AIAA Journal, Vol. 14, March 1976, pp. 394-396.

3. Bangert, L. H. and Roach, R. L., "Study of Effects of Injector Geometry on Fuel-Air Mixing and Combustion", NASA CR-146774, Georgia Institute of Technology, March 1976.

4. Bangert, L. H., "An Estimate of Mean Flow Properties in a Turbulent Diffusion Flame", AIAA Journal, Vol. 15, July 1977., pp. 1049-1051.

5. Allen, J. S. and Cheng, S. I., "Numerical Solutions of the Compressible Navier-Stokes Equations for the Laminar Near Wake," Physics of Fluids, Vol. 13, January 1970, pp. 37-52.

6. Badrinarayanan, M. A., "An Experimental Investigation of Base Flows at Supersonic Speeds", Journal of the Royal Aeronautical Society, Vol. 65, July 1961, pp. 475-482.

7. Roache, P. J., Computational Fluid Dynamics, Hermosa Publishers, Albuquerque, New Mexico, 1972.

8. Launder, B. E. and Spalding, D. B., "The Numerical Computation of Turbulent

Flows", Computer Methods in Applied Mechanics and Engineering, Vol. 3, 1974, pp. 269-289.

9. Briley, W. R. and McDonald, H., "An Implicit Numerical Method for the Multidimensional Compressible Navier-Stokes Equations", United Aircraft Research Laboratories, East Hartford, Connecticut, Report M911363-6, November 1973.

10. Briley, W. R., McDonald, H., and Gibeling, H. J., "Solution of the Multidimensional Compressible Navier-Stokes Equations by a Generalized Implicit Method", United Technologies Research Center, East Hartford, Connecticut, Report R75-911363-15, January 1976.

11. Isaacson, E. and Keller, H. B., Analysis of Numerical Methods, Wiley, New York, N.Y., 1966.

12. Lewis, J. E. and Chapkis, R. L., "Mean Properties of the Turbulent Near Wake of a Slender Body with and without Base Injection", AIAA Journal, Vol. 7, May 1969, pp. 835-841.

LIST OF SYMBOLS

A	empirical coefficient in reaction-rate eq. (A20), approximately 12 for the H_2 - O_2 reaction
C_a	mean mass fraction of specie a
C_f	mean mass fraction of fuel
C_N	mean mass fraction of N_2
C_o	mean mass fraction of O_2
C_p	mean mass fraction of reaction product
C_μ	empirical coefficient in eq. (A9), approximately 0.09
C_Φ	mean mass fraction of reaction invariant
$C_{\epsilon 1}$, $C_{\epsilon 2}$	empirical coefficients in ϵ eq. (A16), approximately 1.44 and 1.92, respectively
D_a	molecular diffusion coefficient of specie a
e	mean internal energy per unit mass, made nondimensional by e_1
h_R	heat of reaction per unit mass of fuel, made nondimensional by e_1
H	half-height of base
k	mean turbulent kinetic energy per unit mass, made nondimensional by u_1^2
K	$\gamma(\gamma-1)M_1^2$

M_1 Mach number, $u_1 / \left[\gamma(\gamma-1)e_1\right]^{0.5}$

p mean static pressure, made nondimensional by p_1

Pr Prandtl number

q_i $-\partial e/\partial x_i$

R_1 Reynolds number, $\rho_1 u_1 H/\mu_1$

s_{ij} see eq. (A7)

t time, made nondimensional by H/u_1

u, v mean velocity in x- and y-directions, respectively, made nondimensional by u_1

u_i mean velocity vector, made nondimensional by u_1

u_* friction velocity, made nondimensional by u_1

$\dot{w}_a$ mean reaction rate of specie a, made nondimensional by u_1/H

x,y,z Cartesian coordinates, made nondimensional by H

x_i x,y,z for i = 1,2,3, respectively

x+ , x- right and left edges, respectively, of cell containing grid point ij

y+ , y- upper and lower edges, respectively, of cell containing grid point ij

Greek

γ ratio of specific heats

δ_{ij} Kronecker delta

δ_x $(\delta_x \phi)_{ij} = (\phi_{i+1,j} - \phi_{i-1,j})/2\Delta x = (\phi_{x+} - \phi_{x-})/\Delta x$

δ_y $(\delta_y \phi)_{ij} = (\phi_{i,j+1} - \phi_{i,j-1})/2\Delta y = (\phi_{y+} - \phi_{y-})/\Delta y$

Δt computational time step, made nondimensional by H/u_1

Δx, Δy, Δz dimensions of cell containing grid point ij, made nondimensional by H

ϵ dissipation rate of turbulent kinetic energy per unit mass, made nondimensional by u_1^3/H

K von Karman constant, approximately 0.43

μ molecular viscosity, made nondimensional by μ_1

μ_T eddy viscosity, made nondimensional by $\rho_1 u_1 H$

ρ mean density, made nondimensional by ρ_1

σ_c turbulent Schmidt number, approximately 0.7

σ_h turbulent Prandtl number, approximately 0.7

σ_k empirical coefficient in k-eq., approximately 1.0

σ_ϵ empirical coefficient in ϵ- eq., approximately 1.3

ϕ any dependent variable

Subscript

1	denotes free stream conditions

Superscripts

n	known time level
n+1	unknown time level
*	intermediate time level after x-sweep
**	time level after y-sweep, taken to be the same as (n+1)

APPENDIX A. Finite Difference Forms of the Conservation Equations

Conservation of Mass

The differential equation for conservation of mass is, using Cartesian tensor notation:

$$\partial\rho/\partial t + \partial\rho u_i/\partial x_i = 0 \tag{A1}$$

This equation is then integrated over a control volume (CV) which is a cell of dimensions Δx, Δy, Δz. Thus,

$$\iiint_{CV} (\partial\rho/\partial t)\, dV = -\iiint_{CV} (\partial\rho u_i/\partial x_i)\, dV$$

$$= -\iint_{CS} \rho u_i n_i dA \tag{A2}$$

using Gauss' theorem. For two-dimensional flow, the area integral over the control surface (CS) becomes:

$$\iint_{CS} \rho u_i n_i dA = \iint_{x+} \rho u\, dy\, dz + \iint_{x-} \rho u(-1)\, dydz$$

$$+ \iint_{y+} \rho v\, dx\, dz + \iint_{y-} \rho v(-1)\, dxdz \tag{A3}$$

Next, the following approximations are made:

$$\iiint_{CV} (\partial\rho/\partial t)dV \cong (\partial\rho/\partial t)_{ij} .\Delta x.\Delta y.\Delta z$$

$$\iint_{x+} \rho u\, dy\, dz \cong (\rho u)_{x+} .\Delta y.\Delta z \tag{A4}$$

etc.

Equation (A2) then becomes:

$$(\partial\rho/\partial t)_{ij} = -(1/\Delta x)\left[(\rho u)_{x+} - (\rho u)_{x-}\right] - (1/\Delta y)\left[(\rho v)_{y+} - (\rho v)_{y-}\right] \quad \text{(A5a)}$$

or

$$\partial\rho/\partial t = -\delta_x(\rho u) - \delta_y(\rho v) \quad \text{(A5b)}$$

Conservation of Momentum:

The differential equation is:

$$\partial(\rho u_i)/\partial t = -(\partial/\partial x_j)\left\{\rho u_i u_j + (1/\gamma M_1^2)\rho e\,\delta_{ij} - (\mu_T + \mu/R_1)s_{ij} + (2/3)\rho k\,\delta_{ij}\right\} \quad \text{(A6)}$$

Here,

$$s_{ij} = \partial u_i/\partial x_j + \partial u_j/\partial x_i - (2/3)\delta_{ij}\,\partial u_m/\partial x_m \quad \text{(A7)}$$

and the Reynolds stress tensor is modeled by:

$$\tau_{T,ij} = \mu_T\, s_{ij} - (2/3)\,\rho k\,\delta_{ij} \quad \text{(A8)}$$

where

$$\mu_T = C_\mu\,\rho k^2/\epsilon \quad \text{(A9)}$$

Equation (A6) is next integrated over the control volume that is the cell surrounding grid point (ij). After applying Guass' theorem and making approximations like those in eqs. (A4), the resulting equations for x- and y-momentum are:

x-momentum:

$$\partial\rho u/\partial t = -\delta_x \left\{\rho u^2 + \rho e/\gamma M_1^2 - (\mu_T + \mu/R_1)s_{xx} + (2/3)\rho k\right\}$$

$$- \delta_y \left\{\rho uv - (\mu_T + \mu/R_1)\, s_{xy}\right\} \qquad \text{(A10)}$$

y-momentum:

$$\partial\rho v/\partial t = -\delta_x \left\{\rho uv - (\mu_T + \mu/R_1)\, s_{xy}\right\}$$

$$- \delta_y \left\{\rho v^2 + \rho e/\gamma M_1^2 - (\mu_T + \mu/R_1)\, s_{yy} + (2/3)\,\rho k\right\} \qquad \text{(A11)}$$

From eq. (A7),

$$s_{xx} = (4/3)\,\partial u/\partial x - (2/3)\,\partial v/\partial y$$

$$s_{xy} = \partial u/\partial y + \partial v/\partial x$$

$$s_{yy} = (4/3)\,\partial v/\partial y - (2/3)\,\partial u/\partial x$$

Conservation of Energy

The differential equation is:

$$(\partial/\partial t)\left[\rho e + \rho\, C_f\, h_R + (K/2)\,\rho u_i u_i\right]$$

$$= -(\partial/\partial x_j)\left\{\rho u_j\left[\gamma e + C_f\, h_R + (K/2)\, u_i u_i\right] + \left(\mu_T/\sigma_h + \mu/Pr.R_1\right)\gamma\, q_j\right.$$

$$\left. - K(\mu_T + \mu/R_1)\, s_{ij}\, u_i + (2/3)K\,\rho\, k\, u_j\right\}$$

$$+ K\rho\varepsilon - K\mu_T\, s_{ij}\,\partial u_i/\partial x_j + (2/3)\,K\rho k\,\partial u_i/\partial x_i \qquad \text{(A12)}$$

Equation (A12) can be put into finite-difference form by following the same sequence of steps used for conservation of mass and momentum. The result is as follows:

$$(\partial/\partial t)\left[\rho e + \rho C_f h_R + (K/2)\rho(u^2 + v^2)\right]$$

$$= -\delta_x \left\{\rho e\left[\gamma e + C_f h_R + (K/2)(u^2 + v^2)\right] + (\mu_T/\sigma_h + \mu/Pr.R_l)\gamma q_x\right.$$

$$\left. - K(\mu_T + \mu/R_l)\, s_{ix}\, u_i + (2/3)\, K\rho ku\right\}$$

$$-\delta_y \left\{\rho v\left[\gamma e + C_f h_R + (K/2)(u^2 + v^2)\right] + (\mu_T/\sigma_h + \mu/Pr.R_l)\gamma q_y\right.$$

$$\left. - K(\mu_T + \mu/R_l)\, s_{iy}\, u_i + (2/3)\, K\rho kv\right\}$$

$$+ K\rho\epsilon - K\mu_T\, s_{ij}\, \partial u_i/\partial x_j + (2/3)\, K\rho k\,(\partial u/\partial x + \partial v/\partial y) \qquad \text{(A13)}$$

In equation (A13), the following have been used:

$$q_x = -\partial e/\partial x$$

$$q_y = -\partial e/\partial y$$

$$s_{ix}\, u_i = \left[(4/3)\,\partial u/\partial x - (2/3)\,\partial v/\partial y\right] u + (\partial u/\partial y + \partial v/\partial x)v$$

$$s_{iy}\, u_i = \left[(4/3)\,\partial v/\partial y - (2/3)\,\partial u/\partial x\right] v + (\partial u/\partial y + \partial v/\partial x)\, u$$

$$s_{ij}\,\partial u_i/\partial x_j = (4/3)\left[(\partial u/\partial x)^2 - (\partial u/\partial x)(\partial v/\partial y) + (\partial v/\partial y)^2\right] + (\partial u/\partial y + \partial v/\partial x)^2$$

Conservation of k

The differential equation is:

$$\partial(\rho k)/\partial t = -(\partial/\partial x_j)\left[\rho u_j k - (\mu_T/\sigma_k)(\partial k/\partial x_j)\right] - \rho\epsilon + \mu_T\, s_{ij}\,\partial u_i/\partial x_j - (2/3)\rho k\,\partial u_i/\partial x_i \qquad \text{(A14)}$$

After following the sequence of steps described in the preceding, the corresponding finite-difference form is:

$$\partial(\rho k)/\partial t = -\delta_x\left[\rho uk - (\mu_T/\sigma_k)(\partial k/\partial x)\right] - \delta_y\left[\rho vk - (\mu_T/\sigma_k)(\partial k/\partial y)\right] - \rho\epsilon + \mu_T\, s_{ij}\,\partial u_i/\partial x_j - (2/3)\rho k\,(\partial u/\partial x + \partial v/\partial y) \qquad \text{(A15)}$$

Conservation of ε

The differential equation is:

$$\partial(\rho\epsilon)/\partial t = -(\partial/\partial x_j)\left[\rho u_j \epsilon - (\mu_T/\sigma_\epsilon)(\partial \epsilon/\partial x_j)\right] + C_{\epsilon 1}(\epsilon/k)\left[\mu_T\, s_{ij}\,\partial u_i/\partial x_j - (2/3)\rho k\,\partial u_i/\partial x_i\right] - C_{\epsilon 2}\,\rho\epsilon^2/k \qquad \text{(A16)}$$

The corresponding finite-difference equation is:

$$\partial(\rho\epsilon)/\partial t = -\delta_x\left[\rho u\epsilon - (\mu_T/\sigma_\epsilon)(\partial\epsilon/\partial x)\right] - \delta_y\left[\rho v\epsilon - (\mu_T/\sigma_\epsilon)(\partial\epsilon/\partial y)\right]$$

$$+ C_{\epsilon 1}(\epsilon/k)\left[\mu_T s_{ij}\,\partial u_i/\partial x_j - (2/3)\rho k(\partial u/\partial x + \partial v/\partial y)\right] + C_{\epsilon 2}\rho\epsilon^2/k \qquad \text{(A17)}$$

Conservation of Chemical Specie m

The differential equation is:

$$\partial(\rho C_m)/\partial t = -(\partial/\partial x_j)\left[\rho u_j C_m - (\mu_T/\sigma_c + \rho D_m)(\partial C_m/\partial x_j)\right] + \rho\dot{w}_m \qquad \text{(A18)}$$

The corresponding finite-difference equation is:

$$\partial(\rho C_m)/\partial t = -\delta_x\left[\rho u C_m - (\mu_T/\sigma_c + \rho D_m)(\partial C_m/\partial x)\right]$$

$$-\delta_y\left[\rho v C_m - (\mu_T/\sigma_c + \rho D_m)(\partial C_m/\partial y)\right] + \rho\dot{w}_m \qquad \text{(A19)}$$

When C_m is C_f, $\dot{w}_f$ can be represented by[4]:

$$\dot{w}_f = -A(\epsilon/k)\,C_f\,C_o \qquad \text{(A20)}$$

When C_m is C_ϕ, then $\dot{w}_f$ is zero.

C_o is then computed from:

$$C_o = C_\phi + \lambda\,C_f \qquad \text{(A21)}$$

where

$$\lambda = b\,\hat{W}_o / a\,\hat{W}_f \tag{A22}$$

and a and b are stoichiometric coefficients for the reaction:

$$a\ (\text{Fuel}) + b\ (\text{Oxygen}) \rightarrow c\ (\text{Product}) \tag{A23}$$

For example, for the $H_2 - O_2$ reaction, $\lambda = 8$.

When the oxidizing medium is air, C_N can be computed from:

$$C_N = 1.88\,\hat{W}_N \left[(1 - C_f - C_o)\,\hat{W}_o + 2\,C_o\,\hat{W}_p \right] / \hat{W}_o\,(\hat{W}_p + 1.88\,\hat{W}_N) \tag{A24}$$

Then, C_p is given by:

$$C_p = 1 - C_f - C_o - C_N \tag{A25}$$

APPENDIX B. The Form of the Conservation Equations for the Alternating Direction Implicit (ADI) Solution

Conservation of Mass

A backward time-difference approximation is applied to equation (A5), and then the right-hand side is linearized about the nth time level. The result is:

$$(\rho^{n+1} - \rho^n)/\Delta t = -\delta_x(\rho^n u^{n+1} + \rho^{n+1} u^n - \rho^n u^n) - \delta_y(\rho^n v^{n+1} + \rho^{n+1} v^n - \rho^n v^n) \tag{B1}$$

This result is also given as equation (2-5).

For the x-sweep equations, (n+1)th level quantities are evaluated at an intermediate time level, denoted by $*$, except for arguments of δ_y.

$$(\rho^* - \rho)/\Delta t = -\delta_x(\rho^* u + \rho u^* - \rho u) - \delta_y(\rho v) \tag{B2}$$

(x-sweep)

Here and in what follows, quantities without a superscript are understood to be at the nth level.

The y-sweep equation is formed from equation (B1) by evaluating (n+1)th level quantities at $**$, except for arguments of δ_x, in which (n+1) level quantities are evaluated at $*$.

$$(\rho^{**} - \rho)/\Delta t = -\delta_x(\rho^* u + \rho u^* - \rho u) - \delta_y(\rho^{**} v + \rho v^{**} - \rho v) \tag{B3}$$

The final y-sweep equation is obtained by subtracting equation (B2) from equation (B3).

$$(\rho^{**} - \rho^{*})/\Delta t = - \delta_y(\rho^{**} v + \rho v^{**} - 2\rho v) \qquad \text{(B4)}$$

(y-sweep)

Equations (B2) - (B4) also appear as equations (2-7) - (2-9), respectively.

Quantities with superscript ** are considered to be the same as the corresponding quantities at the (n+1)th level.

Conservation of x-Momentum

After time differencing and time linearization, equation (A10) becomes:

$$(\rho^{n+1} u + \rho u^{n+1} - 2\ \rho u)/\Delta t$$

$$= - \delta_x \left[\rho^{n+1} u^2 + 2\ \rho u u^{n+1} - 2\ \rho u^2 + (\rho^{n+1} e + \rho e^{n+1} - \rho e)/\gamma M_1^2 \right.$$

$$\left. - (\mu_T + \mu/R_1)\ s_{xx}^{n+1} + (2/3)(\rho^{n+1} k + \rho k^{n+1} - \rho k) \right]$$

$$- \delta_y \left[\rho^{n+1} uv + \rho u^{n+1} v + \rho u v^{n+1} - 2\rho uv - (\mu_T + \mu/R_1) s_{xy}^{n+1} \right] \qquad \text{(B5)}$$

Note that μ_T and μ are evaluated at the nth level, and thus treated explicitly rather than implicitly. The x-sweep equation is:

$$(\rho^{*} u + \rho u^{*} - 2\ \rho u)/\Delta t$$

$$= - \delta_x \left\{ \rho^{*} u^2 + 2\ \rho u u^{*} - 2\ \rho u^2 + (\rho^{*} e + \rho e^{*} - \rho e)/\gamma M_1^2 \right.$$

$$\left. - (\mu_T + \mu/R_1) \left[(4/3)\delta_x u^{*} - (2/3)\delta_y v) \right] + (2/3)(\rho^{*} k + \rho k^{*} - \rho k) \right\}$$

$$- \delta_y \left[\rho uv - (\mu_T + \mu/R_1)\ s_{xy} \right] \qquad \text{(B6)}$$

Mixed derivatives $\delta_x \delta_y$ are treated explicitly at the nth level, because they are awkward to treat implicitly. The y-sweep equation is:

$$(\rho^{**}u + \rho u^{**} - \rho^{*}u - \rho u^{*})/\Delta t$$

$$= -\delta_y \left[\rho^{**}uv + \rho u^{**}v + \rho uv^{**} - 3\rho uv - (\mu_T + \mu/R_1)\,\delta_y(u^{**} - u)\right] \qquad \text{(B7)}$$

Conservation of y-Momentum

The time-linearized difference equation is:

$$(\rho^{n+1}v + \rho v^{n+1} - 2\rho v)/\Delta t$$

$$= -\delta_x \left[\rho^{n+1}uv + \rho u^{n+1}v + \rho uv^{n+1} - 2\,\rho uv - (\mu_T + \mu/R_1)\,s_{xy}\right]$$

$$-\delta_y \left[\rho^{n+1}v^2 + 2\,\rho vv^{n+1} - 2\,\rho v^2 + (\rho^{n+1}e + \rho e^{n+1} - \rho e)/\gamma M_1^2\right.$$

$$\left. - (\mu_T + \mu/R_1)s_{yy}^{n+1} + (2/3)(\rho^{n+1}k + \rho k^{n+1} - \rho k)\right] \qquad \text{(B8)}$$

The x-sweep equation is:

$$(\rho^{*}v + \rho v^{*} - 2\ \rho v)/\Delta t$$

$$= -\ \delta_x \left[\rho^{*}uv + \rho u^{*}v + \rho uv^{*} - 2\ \rho uv - (\mu_T + \mu/R_1)(\delta_y u + \delta_x v^{*})\right]$$

$$-\ \delta \left\{\rho v^2 + \rho e/\gamma M_1^2 - (\mu_T + \mu/R_1)\left[(4/3)\delta_y v - (2/3)\delta_x u\right]\right.$$

$$\left. + (2/3)\rho k\right\} \qquad \text{(B9)}$$

The y-sweep equation is:

$$(\rho^{**}v + \rho v^{**} - \rho^{*}v - \rho v^{*})/\Delta t$$

$$= -\ \delta_y \left[\rho^{**}v^2 + 2\ \rho v v^{**} - 3\ \rho v^2 + (\rho^{**}e + \rho e^{**} - 2\ \rho e)/\gamma M_1^2\right.$$

$$\left. - (\mu_T + \mu/R_1)\ (4/3)\ \delta_y(v^{**} - v) + (2/3)(\rho^{**}\ k + \rho k^{**} - 2\ \rho k)\right]$$

(B10)

Conservation of Energy

The time-linearized difference equation is:

$$
\begin{aligned}
&(1/\Delta t)\left\{\rho^{n+1}\left[e + C_f h_R + (K/2)(u^2 + v^2)\right] + \rho(e^{n+1} + C_f{}^{n+1} h_R)\right. \\
&\left. + K\rho(uu^{n+1} + vv^{n+1}) - 2\rho(e + C_f h_R) - (3/2)K\rho(u^2 + v^2)\right\} \\
&= -\delta_x\left\{(\rho^{n+1}u + \rho u^{n+1})\left[\gamma e + C_f h_R + (K/2)(u^2 + v^2)\right]\right. \\
&\quad + \rho u(\gamma e^{n+1} + C_f{}^{n+1} h_R + Kuu^{n+1} + Kvv^{n+1}) \\
&\quad - \rho u\left[2(\gamma e + C_f h_R) + (3/2)K(u^2 + v^2)\right] \\
&\quad - (\mu_T/\sigma_h + \mu/Pr \cdot R_l)\gamma \delta_x e^{n+1} \\
&\quad \left. - K(\mu_T + \mu/R_l) s_{ix} u_i + (2/3) K \rho k u\right\} \\
&- \delta_y\left\{(\rho^{n+1}v + \rho v^{n+1})\left[\gamma e + C_f h_R + (K/2)(u^2 + v^2)\right]\right. \\
&\quad + \rho v(\gamma e^{n+1} + C_f{}^{n+1} h_R + Kuu^{n+1} + Kvv^{n+1}) \\
&\quad - \rho v\left[2(\gamma e + C_f h_R) + (3/2)K(u^2 + v^2)\right] \\
&\quad - (\mu_T/\sigma_h + \mu/Pr \cdot R_l)\gamma \delta_y e^{n+1} \\
&\quad \left. - K(\mu_T + \mu/R_l) s_{iy} u_i + (2/3) K \rho k v\right\} \\
&+ K\rho\varepsilon - K\mu_T s_{ij}\, \partial u_i/\partial x_j + (2/3) K\rho k(\delta_x u + \delta_y v)
\end{aligned}
\tag{B11}
$$

The production and dissipation terms have been treated explicitly at the nth level.

The x-sweep energy equation is:

$$(1/\Delta t)\left\{\rho^*\left[e + C_f h_R + (K/2)(u^2 + v^2)\right] + \rho(e^* + C_f^* h_R)\right.$$

$$\left. + K\rho(uu^* + vv^*) - 2\rho(e + C_f h_R) - (3/2)K\rho(u^2 + v^2)\right\}$$

$$= -\delta_x\left\{(\rho^* u + \rho u^*)\left[\gamma e + C_f h_R + (K/2)(u^2 + v^2)\right]\right.$$

$$+ \rho u(\gamma e^* + C_f^* h_R + Kuu^* + Kvv^*)$$

$$- \rho u\left[2(\gamma e + C_f h_R) + (3/2)K(u^2 + v^2)\right]$$

$$- (\mu_T/\sigma_h + \mu/Pr \cdot R_l)\gamma\delta_x e^*$$

$$\left. - K(\mu_T + \mu/R_l) s_{ix} u_i + (2/3)K\rho ku\right\}$$

$$- \delta_y\left\{\rho v\left[\gamma e + C_f h_R + (K/2)(u^2 + v^2)\right]\right.$$

$$- (\mu_T/\sigma_h + \mu/Pr \cdot R_l)\gamma\delta_y e$$

$$\left. - K(\mu_T + \mu/R_l) s_{iy} u_i + (2/3)K\rho kv\right\}$$

$$+ K\rho\varepsilon - K\mu_T s_{ij}\,\partial u_i/\partial x_j + (2/3)K\rho k(\delta_x u + \delta_y v) \qquad \text{(B12)}$$

The y-sweep energy equation is:

$$(1/\Delta t)\left\{(\rho^{**} - \rho^{*})\left[e + C_f h_R + (K/2)(u^2 + v^2)\right] + \rho(e^{**} - e^{*})\right.$$

$$\left. + \rho(C_f^{**} - C_f^{*}) h_R + K\rho\left[u(u^{**} - u^{*}) + v(v^{**} - v^{*})\right]\right\}$$

$$= -\delta_y\left\{(\rho^{**}v + \rho v^{**})\left[\gamma e + C_f h_R + (K/2)(u^2 + v^2)\right]\right.$$

$$+ \rho v(\gamma e^{**} + C_f^{**} h_R + K u u^{**} + K v v^{**})$$

$$- \rho v\left[3(\gamma e + C_f h_R) + 2K(u^2 + v^2)\right]$$

$$\left. - (\mu_T/\sigma_h + \mu/Pr.R_1)\,\gamma\,\delta_y(e^{**} - e)\right\} \qquad \text{(B13)}$$

Conservation of k

The time-linearized difference equation is:

$$(\rho^{n+1} k + \rho k^{n+1} - 2\rho k)/\Delta t$$

$$= -\delta_x\left[\rho^{n+1} uk + \rho u^{n+1} k + \rho uk^{n+1} - 2\rho uk - (\mu_T/\sigma_k)\,\delta_x k^{n+1}\right]$$

$$-\delta_y\left[\rho^{n+1} vk + \rho v^{n+1} k + \rho vk^{n+1} - 2\rho vk - (\mu_T/\sigma_k)\,\delta_y k^{n+1}\right]$$

$$-\rho\epsilon + \mu_T s_{ij}\,\partial u_i/\partial x_j - (2/3)\rho k\,(\delta_x u + \delta_y v) \qquad \text{(B14)}$$

The x-sweep k-equation is:

$$(\rho^{*}k + \rho k^{*} - 2\rho k)/\Delta t$$

$$= - \delta_x \left[\rho^{*}uk + \rho u^{*}k + \rho uk^{*} - 2\rho uk - (\mu_T/\sigma_k)\ \delta_x k^{*}\right]$$

$$- \delta_y \left[\rho vk - (\mu_T/\sigma_k)\ \delta_y k\right] - \rho\epsilon + \mu_T\ s_{ij}\ \partial u_i/\partial x_j$$

$$- (2/3)\ \rho k\ (\delta_x u + \delta_y v) \qquad \text{(B15)}$$

The y-sweep k-equation is:

$$\left[(\rho^{**} - \rho^{*})k + \rho(k^{**} - k)\right]/\Delta t$$

$$= - \delta_y \left[\rho^{**} vk + \rho v^{**} k + \rho vk^{**} - 3\rho vk - (\mu_T/\sigma_k)\delta_y(k^{**} - k)\right] \qquad \text{(B16)}$$

Conservation of ϵ

The time-linearized difference equation is:

$$(\rho^{n+1}\ \epsilon + \rho\epsilon^{n+1} - 2\rho\epsilon)/\Delta t$$

$$= - \delta_x \left[\rho^{n+1}\ u\epsilon + \rho u^{n+1}\ \epsilon + \rho u\epsilon^{n+1} - 2\rho u\epsilon - (\mu_T/\sigma_\epsilon)\ \delta_x\ \epsilon^{n+1}\right]$$

$$- \delta_y \left[\rho^{n+1}\ v\epsilon + \rho v^{n+1}\ \epsilon + \rho v\epsilon^{n+1} - 2\rho v\epsilon - (\mu_T/\sigma_\epsilon)\ \delta_y \epsilon^{n+1}\right]$$

$$+ C_{\epsilon 1}\ (\epsilon/k) \left[\mu_T\ s_{ij}\ \partial u_i/\partial x_j - (2/3)\rho k\ (\delta_x u + \delta_y v)\right] - C_{\epsilon 2}\ \rho\epsilon^2/k \qquad \text{(B17)}$$

The x-sweep ϵ-equation is:

$$(\rho^* \epsilon + \rho \epsilon^* - 2\rho\epsilon)/\Delta t$$

$$= - \delta_x \left[\rho^* u\epsilon + \rho u^* \epsilon + \rho u \epsilon^* - 2\rho u \epsilon - (\mu_T/\sigma_\epsilon)\delta_x \epsilon^*\right]$$

$$- \delta_y \left[\rho v \epsilon - (\mu_T/\sigma_\epsilon)\delta_y \epsilon\right]$$

$$+ C_{\epsilon_1} (\epsilon/k) \left[\mu_T s_{ij} \partial u_i/\partial x_j - (2/3)\rho k (\delta_x u + \delta_y v)\right] - C_{\epsilon 2} \rho \epsilon^2/k \qquad \text{(B18)}$$

The y-sweep ϵ-equation is:

$$\left[(\rho^{**} - \rho^*) \epsilon + \rho(\epsilon^{**} - \epsilon^*)\right]/\Delta t$$

$$= - \delta_y \left[\rho^{**} v\epsilon + \rho v^{**} \epsilon + \rho v \epsilon^{**} - 3\rho v \epsilon - (\mu_T/\sigma_\epsilon)\delta_y(\epsilon^{**} - \epsilon)\right] \qquad \text{(B19)}$$

Conservation of Species

The time-linearized difference equation is:

$$(\rho^{n+1} C_a + \rho C_a^{n+1} - 2\rho C_a)/\Delta t$$

$$= - \delta_x \left[\rho^{n+1} u C_a + \rho u^{n+1} C_a + \rho u C_a^{n+1} - 2 \rho u C_a \right.$$

$$\left. - (\mu_T/\sigma_c + \rho D_a) \delta_x C_a^{n+1} \right]$$

$$- \delta_y \left[\rho^{n+1} v C_a + \rho v^{n+1} C_a + \rho v C_a^{n+1} - 2 \rho v C_a - (\mu_T/\sigma_c + \rho D_a) \delta_y C_a^{n+1} \right]$$

$$+ \rho \dot{w}_a \qquad \text{(B20)}$$

The x-sweep species conservation equations is:

$$(\rho^* C_a + \rho C_a^* - 2 \rho C_a)/\Delta t$$

$$= - \delta_x \left[\rho^* u C_a + \rho u^* C_a + \rho u C_a^* - 2 \rho u C_a - (\mu_T/\sigma_c + \rho D_a) \delta_x C_a^* \right]$$

$$- \delta_y \left[\rho v C_a - (\mu_T/\sigma_c + \rho D_a) \delta_y C_a \right] + \rho \dot{w}_a \qquad \text{(B21)}$$

The y-sweep species conservation equation is:

$$\left[(\rho^{**} - \rho^*) C_a + \rho (C_a^{**} - C_a^*) \right]/\Delta t$$

$$= - \delta_y \left[\rho^{**} v C_a + \rho v^{**} C_a + \rho v C_a^{**} - 3 \rho v C_a - (\mu_T/\sigma_c + \rho D_a) \delta_y (C_a^{**} - C_a) \right]$$

(B22)